

---

# Impact of liquid droplets with deformable surfaces

---

A thesis submitted to the School of Mathematics at the  
University of East Anglia in partial fulfilment of the  
requirements for the degree of Doctor of Philosophy

Michael Pegg

September 2019

© This copy of the thesis has been supplied on condition that anyone who consults it is understood to recognise that its copyright rests with the author and that use of any information derived there from must be in accordance with current UK Copyright Law. In addition, any quotation or extract must include full attribution.



# Abstract

---

During a droplet impact onto a substrate, splashing is known to be caused by the presence of surrounding gas or by surface roughness. Impact occurring in a vacuum onto a smooth rigid wall results in droplet spreading, rather than development of a corona or prompt splash. In this thesis we present an analytical and numerical study of a third potential splashing mechanism, namely elastic deformation of the substrate. An axisymmetric Wagner-style model of droplet impact is formulated and solved using the method of normal modes, together with asymptotic analysis and numerical methods. We highlight the effect that a flexible substrate brings to the contact line velocity and jet behaviour, demonstrating that oscillation of the substrate can cause blow-up of the splash jet which is absent for a rigid substrate and indicate the onset of splashing.

In chapter 4 we investigate the important role air plays in the pre-impact behaviour of a liquid droplet approaching a solid substrate. A model for the air cushioning of a liquid droplet approaching a partially flexible solid substrate is developed using asymptotic and complex analysis methods. The model is solved numerically using boundary elements and method of normal modes. We show the presence of an elastic plate causes a slowing of the impact and if positioned directly underneath the droplet reduce the overall impact pressure. When the plate is not placed symmetrically touch down is found at only one location, with this touch down point having significantly higher impact pressures than initially anticipated.

Finally in chapter 5 we develop a model for the impact of a liquid droplet with an attached air cavity. This preliminary model couples the various parameters inside the gas to the classical Wagner approach for liquid impact and allows us to investigate the evolution of the air cavity and its impact on the motion of the contact points.

## **Access Condition and Agreement**

Each deposit in UEA Digital Repository is protected by copyright and other intellectual property rights, and duplication or sale of all or part of any of the Data Collections is not permitted, except that material may be duplicated by you for your research use or for educational purposes in electronic or print form. You must obtain permission from the copyright holder, usually the author, for any other use. Exceptions only apply where a deposit may be explicitly provided under a stated licence, such as a Creative Commons licence or Open Government licence.

Electronic or print copies may not be offered, whether for sale or otherwise to anyone, unless explicitly stated under a Creative Commons or Open Government license. Unauthorised reproduction, editing or reformatting for resale purposes is explicitly prohibited (except where approved by the copyright holder themselves) and UEA reserves the right to take immediate 'take down' action on behalf of the copyright and/or rights holder if this Access condition of the UEA Digital Repository is breached. Any material in this database has been supplied on the understanding that it is copyright material and that no quotation from the material may be published without proper acknowledgement.

# Contents

---

|   |           |
|---|-----------|
| <b>Abstract</b>   | <b>2</b>  |
| <b>List of Figures</b>  | <b>7</b>  |
| <b>Acknowledgements</b>                                       | <b>15</b> |
| <b>1 Introduction</b>   | <b>16</b> |
| <b>2 Droplet Impact onto a Simply Supported Elastic Plate</b> | <b>23</b> |
| 2.1 Introduction . . . . .                                    | 23        |
| 2.2 Formulation of the problem . . . . .                      | 25        |
| 2.3 Coupled problem of hydroelastic impact . . . . .          | 33        |
| 2.3.1 Coupled problem . . . . .                               | 35        |
| 2.3.2 Hydrodynamic problem . . . . .                          | 37        |
| 2.4 Jet-root and jet regions . . . . .                        | 39        |
| 2.4.1 Jet-root region . . . . .                               | 40        |
| 2.4.2 Jet region . . . . .                                    | 44        |

---

|          |  |            |
|----------|--|------------|
| 2.5      | Numerical solution . . . . .                                   | 49         |
| 2.6      | Results . . . . .  | 51         |
| <b>3</b> | <b>Impact of a droplet with a clamped elastic plate</b>        | <b>59</b>  |
| 3.1      | Problem formulation . . . . .                                  | 60         |
| 3.2      | Results . . . . .  | 63         |
| <b>4</b> | <b>Air cushioning</b>  | <b>70</b>  |
| 4.1      | Air cushioning with an elastic substrate . . . . .             | 70         |
| 4.1.1    | Problem Definition . . . . .                                   | 70         |
| 4.1.2    | Problem Solution . . . . .                                     | 79         |
| 4.2      | Numerical Methods . . . . .                                    | 81         |
| 4.2.1    | Numerical Validation . . . . .                                 | 88         |
| 4.2.2    | Touchdown . . . . .  | 90         |
| 4.3      | Results . . . . .  | 93         |
| <b>5</b> | <b>Impact of a droplet which contains a trapped gas cavity</b> | <b>101</b> |
| 5.1      | Problem definition . . . . .                                   | 101        |
| 5.2      | Problem Solution . . . . .                                     | 104        |
| 5.2.1    | Numerical Solution . . . . .                                   | 115        |
| 5.3      | Results . . . . .  | 118        |
| <b>6</b> | <b>Conclusions and future work</b>                             | <b>129</b> |

|                   |   |            |
|-------------------|---|------------|
| 6.1               | Conclusions   | 129        |
| 6.2               | Future Work   | 134        |
| <b>Appendices</b> |   | <b>142</b> |
| <b>A</b>          | <b>Integrals <math>U_n</math></b>                             | <b>142</b> |
| <b>B</b>          | <b>Integrals <math>Q_n(a)</math></b>                          | <b>143</b> |
| <b>C</b>          | <b>Calculation of the vector elements <math>g_n(a)</math></b> | <b>145</b> |
| <b>D</b>          | <b>Elements of the added-mass matrix</b>                      | <b>147</b> |

# List of Figures

---

|  |    |
|--|----|
| 2.1.1 A schematic of the impact problem showing the outer, jet-root and jet regions. . . . .   | 24 |
| 2.2.1 A two-dimensional representation of the problem. A spherical droplet of radius $R$ , travelling with constant speed $V$ , impacts onto a circular elastic plate of radius $L$ (thin horizontal line) housed in a solid housing of otherwise infinite extent (thick horizontal line). . . . .   | 25 |
| 2.2.2 A sketch of the problem away from the contact region. The light grey paraboloid shows the liquid free surface $z = \epsilon\eta(r, t)$ , the dark grey circle is the elastic plate with deformation $z = \epsilon(t - w(r, t))$ and the light gray square region indicates the infinite rigid housing for the elastic plate. . . . . | 33 |
| 2.4.1 A sketch of the jet-root region problem. . . . .   | 41 |
| 2.4.2 A sketch of the hodograph plane for the jet-root region $U = \phi_X - i\phi_Z$ . . . . .   | 42 |
| 2.6.1 Parametric plane showing the regions of negative and unbounded contact line velocity. Pluses represent simulations which encountered contact line shrinkage, a cross represents a simulation with no problems and a filled circle represents a simulation with an unbounded contact line velocity. . . . .                           | 52 |

|   |    |
|---|----|
| 2.6.2 Contact line velocity $da/dt$ for $\alpha = 0.01$ , $\beta = 0.001$ as a function of the non-dimensional contact line radius $a(t)$ . . . . .   | 55 |
| 2.6.3 The averaged plate displacement (a) and averaged plate velocity (b) for $\alpha = 0.01$ , $\beta = 0.001$ as functions of contact line radius $a$ . . . . .   | 55 |
| 2.6.4 The contact line velocity (a) and plate shapes (b) calculated at intervals of $a = 0.05$ for $\alpha = 0.005$ , $\beta = 0.014$ . . . . .   | 55 |
| 2.6.5 Contact line velocity $da/dt$ for $\alpha = 0.1$ , $\beta = 0.02$ as a function of contact line radius $a$ . . . . .  | 56 |
| 2.6.6 Plot of splashing conditions (2.4.32) and (2.4.33) for $\alpha = 0.2$ , $\beta = 0.3$ . The circle indicates the value of $\tau$ for which splashing first occurs. . . . .  | 57 |
| 2.6.7 For the parameters $\alpha = 0.1$ and $\beta = 0.5$ (a) shows the jet thickness $h(r, t)$ given by (2.4.29) as the function of $r$ , where $r > a(t)$ for $t = 0.07, 0.12$ and $0.19$ . Plot (b) shows the growth of the splash for the interval $0.12 < \tau < 0.14$ of the Lagrangian coordinate $\tau$ , from time $t = 0.07$ to $t = 0.18$ in steps of $0.01$ . Increasing time is shown by increasing maximum in both plots. . . . . | 57 |
| 2.6.8 The $\alpha - \beta$ parametric plot where splashing is predicted, the dark crossed region, and where it is not predicted, the dotted region. . . . .   | 58 |
| 3.1.1 The first 4 normal modes for the clamped boundary condition (a) and simply supported (b). . . . .   | 62 |
| 3.2.1 Contact line velocity against contact line position for the clamped, simply supported and rigid substrates. The elastic plates have parameters $\alpha=1.5$ , $\beta=1.5$ . . . . .   | 63 |

|  |    |
|--|----|
| 3.2.2 Plate shapes taken at snapshots of $a = 0.1$ for the plate parameters $\alpha = \beta = 1.5$ . Figure (a) is a clamped plate and Figure (b) simply supported . . . . .   | 64 |
| 3.2.3 A parametric $\alpha - \beta$ plot showing regions where the contact line velocity becomes zero (blue stars), very large (red crosses) and reaches the end of the plate with no issue (black pluses) . . . . .   | 65 |
| 3.2.4 Plot of splashing conditions (2.4.33) for $\alpha = 0.1$ and $\beta = 0.5$ . The circle indicates the $\tau$ at which splashing is first seen. . . . .   | 66 |
| 3.2.5 The shape of the jet at times $t = 0.1, 0.155, 0.21, 0.265$ for plate parameters $\alpha = 0.1$ and $\beta = 0.5$ . . . . .  | 66 |
| 3.2.6 A parametric $\alpha - \beta$ plot showing regions where splashing is predicted (black crosses) and not predicted (red pluses) . . . . .   | 67 |
| 3.2.7 Contact line velocity for clamped, simply supported and rigid substrates. The elastic substrates have parameters $\alpha = 1.5$ and $\beta = 0.5$ . For these parameters a splash is predicted for the simply supported plate only. . . . .              | 68 |
| 3.2.8 Plate shapes taken at snapshots of $a = 0.1$ for the plate parameters $\alpha = 1.5$ and $\beta = 0.5$ . Figure (a) is a clamped plate and Figure (b) simply supported . . . . .   | 68 |
| 3.2.9 Contact line velocity for clamped, simply supported and rigid substrates. The elastic substrates have parameters $\alpha = 0.1$ and $\beta = 0.5$ . For these parameters a splash is predicted for both the simply supported and clamped plates. . . . . | 69 |
| 3.2.10 Plate shapes taken at snapshots of $a = 0.1$ for the plate parameters $\alpha = 0.1$ and $\beta = 0.5$ . Figure (a) is a clamped plate and Figure (b) simply supported . . . . .  | 69 |

|   |    |
|---|----|
| 4.1.1 Schematic showing the problem being considered in this section. . . . .   | 71 |
| 4.2.1 Time evolution of the free surface height ( <i>a</i> ), elastic plate deflection ( <i>b</i> ) and pressure ( <i>c</i> ) at the origin for plate parameters $\alpha = 1.0, \beta = 1.0, x_0 = 0, L = 10$ . In each Figure there are 3 plots, calculated with differing time steps and a spatial step of $\delta x = 0.01$ . . . . .  | 88 |
| 4.2.2 Time evolution of the free surface height ( <i>a</i> ), elastic plate deflection ( <i>b</i> ) and pressure ( <i>c</i> ) at the origin for plate parameters $\alpha = 1.0, \beta = 1.0, x_0 = 0, L = 10$ . In each Figure there are 3 plots, calculated with different spatial step and a time step of $\delta x = 0.01$ . . . . .   | 88 |
| 4.2.3 Time evolution of the free surface height ( <i>a</i> ), elastic plate deflection ( <i>b</i> ) and pressure ( <i>c</i> ) at the origin for plate parameters with different starting times $t = t_0$ . . . . .  | 89 |
| 4.3.1 Time evolution of the free surface ( <i>a</i> ) and pressure ( <i>b</i> ) with a rigid substrate. Curves are taken at time intervals of $t = 1$ and at the time step before termination of the simulation. The red line corresponds to time $t = 0$ and blue to the final iteration. . . . .  | 94 |
| 4.3.2 Time evolution of the free surface ( <i>a</i> ), elastic plate deformation ( <i>b</i> ) and pressure ( <i>c</i> ) for a substrate with elastic parameters $L = 10, \alpha = \beta = 1.0$ . Curves are taken at time intervals of $t = 1$ and at the time step before termination of the simulation. The red line corresponds to time $t = 0$ and blue to the final iteration. . . . . | 95 |
| 4.3.3 Time evolution of the distance between the free surface and substrate for elastic parameters $L = 10, \alpha = \beta = 1.0$ . Curves are taken at time intervals of $t = 1$ and at the time step before termination of the simulation. The red line corresponds to time $t = 0$ and blue to the final iteration. . . . .  | 95 |

- 4.3.4 Time evolution of the free surface (a), elastic plate deformation (b) and pressure (c) for a substrate with elastic parameters  $L = 20$ ,  $\alpha = \beta = 1.0$ . Curves are taken at time intervals of  $t = 1$  and at the time step before termination of the simulation. The red line corresponds to time  $t = 0$  and blue to the final iteration. . . . . 96
- 4.3.5 A set of plots showing the time evolution of the gap between free surface and substrate  $F - W$  for different plate parameters. In each Figure the plate length  $L = 10$ . Figures are arranged such that columns from left to right have  $\beta = 0.5, 1.0$  and  $2.0$  while rows from top to bottom have  $\alpha = 0.5, 1.0$  and  $2.0$ . . . . . 97
- 4.3.6 A set of plots showing the time evolution of the gas pressure  $P$  for different plate parameters. In each Figure the plate length  $L = 10$ . Figures are arranged such that columns from left to right have  $\beta = 0.5, 1.0$  and  $2.0$  while rows from top to bottom have  $\alpha = 0.5, 1.0$  and  $2.0$ . . . . . 98
- 4.3.7 A set of plots showing the effect of altering the location of the elastic plate. Columns from left to right have plate centres at  $x_0 = 0, 2, 4$  and  $6$  respectively. Rows from top to bottom show the free surface  $F(x, t)$ , gap between free surface and substrate  $F(x, t) - W(x, t)$ , plate deformation  $W(x, t)$ , pressure  $P(x, t)$  and horizontal velocity of the gas at the centre of the gap  $U(x, y = (F(x, t) - W(x, t))/2, t)$  and horizontal flux of the gas. In all Figures the plate has parameters  $\alpha = 1.0, \beta = 1.0$  and a length of  $L = 10$ . In the first two rows of Figures the vertical lines show the edge of the elastic plate. . . . . 99

|   |     |
|---|-----|
| 4.3.8 A set of plots showing the effect of altering the location of the elastic plate. Columns from left to right have plate centres at $x_0 = 0, 2, 4$ and $6$ respectively. Rows from top to bottom show the gap between free surface and substrate $F(x, t) - W(x, t)$ , pressure $P(x, t)$ and horizontal flux of the gas. In all Figures the plate has parameters $\alpha = 0.3, \beta = 0.3$ and a length of $L = 10$ . In the first two rows of Figures the vertical lines show the edge of the elastic plate. . . . . | 100 |
| 5.1.1 A schematic showing the problem being considered after inversion from a liquid impacting solid problem to a solid impacting liquid one. . . . .   | 103 |
| 5.2.1 Sketch of the boundary value problem (5.1.4)-(5.1.8). . . . .   | 104 |
| 5.3.1 The contact point positions (a) and contact point velocities (b) for the substrate surface shape given in equation (5.2.59) and with no gas in the cavity. . . . .  | 120 |
| 5.3.2 The contact point positions (a) and contact point velocities (b) for the substrate shape given in equation (5.2.60) and with no gas in the cavity. . . . .  | 121 |
| 5.3.3 A comparison of the evolution of $a(t)$ between the free surface shape being the same on either side of the contact line, (5.2.59), and different on either side of the contact line, (5.2.60) . . . . .  | 121 |
| 5.3.4 The contact point position (a), contact point velocity (b), pressure in the cavity (c) and volume of the cavity (d) for the solid substrate shape given in equation (5.2.59) with $C_0 = 1$ . . . . .   | 122 |
| 5.3.5 The contact line positions for $C_0 = 0.1$ (a) and $C_0 = 2$ (b) . . . . .  | 123 |
| 5.3.6 Comparing the motion of $b(t)$ for a range of $C_0$ . . . . .   | 123 |

- 5.3.7 The contact line position (a), contact line velocity (b) and cavity volume (c) for the free surface shape given in equation (5.2.60) and  $C_0 = 0.1$ . . . . . 124
- 5.3.8 The contact line position (a), contact line velocity (b) and cavity volume (c) for the free surface shape given in equation (5.2.60) and  $C_0 = 1$ . . . . . 125
- 5.3.9 The contact line position (a), contact line velocity (b) and cavity volume (c) for the free surface shape given in equation (5.2.60) and  $C_0 = 0.1$ . . . . . 125
- 5.3.10 Parametric plots showing the inner contact line position (a), outer contact line position (b), time (c) and cavity volume (d) at the final iteration time  $t = t_f$ . for both the purely quartic incoming solid shape in equation 5.2.59 and the mixed quartic quadratic shape from equation 5.2.60 . . . . . 126
- 5.3.11 Figure (a) shows the contact line positions against time for an unperturbed free surface (5.2.59) and a perturbed free surface (5.3.9) with parameters  $D = 0.00, k = 1, l = 0.2, x_0 = 0.7$ . Figure (b) shows the difference between perturbed and unperturbed inner contact line positions  $a(t)$  divided by the amplitude of the perturbation  $D = 0.005$  against time. The compressibility coefficient was set to  $C_0 = 0.1$  . . . . . 128
- 5.3.12 Figure (a) shows the contact line positions against time for an unperturbed free surface (5.2.59) and a perturbed free surface (5.3.9) with parameters  $D = 0.0008, k = 5, l = 0.1, x_0 = 0.5$ . Figure (b) shows the difference between perturbed and unperturbed inner contact line positions  $a(t)$  divided by the amplitude of the perturbation  $D = 0.0008$  against time. The compressibility coefficient was set to  $C_0 = 0.1$  . . . . . 128

---

|   |     |
|---|-----|
| B.0.1 The functions $Q_n(a)$ for $n = 1, 2, 3$ and 4 using modes calculated with $\nu = 0.3$ . . . . .  | 144 |
| C.0.1 $g_n$ versus $a$ for $n = 1, 2, 3$ and 4 using modes calculated with $\nu = 0.3$ for $\dot{h} = 1$ . . . . .  | 146 |
| D.0.1(a) The first 4 diagonal elements of the added mass matrix, $W_{nn}(a)$ .<br>(b) The first 3 off diagonal elements of the first column of the added mass matrix, $W_{nm}(a)$ . . . . . | 148 |

# Acknowledgements

---

I would like to thank both of my supervisors, Professor Alexander Korobkin and Dr Richard Purvis, for their fantastic support, supervision and expertise over the many years of my studies. I am truly thankful for having both as my supervisors and could not have had a better pair of friends and colleagues for my PhD studies. I would like to thank the many friends I've made within the UEA mathematics PhD office over the years for the discussions and distractions. I would like to thank my family for their endless love and support, especially my Mum who was so helpful and caring throughout my illness.

The work within this thesis was funded by the Engineering and Physical Research Council and results were obtained using the UEA High Performance Computer Cluster.

# Introduction

---

Liquid impact phenomena are ubiquitous in science, nature, and technology. They are critically important in fields ranging from biotechnology and agriculture to marine engineering. One particular phenomenon observed in liquid impacts on solid surfaces is that of splashing, where the wetting front propagating along the surface becomes unstable, detaches from the surface and can subsequently disperse into multiple smaller droplets. Several mechanisms of splashing initiation have been identified, for example, surface roughness and interaction of the fast moving wetting jet with the surrounding air. Controlling splashing is of practical interest. When designing a car windscreen splashing is encouraged to disperse rain [Blocken and Carmeliet, 2004], whilst splashing should be avoided in ink-jet printing [Martin et al., 2008]. Splashing is a complicated process governed by several physical effects. It is determined by properties of the liquid, substrate and surrounding atmosphere. Flexibility of the substrate is another physical effect which may cause splashing. This effect has not yet been fully understood for substrates with relatively high rigidity.

Despite the importance of splashing, the mechanisms that trigger splashing are still not fully understood. It was discovered by experiments carried out by Xu et al. [2005] that the pressure of the surrounding gas was critically important for the splashing of a drop impacting a smooth surface. Xu [2007] later experimentally studied the impact of liquid drops with a variety of surfaces and found that the surrounding gas is responsible for “corona” splash and substrate

roughness causes “prompt” splash. [Riboux and Gordillo \[2014\]](#) studied the effects of the presence of surrounding gas in droplet impacts onto smooth surfaces, deriving a relationship between splashing and a critical impact velocity. [Ellis et al. \[2011\]](#) analytically investigated the impact of a liquid droplet with a rough surface using the Wagner model for a surface of small roughness, and an alternative model for more rough surfaces. Their study did not incorporate splashing, but the analysis showed that the effect of surface roughness can be modelled in an appropriate small roughness limit.

It has been shown experimentally that elasticity can play a key role in splashing. [Pepper et al. \[2008\]](#) presented an experimental study of droplets impacting an elastic membrane held under different tensions. They found indications that it is the very early times after impact that are critical for determining whether splashing will occur. They showed that a soft substrate can suppress splashing entirely. Experimental studies ([Alizadeh et al. \[2013\]](#), [Mangili et al. \[2012\]](#)) of droplets impacting deformable surfaces have focused on soft surfaces. In chapters 2 and 3 we introduce and investigate a brand new mechanism that can cause splashing, the presence of an elastic plate. This is unexpected since, in previous experimental studies flexible substrates have been found to suppress splashing but by focusing on a regime where the deflection of a small elastic plate is strongly coupled to the hydrodynamics of an impacting droplet we show that elasticity can in fact cause splashing. This has potential applications in the modelling of spraying pesticides on plants, improving the resolution of additive manufacturing and the design of new micropatterned surfaces for example.

The Wagner model is used in several chapters of the thesis. It was first developed by [Wagner \[1932\]](#) for evaluating the hydrodynamic loads on the floaters of seaplanes during landing. The Wagner model assumes that the solid surface, and the free surface of the liquid at impact are nearly parallel to each-other with the normal displacements of these surfaces being much smaller than the size of their contact region. The Wagner model is used during the early stages of impact, when the geometry of the impacting surfaces, equations

of the liquid flow, and the corresponding boundary conditions can be simplified. However, the problem remains non-linear because the size of the wetted area is unknown in advance and should be determined as part of the solution. The size of the wetted part of the substrate is determined by using the so-called Wagner condition. This condition requires that the liquid boundary, which includes the liquid free surface and the wetted area of the substrate, is continuous and was first described within the model by Wagner [1932]. This condition was formally justified by Howison et al. [1991] through an asymptotic analysis of liquid impact problems.

Many of the studies adopting the Wagner model have focused on two dimensional problems. Liquid-liquid impacts were investigated by Semenov et al. [2015]. A droplet-liquid impact problem was investigated by Howison et al. [2005]. Water entry problems have received much more attention, stretching as far back as the studies by von Karman [1929], who investigated the impact of a solid wedge onto a water free surface. Other examples include Wu [2007] who investigated the impact of liquid columns and droplets on solid wedges and Philippi et al. [2016] who investigated the early stages of a liquid drop impacting with a solid plate. Korobkin [1985] investigated a three dimensional water impact problem using the displacement potential however he was not able to fully solve the problem. This problem was later solved by Scolan and Korobkin [2001]. Liquid-elastic impacts have begun to receive an increasingly large amount of attention. Khabakhpasheva and Korobkin [2013] investigated the two dimensional liquid elastic wedge impact problem and Tkacheva [2008] studied the impact of a box with an elastic base onto a thin layer of liquid. Many of the papers studying the three dimensional impact problem derive from the work presented by Scolan and Korobkin [2001] and Korobkin and Scolan [2006]. Xu et al. [2011] investigated the axisymmetric impact of a liquid block onto a solid surface and Scolan [2004] has produced one of the few works on an axisymmetric liquid-elastic impact. Several of the previous works studying liquid impact onto an elastic surface used the method of normal modes, such as the studies by Korobkin and Khabakhpasheva [2006] and Scolan

[2004]. In the method of normal modes deflections of an elastic substrate are represented as a superposition of the substrates normal modes. By performing our analysis in 3d in chapters 2 and 3 we will present results that can be used by experimentalists to verify our predictions and model.

In the study of droplet impacts air effects are often neglected. When considering water droplets in air at atmospheric pressure indeed it is difficult to immediately see how large of an effect the air can have when there is three order of magnitude difference in density. However in surprising experiments by Xu et al. [2005] it was found that a reduction in air pressure, which can be thought of as a reduction in air density, can suppress and completely remove splashing during droplet impact. Sprittles [2017] investigated the maximum speed at which a liquid-gas free surface can wet a solid by including gas effects in his analysis via the Boltzmann equation. Moore et al. [2013] investigated the effects that air cushioning has on the asymptotic 'outer', 'jet-root' and 'jet' regions as defined by Howison et al. [1991]. These and many other studies highlight the important role that air can play in the behaviour of many different hydrodynamic systems.

One of the important effects of air on liquid droplets happens during impact with a solid substrate. As the droplet nears the substrate air cannot evacuate the gap between droplet and substrate fast enough, leading to an increase in air pressure below the droplet. This increased air pressure then resists the downward motion of the liquid droplet. The effect of this 'air-cushion' is to delay impact time, produce an impact at a line rather than a point (in 3d) and to trap an air bubble inside the droplet upon impact. The earliest theoretical interest in air cushioning comes from ship slamming where Verhagen et al. [1967] considered the gas in a one dimensional channel during a slow impact. Wilson [1991] derived a set of equations in two dimensions where the gas and liquid were both inviscid. Droplet length scales are significantly smaller than those in ship slamming, prompting Smith et al. [2003] to derive a set of equations which balance an inviscid liquid with a viscous gas modelled with lubrication equations. The lubrication pressure becomes extremely large as the free surface approaches the solid substrate which

prevents numerical computation up to the point of touch down. Asymptotic analysis centred on the touch down point were carried out and it was shown that the touch down does occur in finite time when surface tension is neglected. Following [Smith et al. \[2003\]](#) many extensions to the lubrication style approach were made. [Mandre et al. \[2009\]](#) and [Purvis and Smith \[2004\]](#) extended the model to include strong surface tension and concluded that in this case touch down does not occur. The model was extended into three dimensions by [Hicks and Purvis \[2010\]](#). The predictions of bubble volume in [Hicks and Purvis \[2010\]](#) were found to be in good agreement with experimental measurements by [Thoroddsen et al. \[2005\]](#). Air cushioning with a porous substrate was considered by [Hicks and Purvis \[2017\]](#). Some studies have focused on air cushioning between an incoming droplet and a liquid layer, such as [Hicks and Purvis \[2011\]](#). In these liquid-liquid air cushioning problems both free surfaces are deformed by the air cushion, somewhat similar to our situation where we have an elastic substrate rather than a layer of liquid. However the dynamics of a partially elastic substrate are different to that of a liquid substrate. For a start we can move the location of the elastic plate introducing a variable level of asymmetry in the problem which has an interesting effect on the impact pressures and touch down time of the droplet. The edges of the elastic plate, where it is clamped to the solid part of the substrate also influence the droplet, often causing touch down to occur rapidly upon the spreading liquid drop encountering this area.

In most theoretical works, such as those considered by [Moore et al. \[2012\]](#), [Scolan \[2004\]](#) and [Semenov et al. \[2015\]](#) the contact between the liquid and solid starts at a single point. However, because of the air cushioning effect it is possible for a small air bubble to be trapped inside the droplet, causing touch down at two points (in 2d) or a line (in 3d). There are many experimental observations of this effect, one of the earliest being [Lesser and Field \[1983\]](#). Recent advances in experimental techniques and high-speed photography contribute to a wide array of air-cushioning experiments across a range of set-ups. [Thoroddsen et al. \[2003, 2005\]](#) captured the formation and contraction of the air bubble between a liquid

droplet and solid shortly after impact using high speed photography. [Driscoll and Nagel \[2011\]](#) used interference imaging to measure the thickness of the trapped air pocket between a liquid droplet and solid post impact and found that it dissipated before a splashing lamella was formed. Air cushioning also occurs in impacts between two liquids.

Air cushioning is also of industrial interest. As explained by [Poots et al. \[2000\]](#) during flight supercooled droplets impact with the aircraft, potentially freezing and causing a reduction in lift which may prove catastrophic. Failure to accurately predict where droplets impact, spread and splash with an aircraft wing can lead to poorly placed or inadequate de-icing mechanisms. At the typical velocities plane wings meet liquid droplets at the inclusion of air-cushioning is vital for fully understanding and predicting icing. As discussed by [Purvis and Smith. \[2016\]](#) predicting the impacting droplet speed and size is critical for being able to properly model the size, speed and location of any ice formation. Failure to predict these accurately can lead to inadequate or improperly placed de-icing mechanisms with potentially lethal consequences. Experiments have been carried out by [Maitra et al. \[2014a,b\]](#) where liquid droplets impact textured and superhydrophobic substrates in an attempt to control and predict the formation of ice. In these works pre-impact air cushioning was seen to play an important role. With aircraft beginning to be designed using complex new materials understanding the effect a variably flexible material has on the build up of ice could be important for safe and efficient flying.

The role that air plays in droplet evolution post impact has received attention from experimentalists. [Kolinski \[2015\]](#) performed experiments showing the evolution of the air film trapped below an impacting droplet and the method by which it breaks up. [Tran et al. \[2013\]](#) carried out experiments with droplets impacting a deep pool of liquid and showed the impact can cause air to become entrained within the liquid. Due to the complexity of the dynamics when air is included analytical progress of modelling the evolution of droplets post-impact

has been slow. [Verhagen et al. \[1967\]](#) developed a model in which a flat bottomed solid impacted a free surface with trapped air using experimental insights to justify some assumptions. [Moore and Oliver \[2014\]](#) and [Moore et al. \[2013\]](#) presented a modified Wagner model, with the air taken into account, and showed how its presence affects the location of the contact points and lines in 2D and 3D. This model was started with a parabolic free surface touching down on the solid substrate, neglecting the effect that pre-impact air cushioning has on droplet shape. [Riboux and Gordillo \[2014\]](#) introduced a model for the motion of the liquid jet and used it to derive an equation predicting when the jet will lift off the solid substrate due to lubrication effects. [Moore et al. \[2013\]](#) also investigated the impact air plays on the evolution of the liquid jet. They introduced a series of models to take account for the surface tension and gravity. Modelling the transition from pre-impact air cushioning to a post impact model is a problem with no clear solution, hence the previous analytical works starting at impact with an idealised set up. One potential area of investigation for this problem is in modelling rarified gas to bridge the time between the breakdown of air cushioning and the beginning of impact. [Sprittles and Shikhmurzaev \[2012\]](#) incorporated kinetic effects of the gas at small length scales and showed there is an appreciable affect in the maximum speed a solid can be wet. Unlike most previous analytical work we present a model where there is a trapped air cavity, rather than effectively 'turning on' the air's influence upon impact. This additional phase along the solid surface adds a great deal of complexity and allows us to investigate effects such as the halting of the inner contact point and make some comparisons between the mechanics seen in our model and those shown by previous experiments. Although the model we produce in chapter 5 is preliminary it captures many complex behaviours and provides a strong framework for future works in this very important area.

# Droplet Impact onto a Simply Supported Elastic Plate

---

## 2.1 Introduction

During a droplet impact onto a substrate, splashing is known to be caused by the presence of surrounding gas or by surface roughness. Impact occurring in a vacuum onto a smooth rigid wall results in droplet spreading, rather than development of a corona or prompt splash. In this chapter we present an analytical and numerical study of a third potential splashing mechanism, namely elastic deformation of the substrate. An axisymmetric Wagner-style model of droplet impact is formulated and solved using the method of normal modes, together with asymptotic analysis and numerical methods. We highlight the effect that a flexible substrate brings to the contact line velocity and jet behaviour, demonstrating that elasticity can cause rupture of the splash jet which is absent for a rigid substrate.

In section [2.2](#) we introduce the problem of a droplet impacting upon a substrate which includes an elastic part. We introduce the relevant scales and non-dimensional variables for the early stage of droplet impact within a potential flow model. Both the coupled elastic and hydrodynamic problems are described at the leading order. These problems are coupled, in particular, via the equation for the unknown radius of the contact region between the droplet

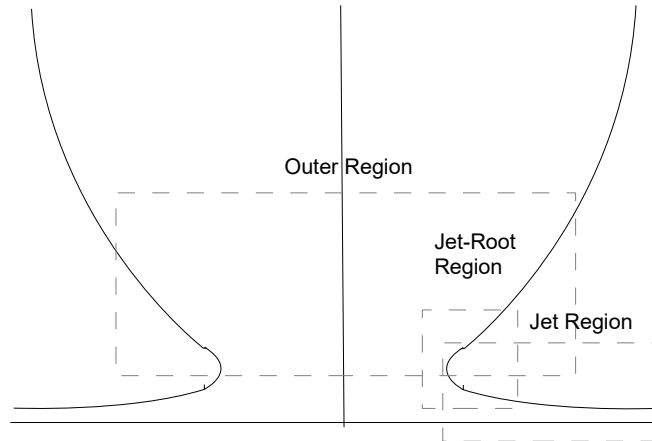


Figure 2.1.1: A schematic of the impact problem showing the outer, jet-root and jet regions.

and substrate. The resulting model is based on the Wagner model of liquid impact. In section 2.3, the plate deflection is obtained by the normal mode method and the hydrodynamic pressure in the contact region is determined as a solution of an axisymmetric mixed boundary value problem for the velocity potential of the flow in the droplet. The obtained solution predicts singular flow velocities close to the advancing contact line. The Wagner solution is corrected near the contact region in section 2.4.1, where the jet-root region is introduced. The solution of the problem in the jet-root region provides the speed of the flow at the entrance to the jet sheet and the thickness of this sheet. The jet flow is described by the one-dimensional non-linear model in subsection 2.4.2. It is shown that the nonlinear jet solution breaks down if the acceleration of the contact line is positive, predicting unbounded jet thickness. This is interpreted as splashing. In section 2.5, the coupled problem of hydroelasticity is solved numerically. Convergence and stability of the numerical algorithm are discussed. The results of the analysis are presented in section 2.6. It is shown that the Wagner model of liquid impact is no longer appropriate for very thin plates, or for very flexible plates. Conditions of splashing are obtained and explained. Figure 2.1.1 shows a depiction of the three flow regions we consider in this chapter.

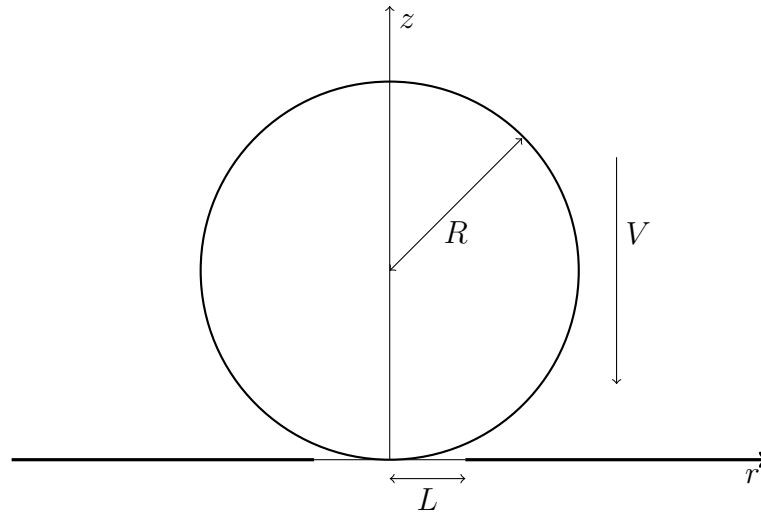


Figure 2.2.1: A two-dimensional representation of the problem. A spherical droplet of radius  $R$ , travelling with constant speed  $V$ , impacts onto a circular elastic plate of radius  $L$  (thin horizontal line) housed in a solid housing of otherwise infinite extent (thick horizontal line).

## 2.2 Formulation of the problem

In this chapter we address the normal impact between an axisymmetric liquid droplet and a circular elastic plate which is housed within an otherwise rigid flat surface. The radius of the elastic plate is taken to be much smaller than the radius of the liquid droplet. This configuration is used to highlight the effects of the elastic vibrations of the circular plate on triggering splashing. We concentrate on a parameter regime where the plate has a relatively high rigidity so that rather than simply being deformed by the impact it can vibrate. The period of the substrate vibration is of the order of the duration of the impact stage, and deflections of the elastic plate remain small. Vibration of the substrate and the liquid flow in the impacting droplet are coupled through the hydrodynamic pressure and the kinematic boundary condition on the wetted part of the substrate. The effects of viscosity, surface tension and gravity are assumed to play a negligible role during the early stages of impact. We assume the conditions are such that the flow caused by the impact is inertia driven, and described by the theory of potential flow. The gas surrounding the droplet is also not taken into account. The axisymmetric problem of a liquid droplet

impacting onto a partly elastic substrate is formulated in non-dimensional variables. The liquid drop is taken to be spherical before impact, with radius  $R$ . The impact speed  $V$  is constant. At the instant of impact ( $t = 0$ ), the drop touches the elastic circular plate at its central point. The circular elastic plate of radius  $L$  is housed in an otherwise rigid substrate, and is simply supported at its edge (see Figure 2.2.1). The liquid in the drop is assumed inviscid and incompressible, and the subsequent flow is irrotational and axisymmetric. The radius of the elastic plate,  $L$ , is assumed to be much smaller than the radius of the drop,  $R$ . The ratio

$$\epsilon = L/R, \quad (2.2.1)$$

is the small parameter in the present study.

The early stage of the impact with a strong coupling between the deflection of the elastic plate and the liquid motion is considered in this chapter. The dimensional scales are taken to be:  $L$  is the length scale,  $V$  is the velocity scale and  $\rho V^2 R/L$  is the pressure scale. The typical time scale  $T$  of this stage of the impact is taken as the time required for the elastic plate to be completely wetted. Geometrical considerations yield  $T = L^2/(VR)$ . The displacements of the plate deflection and of the free surface of the liquid drop are of order  $VT$ . All variables used later on in this chapter are non-dimensional unless explicitly stated otherwise.

The problem is studied by using the cylindrical coordinate system  $(r, z)$ . Initially,  $t = 0$ , the drop is spherical and touches the flat horizontal substrate,  $z = 0$ , at a single point which is taken as the origin of the coordinate system (see Figure 1). The initial surface of the drop is described by the equation

$$z = \frac{\epsilon}{2} (r^2 + z^2). \quad (2.2.2)$$

For mathematical convenience we chose a frame of reference where the droplet is initially at rest and the substrate hits the liquid drop at unit speed from below.

The position of the moving substrate is given by

$$z = \epsilon(t - w(r, t)), \quad (2.2.3)$$

where  $w(r, t)$  is the deflection of the elastic part,  $r < 1$ , of the substrate, and  $w(r, t) = 0$  elsewhere. The deflection  $w(r, t)$  is taken to be positive in the negative  $z$ -direction.

The flow in the droplet is described by the velocity potential  $\varphi(r, z, t)$ . The potential satisfies Laplace's equation in the flow region,  $\Omega(\epsilon, t)$ , and is subject to the kinematic boundary condition,

$$\varphi_z = \epsilon\eta_r\varphi_r + \eta_t, \quad (2.2.4)$$

on the free surface of the drop,  $z = \epsilon\eta(r, t)$ , where  $\eta(r, 0) = \frac{1}{2}r^2 + O(\epsilon)$  and  $r = O(1)$ . We require that the normal velocities of the liquid and solid substrate match along their interface, this is called the body boundary condition and takes the vector form

$$\nabla\varphi \cdot \hat{\mathbf{n}} = \mathbf{V}_b \cdot \hat{\mathbf{n}}, \quad (2.2.5)$$

where  $\hat{\mathbf{n}}$  is the unit normal to the moving boundary and  $\mathbf{V}_b$  is its velocity. This takes the form

$$\varphi_z = 1 - w_t - \epsilon w_r \varphi_r, \quad (2.2.6)$$

on the moving substrate (2.2.3), in the wetted region where  $r < a(t, \epsilon)$ . This wetted region is unknown in advance and should be found as part of the solution; the unknown function  $a(t, \epsilon)$  gives the radius of the contact region (neglecting the thin jet-sheet discussed later). The dynamic boundary condition on the free surface of the impacted drop is

$$p(r, \epsilon\eta(r, t), t) = 0, \quad (2.2.7)$$

where the hydrodynamic pressure  $p(r, z, t)$  is given by the Bernoulli equation,

$$p(r, z, t) = -\varphi_t - \frac{1}{2}\epsilon|\nabla\varphi|^2. \quad (2.2.8)$$

The plate deflection  $w(r, t)$  is taken to be described by the thin plate theory:

$$\alpha w_{tt} + \beta \nabla^4 w = p(r, \epsilon(t - w(r, t)), t), \quad (r \leq 1), \quad (2.2.9)$$

where

$$\alpha = \frac{\rho_p h}{\rho L}, \quad \beta = \frac{E h^3 \epsilon^2}{12(1 - \nu^2) \rho V^2 L^3}, \quad (2.2.10)$$

$\rho_p$  is the density of the elastic plate,  $h$  is the plate thickness,  $E$  is the Young modulus of the plate material, and  $\nu$  is the Poisson ratio. The parameter  $\alpha$  indicates the importance of the structural mass per unit area of the plate,  $\rho_p h$ , compared to the added mass of the liquid per unit area, which is of order  $O(\rho L)$ . The parameter  $\beta$  can be considered as the dynamic rigidity of the plate. This parameter depends on the elastic characteristics of the plate, speed of impact and the size of the drop. We assume that both  $\alpha$  and  $\beta$  are of order  $O(1)$  in the present analysis. For small  $\alpha$  and  $\beta$  the plate equation (2.2.9) should be investigated using asymptotic methods. If  $\alpha$  becomes very small then we can neglect the structural inertia by setting  $\alpha=0$ . However, this case requires an early time asymptotic analysis when  $t = o(\epsilon^2)$ . If  $\beta$  is small then a matched asymptotic analysis at the edges of the plate is required. Neither of these asymptotic analyses are performed in the present work. Outside of the wetted region,  $r > a(t, \epsilon)$ , the right-hand side in (2.2.9) is zero. We assume that the elastic plate is simply supported at  $r = 1$  and flat initially. Then the plate equation is to be solved subject to

$$w = 0, \quad w_{rr} + \frac{\nu}{r} w_r = 0, \quad (r = 1), \quad (2.2.11)$$

$$w(r, 0) = 0, \quad w_t(r, 0) = 0 \quad (r \leq 1). \quad (2.2.12)$$

The formulation of the fully coupled problem is completed by the initial conditions

$$\varphi(r, z, 0) = 0, \quad (2.2.13)$$

$$a(0, \epsilon) = 0, \quad (2.2.14)$$

$$\eta(r, 0) = \frac{1}{2}r^2 + O(\epsilon), \quad (2.2.15)$$

where  $r = O(1)$  and  $z = O(1)$ . The pressure  $p(r, z, t)$  in (2.2.7) and (2.2.8) does not account for ambient pressure, hydrostatic pressure and the pressure due to surface tension effects. The hydrostatic pressure is of order  $\rho g R$  which is much smaller than the pressure scale  $\rho V^2 R/L$  if  $\epsilon(gR/V^2) \ll 1$ . The surface tension can be neglected at leading order if  $\sigma/(\rho V^2 R) \ll 1$ , where  $\sigma$  is the coefficient of surface tension of the liquid. For a water droplet of density  $\rho = 1000 \text{ kg/m}^3$ , surface tension  $\sigma = 7.197 \times 10^{-2} \text{ N/m}$  and radius  $R = 5 \times 10^{-3} \text{ m}$  with  $g = 9.81 \text{ m/s}^2$  impacting an elastic circular disk of radius  $L = 1 \times 10^{-3} \text{ m}$  at velocity  $V = 1 \text{ m/s}$  we have  $\sigma/(\rho V^2 R) < 2 \times 10^{-4}$  and  $\epsilon(gR/V^2) < 10^{-2}$ . Hence we neglect surface tension and gravity as both provide smaller contributions to the hydrodynamic pressure compared to that from inertia.

The problem formulated above is strongly coupled. The plate deflection depends on the hydrodynamic loads through the right-hand side of (2.2.9), and both the hydrodynamic pressure (2.2.8) and the flow in the liquid droplet depend on the elastic deflection of the plate through the body boundary condition (2.2.6). The flow region,  $\Omega(\epsilon, t)$ , and the wetted area of the plate,  $r < a(t, \epsilon)$ , are unknown in advance and should be determined along with the hydrodynamic and structural characteristics of the problem.

The problem (2.2.2)-(2.2.15) can be simplified during the early stage of impact. The approximate solution can be obtained by asymptotic methods as  $\epsilon \rightarrow 0$ . Equations (2.2.2)-(2.2.3) show that the flow region can be approximated by the upper half-space,  $z > 0$ , to leading order, and the boundary conditions (2.2.4)-(2.2.7) can be linearised and imposed on the plane  $z = 0$ . In addition, the linearised dynamic condition (2.2.7) can be integrated in time using the initial

conditions. Below we keep the original notation of the unknown functions for their leading-order terms. At leading order, the hydrodynamic part of the problem reads

$$\nabla^2 \varphi = 0, \quad (z > 0), \quad (2.2.16)$$

$$\varphi = 0, \quad (z = 0, r > a(t)), \quad (2.2.17)$$

$$\varphi_z = 1 - w_t(r, t), \quad (z = 0, r \leq a(t)), \quad (2.2.18)$$

$$\varphi \rightarrow 0, \quad (r^2 + z^2 \rightarrow \infty), \quad (2.2.19)$$

where  $w(r, t) = 0$  for  $r > 1$ . The hydrodynamic pressure is given by the linearised Bernoulli equation,  $p(r, z, t) = -\varphi_t(r, z, t)$ . The plate equation (2.2.9) at leading order then becomes

$$\frac{\partial}{\partial t} (\alpha w_t(r, t) + \varphi(r, 0, t)) + \beta \nabla^4 w = 0, \quad (r < 1). \quad (2.2.20)$$

Equation (2.2.20) is solved subject to the boundary conditions (2.2.11) and initial conditions (2.2.12). The shape of the liquid free surface,  $z = \epsilon \eta(r, t)$ , is provided at leading order by  $\eta_t(r, t) = \varphi_z(r, 0, t)$ , where  $r > a(t)$ , which follows from the kinematic condition (2.2.4). Note that  $\eta(r, 0) \rightarrow r^2/2$  as  $\epsilon \rightarrow 0$ . The equations of flow, (2.2.16)-(2.2.19), and the equation of the plate deflection (2.2.20) at leading order are linear but still coupled.

The radius of the contact region between the liquid and substrate,  $r < a(t)$ , is determined by using the condition that the vertical coordinate of the free surface,  $z = \epsilon \eta(a(t), t)$  at the contact line  $r = a(t)$ , and the vertical coordinate of the elastic substrate (2.2.3) are equal, namely

$$\eta(a(t), t) = t - w(a(t), t). \quad (2.2.21)$$

Condition (2.2.21) is known as the Wagner condition [Wagner \[1932\]](#). The Wagner condition comes from assuming that the contact points This condition assumes that the free surface meets the impacting body at the turn over points. This

assumed that the spray jet is thin and can be neglected at leading order as  $\epsilon \rightarrow 0$ . To derive the Wagner condition we introduce the displacement potential  $\phi(r, z, t)$  which is the analog of velocity potential but for displacements and is related to the velocity potential via  $\dot{\phi} = \varphi$ . The governing equations for the displacement potential are

$$\nabla^2 \phi = 0, \quad (z > 0), \quad (2.2.22)$$

$$\phi = 0, \quad (z = 0, r > a), \quad (2.2.23)$$

$$\phi_z = t - w(r, t) - \frac{r^2}{2} = F(r, t), \quad (z = 0, r \leq a(t)), \quad (2.2.24)$$

$$\phi_r = 0, \quad (z = 0, r = 0), \quad (2.2.25)$$

$$\phi \rightarrow 0, \quad (r^2 + z^2 \rightarrow \infty). \quad (2.2.26)$$

The boundary value problem (2.2.22)-(2.2.26) is solved by introducing a new unknown function  $G(\lambda, a(t))$  such that

$$\phi(r, z, t) = \int_0^\infty G(\lambda, a) e^{-\lambda z} J_0(\lambda r) d\lambda. \quad (2.2.27)$$

By substituting the expression for  $\phi$  from equation (2.2.27) into the boundary conditions (2.2.23) and (2.2.24) we obtain the pair of equations

$$\int_0^\infty G_0(\lambda, a) J_0(\lambda r) d\lambda = 0, \quad (2.2.28)$$

$$\int_0^\infty G_0(\lambda, a) \lambda J_0(\lambda r) d\lambda = -F(r, t). \quad (2.2.29)$$

The set of equations (2.2.28)-(2.2.29) are solved by use of the Titchmarsh solution [McBride \[1979\]](#) giving

$$G_0(\lambda, a) = -\sqrt{\frac{2\lambda}{\pi}} \int_0^a x J_{\frac{1}{2}}(x\lambda) dx \int_0^x \frac{\rho F(\rho, t) d\rho}{\sqrt{x^2 - \rho^2}}. \quad (2.2.30)$$

By substituting  $G_0$  from equation (2.2.30) into the solution for  $\phi$  (2.2.27) and

rearranging integrals we find

$$\phi(r, 0, t) = -\frac{2}{\pi} \int_r^a \frac{dx}{\sqrt{x^2 - r^2}} \int_0^x \frac{\rho F(\rho, t)}{\sqrt{x^2 - \rho^2}} d\rho. \quad (2.2.31)$$

In order for the radial derivative at the contact line to be finite we require that

$$\int_0^a \frac{\rho F(\rho, t) d\rho}{\sqrt{a^2 - \rho^2}} = 0. \quad (2.2.32)$$

By making the obvious substitution we arrive at the form of the Wagner condition used throughout this chapter,

$$\int_0^{\frac{\pi}{2}} \sin(\theta) F(a(t) \sin(\theta), t) d\theta = 0, \quad (2.2.33)$$

Note that the radius of the contact region  $a(t)$  depends strongly on the plate deflection  $w(r, t)$ .

The hydrodynamic problem (2.2.16)-(2.2.19) is solved by the method of dual integral equations [McBride, 1979] and the plate deflection is obtained by the method of normal modes [Korobkin, 1998, Scolan, 2004] applied to the structural problem (2.2.20), (2.2.11), (2.2.12), where the radius  $a(t)$  of the contact region is determined by equation (2.2.33).

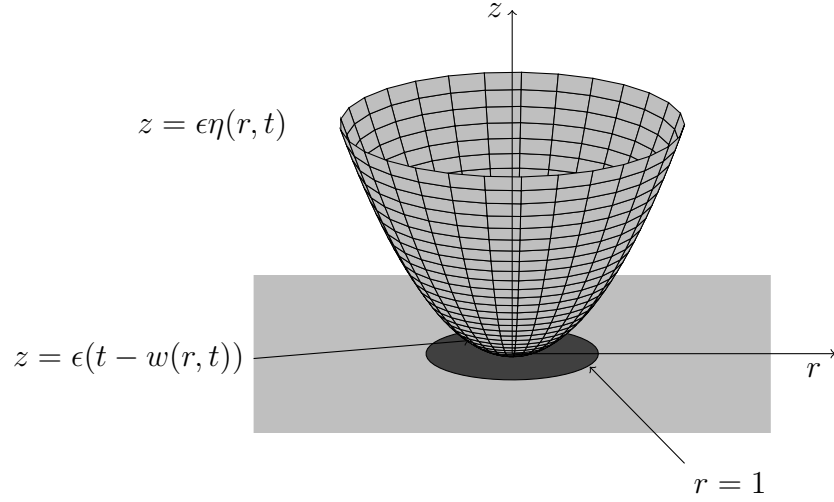


Figure 2.2.2: A sketch of the problem away from the contact region. The light grey paraboloid shows the liquid free surface  $z = \epsilon\eta(r, t)$ , the dark grey circle is the elastic plate with deformation  $z = \epsilon(t - w(r, t))$  and the light grey square region indicates the infinite rigid housing for the elastic plate.

### 2.3 Coupled problem of hydroelastic impact

The full formulated problem described above and given by (2.2.11)-(2.2.12), (2.2.16)-(2.2.33) is coupled. The hydrodynamic part of the problem (2.2.16) subject to (2.2.17)-(2.2.19), and the structural part of the problem (2.2.20), subject to (2.2.11)- (2.2.12) should be solved simultaneously, together with the Wagner condition (2.2.33) for the unknown radius of the contact region,  $a(t)$ .

#### Structural problem

It is convenient to introduce a new unknown function, called the auxiliary function

$$q(r, t) = -\frac{1}{\beta} (\alpha w_t(r, t) + \varphi(r, 0, t)), \quad (2.3.1)$$

where  $0 \leq r < 1$ , and to rewrite equation (2.2.20) as

$$q_t = \nabla^4 w, \quad \alpha w_t + \varphi(r, 0, t) = -\beta q(r, t). \quad (2.3.2)$$

Here  $\varphi(r, 0, t) = 0$ , where  $a(t) \leq r < 1$ , during the early stage when the elastic plate is only partly in contact with the liquid,  $a(t) < 1$ . Within the method of normal modes, the deflection  $w(r, t)$  and auxiliary function  $q(r, t)$  are sought in the forms

$$w(r, t) = \sum_{n=1}^{\infty} A_n(t) w_n(r), \quad (2.3.3)$$

$$q(r, t) = \sum_{n=1}^{\infty} k_n^4 q_n(t) w_n(r), \quad (2.3.4)$$

where  $A_n(t)$  and  $q_n(t)$  are the coefficients to be determined. The functions  $w_n(r)$  are the non-trivial bounded solutions to the homogeneous boundary value problem

$$\nabla^4 w_n = k_n^4 w_n, \quad r < 1, \quad (2.3.5)$$

$$w_n(1) = 0, \quad w_n''(1) + \nu w_n'(1) = 0, \quad (2.3.6)$$

and  $k_n$  are the corresponding eigenvalues. The functions  $w_n(r)$  describe the axisymmetric shapes of free vibrations of a circular simply supported plate with frequencies proportional to  $k_n^2$  [Leissa, 1969]. The solutions have the form

$$w_n(r) = J_0(k_n r) - \frac{J_0(k_n)}{I_0(k_n)} I_0(k_n r), \quad (2.3.7)$$

where  $k_n$  are the solutions of the equation

$$\frac{J_1(k_n)}{J_0(k_n)} + \frac{I_1(k_n)}{I_0(k_n)} = \frac{2k_n}{1 - \nu}, \quad (2.3.8)$$

with  $n \geq 1$  and  $k_{n+1} > k_n$ . Here  $J_n(r)$  and  $I_n(r)$  are the Bessel functions of the first kind and modified Bessel functions of the first kind of order  $n$  respectively. The functions (2.3.7) are orthogonal but not normalised

$$\int_0^1 w_n(r) w_m(r) r dr = U_n \delta_{nm}, \quad (2.3.9)$$

where  $U_n$  are given in Appendix A, and where  $\delta_{nm} = 0$  for  $n \neq m$  and  $\delta_{nn} = 1$ .

### 2.3.1 Coupled problem

The first equation in (2.3.2) and equations (2.3.3), (2.3.4) together with initial conditions (2.2.12) provide the system of ordinary differential equations for the vector  $\mathbf{q}(t) = \{q_1(t), q_2(t), \dots\}$ ,

$$\dot{\mathbf{q}} = \mathbf{A}(t), \quad \mathbf{q}(0) = 0, \quad (2.3.10)$$

where  $\mathbf{A}(t) = \{A_1(t), A_2(t), \dots\}$  is the vector of coefficients in the series (2.3.3), and overdot stands for time derivative. The boundary problem (2.2.16)-(2.2.19) for the velocity potential  $\varphi(r, z, t)$  and the series for the plate deflection (2.3.3) lead to the following decomposition of the potential

$$\varphi(r, z, t) = \varphi_0(r, z, a) - \sum_{n=1}^{\infty} \dot{A}_n(t) \varphi_n(r, z, a). \quad (2.3.11)$$

Here  $\varphi_0(r, z, a)$  is the potential of the flow caused by the impact of the rigid circular disk of radius  $a$  with the condition on the disc,  $\varphi_{0,z}(r, 0, a) = 1$ . The potentials  $\varphi_n(r, z, a)$  satisfy (2.2.16) and (2.2.19), with the condition (2.2.18) becoming  $\varphi_{n,z}(r, 0, a) = w_n(r)$ , for  $r < a$ . Substituting (2.3.11) and (2.3.3) into the second equation of (2.3.2), multiplying both sides of this equation by  $w_m(r)r$  and integrating in  $r$  from 0 to 1 we find

$$\begin{aligned} \alpha \dot{A}_m U_m + \int_0^a \varphi_0(r, 0, a) w_m(r) r dr - \sum_{n=0}^{\infty} \dot{A}_n(t) \int_0^a \varphi_n(r, 0, a) w_m(r) r dr \\ = -\beta k_m^4 q_m(t) U_m, \end{aligned} \quad (2.3.12)$$

which can be written more concisely in vector form as

$$\dot{\mathbf{A}} = -(\mathbf{\Lambda} + \mathbf{W}(a))^{-1} (\mathbf{Z}\mathbf{q} - \mathbf{g}(a)), \quad \mathbf{A}(0) = 0. \quad (2.3.13)$$

Here  $\mathbf{\Lambda} = \text{diag}\{\alpha U_1, \alpha U_2, \dots\}$  and  $\mathbf{Z} = \text{diag}\{\beta k_1^4 U_1, \beta k_2^4 U_2, \dots\}$  are diagonal matrices. The elements of the vector  $\mathbf{g}(a)$  are

$$g_n(a) = - \int_0^a \varphi_0(r, 0, a) w_n(r) r dr, \quad (2.3.14)$$

and the symmetric matrix of added masses  $W(a)$  has the elements

$$W_{nm}(a) = - \int_0^a \varphi_n(r, 0, a) w_m(r) r dr. \quad (2.3.15)$$

The system of ordinary differential equations (2.3.10) and (2.3.13) is valid for  $a \leq 1$ . For the later stages, when  $a(t) > 1$  and the elastic plate is completely wetted, we should change the upper limits in (2.3.14) and (2.3.15) to 1 and set  $w_n(r) = 0$ , where  $r > 1$  in the boundary conditions for the potentials  $\varphi_n(r, z, a)$ . The coefficients in (2.3.13) depend on the radius of the wetted area,  $a(t)$ , which is defined by equation (2.2.33). Substituting for  $F(r, t)$  and the series (2.3.3) in (2.2.33), we find

$$t - \frac{1}{2} a^2(t) \int_0^{\frac{\pi}{2}} \sin^3(\theta) d\theta - \sum_{n=1}^{\infty} A_n(t) \int_0^{\frac{\pi}{2}} \sin(\theta) w_n(a \sin(\theta)) d\theta = 0, \quad (2.3.16)$$

and then

$$a^2(t) = 3t - 3\mathbf{A}(t)\mathbf{Q}(a), \quad (2.3.17)$$

where

$$Q_n(a) = \int_0^{\frac{\pi}{2}} \sin(\theta) w_n(a \sin(\theta)) d\theta = \frac{1}{a} \int_0^a \frac{\rho w_n(\rho) d\rho}{\sqrt{a^2 - \rho^2}}. \quad (2.3.18)$$

Note that  $w_n(a \sin(\theta)) \equiv 0$  where  $a \sin(\theta) > 1$ . The system (2.3.10), (2.3.13) and (2.3.17) can be solved numerically once the integrals (2.3.14), (2.3.15) and (2.3.18) are known explicit functions of  $a$ . The functions  $Q_n(a)$  and  $g_n(a)$  are evaluated in Appendices B and C respectively.

### 2.3.2 Hydrodynamic problem

The hydrodynamic problem (2.2.16)-(2.2.19), together with the decomposition (2.3.11), leads to two mixed boundary value problems. The rigid part of the decomposition (2.3.11) becomes

$$\nabla^2 \varphi_0 = 0, \quad (z > 0), \quad (2.3.19)$$

$$\varphi_0 = 0, \quad (z = 0, r > a(t)), \quad (2.3.20)$$

$$\varphi_{0,z} = 1, \quad (z = 0, r \leq a(t)), \quad (2.3.21)$$

$$\varphi_0 \rightarrow 0, \quad (r^2 + z^2 \rightarrow \infty), \quad (2.3.22)$$

whilst the elastic part of the decomposition requires

$$\nabla^2 \varphi_n = 0, \quad (z > 0), \quad (2.3.23)$$

$$\varphi_n = 0, \quad (z = 0, r > a(t)), \quad (2.3.24)$$

$$\varphi_{n,z} = w_n(r), \quad (z = 0, r \leq a(t)), \quad (2.3.25)$$

$$\varphi_n \rightarrow 0, \quad (r^2 + z^2 \rightarrow \infty), \quad (2.3.26)$$

where  $n \geq 1$ .

These mixed boundary value problems are solved through the use of Hankel transformations. Equations (2.3.19) and (2.3.22) give

$$\varphi_0(r, z, a) = \int_0^\infty G_0(\lambda, a) e^{-\lambda z} J_0(\lambda r) d\lambda, \quad (2.3.27)$$

where  $G_0(\lambda, a)$  is a new unknown function. Substituting (2.3.27) in the boundary conditions (2.3.20) and (2.3.21) gives us the dual integral equations

$$\int_0^\infty G_0(\lambda, a) J_0(\lambda r) d\lambda = 0, \quad r > a \quad (2.3.28)$$

$$\int_0^\infty G_0(\lambda, a) \lambda J_0(\lambda r) d\lambda = -1, \quad r \leq a. \quad (2.3.29)$$

These equations are solved by using the Titchmarsh solution [McBride, 1979]

giving,

$$G_0(\lambda, a) = -\sqrt{\frac{2\lambda}{\pi}} \int_0^a x J_{\frac{1}{2}}(x\lambda) dx \int_0^x \frac{\rho d\rho}{\sqrt{x^2 - \rho^2}}. \quad (2.3.30)$$

Equations (2.3.27) and (2.3.30) yield the expression

$$\varphi_0(r, 0, a) = -\sqrt{\frac{2}{\pi}} \int_0^a \sqrt{x} dx \int_0^x \frac{\rho d\rho}{\sqrt{x^2 - \rho^2}} \int_0^\infty \sqrt{\lambda} J_0(\lambda r) J_{\frac{1}{2}}(\lambda x) d\lambda. \quad (2.3.31)$$

This can be integrated directly (with the  $\lambda$  integral given by 6.575.1 of [Gradshteyn and Ryzhik \[2007\]](#)) to give an explicit expression for the rigid velocity potential evaluated on  $z = 0$ ,

$$\varphi_0(r, 0, a) = -\frac{2}{\pi} \sqrt{a^2 - r^2}, \quad (r \leq a). \quad (2.3.32)$$

The elastic part of the problem (2.3.23)-(2.3.26) is solved using the same method.

The elastic terms of the velocity potential,  $\varphi_n(r, 0, a)$ , are given by

$$\varphi_n(r, 0, a) = -\frac{2}{\pi} \int_r^a \frac{dx}{\sqrt{x^2 - r^2}} \int_0^x \frac{\rho w_n(\rho) d\rho}{\sqrt{x^2 - \rho^2}}. \quad (2.3.33)$$

By using (2.3.18) we can express (2.3.33) as

$$\varphi_n(r, 0, a) = -\frac{2}{\pi} \int_r^a \frac{x Q_n(x) dx}{\sqrt{x^2 - r^2}} = -\Phi_n(r, a), \quad (2.3.34)$$

and (2.3.11) as

$$\varphi(r, 0, a) = -\frac{2}{\pi} \sqrt{a^2 - r^2} + \sum_{n=1}^{\infty} \dot{A}_n(t) \Phi_n(r, a), \quad (r \leq a). \quad (2.3.35)$$

The added mass elements (2.3.15) then become

$$W_{nm} = \frac{2}{\pi} \int_0^a \left( \int_r^a \frac{x Q_n(x) dx}{\sqrt{x^2 - r^2}} \right) w_m(r) dr = \frac{2}{\pi} \int_0^a x^2 Q_n(x) Q_m(x) dx. \quad (2.3.36)$$

The integrals (2.3.36) are evaluated in Appendix D. Integrating in (2.3.34) by

parts, we obtain

$$\Phi_n(r, a) = \frac{2}{\pi} Q_n(a) \sqrt{a^2 - r^2} - \frac{2}{\pi} \int_r^a \sqrt{x^2 - r^2} Q_n'(x) dx, \quad (2.3.37)$$

where  $Q_n(a)$  is given by (2.3.18).

Equations (2.3.37) and (2.3.35) provide the behaviour of the velocity potential close to the contact line as  $r \rightarrow a(t)$ ,

$$\varphi(r, 0, t) = B(t) \sqrt{a(t) - r} + O\left((a - r)^{\frac{3}{2}}\right), \quad (2.3.38)$$

where

$$B(t) = \frac{2}{\pi} \sqrt{2a} \left( \sum_{n=1}^{\infty} \dot{A}_n(t) Q_n(a) - 1 \right). \quad (2.3.39)$$

Therefore the Wagner condition predicts a square-root singularity in the radial velocity of the flow in the main region,  $(\partial\varphi/\partial r)(r, 0, t)$ , and in the hydrodynamic pressure,  $p(r, 0, t) = -\partial\varphi/\partial t$ , at the contact line as  $r \rightarrow a(t)$ . The coefficient of this singularity,  $B(t)$ , depends on the plate deflection and is calculated as part of the solution in the main flow region. The Wagner condition is not valid at the periphery of the contact region. In Wagner-type problems, this singularity is resolved by introducing an inner region, the so called jet-root region, around the contact line [Howison et al., 1991]. This locally resolves the singularity by the presence of a thin jet running along the substrate. This local inner solution is discussed below.

## 2.4 Jet-root and jet regions

The dynamics of the jet sheet and its dependence on elastic oscillations of the plate play a key role in potential splashing of the droplet. We distinguish the jet-root region, which is in a small vicinity of the contact line and is characterised by large velocities and pressures there, and the jet itself. The equations governing the flows in both the jet-root region and the jet region are

derived by using stretched variables and asymptotic methods, see [Howison et al. \[1991\]](#) and [Oliver \[2002\]](#) for full details of the case for impact with a rigid substrate. The introduction of the jet-root region removes the singularity of the Wagner solution, and provides characteristics of the initiation of the thin jet sheet that spreads along the substrate.

### 2.4.1 Jet-root region

In order to resolve the singularity found in the leading order velocity and pressure at the contact line, we consider a local region around the contact line described by the stretched inner variables  $X, Z$  where

$$r = a(t) + \epsilon^2 X, \quad z = \epsilon(t - w(a, t)) + \epsilon^2 Z. \quad (2.4.1)$$

We also introduce the inner potential  $\phi(X, Z, t)$  by

$$\varphi = \epsilon(\phi(X, Z, t) + \dot{a}(t)X). \quad (2.4.2)$$

This inner potential describes the relative flow in the moving coordinate system  $(X, Z)$ , see [Howison et al. \[1991\]](#).

The original equations of the hydrodynamic problem (2.2.2)-(2.2.8) written in the inner variables (2.4.1) become at leading order as  $\epsilon \rightarrow 0$

$$\frac{\partial^2 \phi}{\partial X^2} + \frac{\partial^2 \phi}{\partial Z^2} = 0, \quad (\text{in the flow region}), \quad (2.4.3)$$

$$\frac{\partial \phi}{\partial n} = 0, \quad (\text{on the flow boundaries}), \quad (2.4.4)$$

$$\left(\frac{\partial \phi}{\partial X}\right)^2 + \left(\frac{\partial \phi}{\partial Z}\right)^2 = \dot{a}^2, \quad (\text{on the free surface}). \quad (2.4.5)$$

As illustrated in Figure 2.4.1, the free surface of the droplet turns over in the jet-root region producing the jet along the solid substrate.

Matching the outer velocity potential (2.3.38) and the inner velocity potential

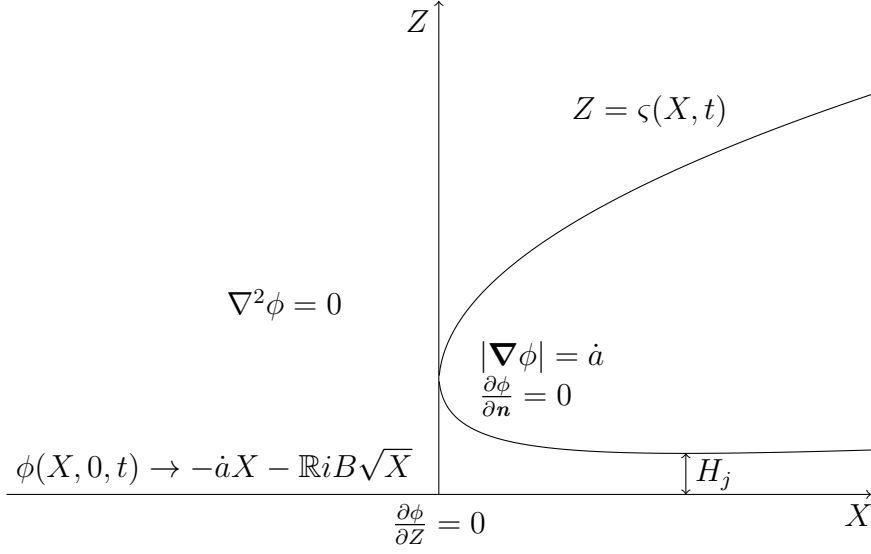


Figure 2.4.1: A sketch of the jet-root region problem.

(2.4.1) yields the far-field condition

$$\phi(X, 0, t) \approx -\dot{a}(t)X + B\sqrt{-X}, \quad (X \rightarrow -\infty), \quad (2.4.6)$$

along the wall and

$$\phi \approx -\dot{a}(t)X \quad \text{as} \quad X^2 + Z^2 \rightarrow \infty \quad (2.4.7)$$

along the free surface, where  $B(t)$  is given by (2.3.38). Equation (2.4.3) implies that the flow in the jet-root region is two-dimensional at leading order and the inner stream function  $\psi(X, Z, t)$  can be introduced. The boundary condition (2.4.4) requires that the stream function is constant along the solid boundary,  $Z = 0$ , and along the free surface,  $Z = \zeta(X, t)$ . The shape of the free surface,  $\zeta(X, t)$ , is unknown in advance and should be determined as part of the inner solution by using the dynamic boundary condition (2.4.5). The right-hand sides of (2.4.5) and (2.4.6) depend on time  $t$  through the speed of the contact line,  $\dot{a}(t)$ , and the coefficient  $B(t)$  given by (2.3.39). However, there are no time derivatives of the solution in the leading order inner problem (2.4.3)-(2.4.6). Therefore, the leading order inner flow is quasi-stationary, non-linear and two-dimensional in contrast to the flow in the main region, which is three-dimensional, linear and

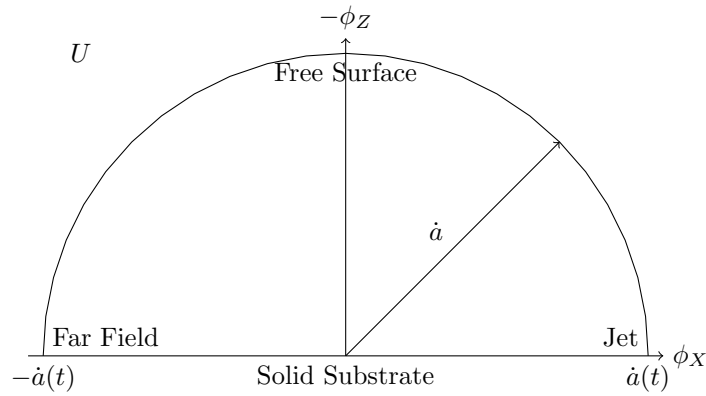


Figure 2.4.2: A sketch of the hodograph plane for the jet-root region  $U = \phi_X - i\phi_Z$ .

inertia driven. The solution of the inner problem (2.4.3)-(2.4.7) was given by Howison et al. [1991]. Here we are concerned only with the thickness of the jet,  $H_j(t)$ , and the speed of the jet, which are needed to integrate the equations of the jet dynamics introduced in the next subsection. In particular, we are interested in the effect of the elastic plate deflection on the quantities which enter this jet-root region via  $B(t)$  in (2.4.6)

The problem (2.4.3)-(2.4.7) can be formulated in terms of the complex potential,  $W = \phi + i\psi$ , as a function of the complex velocity  $U = dW/d\zeta = \phi_X - i\phi_Z$ , where  $\zeta = X + iZ$ . The flow region (see Figure 2.4.1) in the plane of the complex velocity corresponds to the semi-circle,  $\phi_X^2 + \phi_Z^2 < \dot{a}^2$ ,  $-\phi_Z > 0$ , see Figure 2.4.2. The far field of the flow region, where  $X^2 + Z^2 \rightarrow \infty$ , corresponds to the corner point  $U = -\dot{a}(t)$ , and the jet, where  $0 < Z < H_j$  and  $X \rightarrow +\infty$ , to the corner point  $U = \dot{a}(t)$ . The dynamic boundary condition (2.4.5) and the assumption that the jet thickness approaches a constant value  $H_j$  as  $X \rightarrow +\infty$  provide  $\phi_X \rightarrow \dot{a}(t)$  and  $\phi_Z \rightarrow 0$  in the jet as  $X \rightarrow +\infty$ . This result, along with equations (2.4.1)-(2.4.2), yields that the jet speed is double the speed of the contact line,  $2\dot{a}(t)$ , in the global coordinate system. The kinematic boundary condition (2.4.4) gives that the stream function  $\psi(X, Z, t)$  is independent of  $X$  and  $Z$  on the boundary of the flow region. We take  $\psi = 0$  on the solid boundary,  $Z = 0$ , and  $\psi = Q(t)$  on the free surface, where the function  $Q(t)$  is to be determined.

The horizontal velocity in the jet approaches  $\dot{a}(t)$  as  $X \rightarrow +\infty$ , see Figure 2.4.1, which gives

$$\phi_X = \psi_Z \rightarrow \dot{a}(t). \quad (2.4.8)$$

Integrating this expression in  $Z$  across the jet (see Figure 2.4.1) and taking into account that  $\psi = 0$  at  $Z = 0$  and  $\psi = Q(t)$  on the free surface, we find

$$Q(t) = \dot{a}(t)H_j(t). \quad (2.4.9)$$

The complex potential  $W(U)$  is an analytic function in  $|U| < \dot{a}(t)$ ,  $\Im(U) > 0$ , satisfies the boundary conditions  $\Im(W) = 0$  on  $\Im(U) = 0$  and  $\Im(W) = Q(t)$  on  $|U| = \dot{a}(t)$ , and behaves as  $W \sim \frac{1}{4}\dot{a}B^2(t)(U + \dot{a})^{-2}$  as  $U \rightarrow -\dot{a}(t)$ . The latter behaviour follows from the far-field condition (2.4.6) written in terms of the complex potential. In addition  $dW/dU$  should be zero at the stagnation point, where  $U = 0$ . This condition follows from the equalities  $U = dW/d\zeta = dW/dU \cdot dU/d\zeta$  and the condition at the stagnation point,  $dU/d\zeta \neq 0$ . The solution is composed as the sum of two analytic functions,  $W(U) = W_1(U) + W_2(U)$ , such that

$$W_1(U) = -\frac{1}{4}B^2U(U + \dot{a})^{-2}, \quad W_2(U) = -\frac{2}{\pi}Q(t)\ln\left(\frac{\dot{a} - U}{\dot{a} + U}\right), \quad (2.4.10)$$

where  $W_1(U)$  has the required behaviour close to  $U = -\dot{a}(t)$  and  $\Im(W_1) = 0$  on the boundary of the flow region in the  $U$ -plane, and  $W_2(U)$  satisfies the boundary condition for  $W(U)$  on  $|U| = \dot{a}(t)$ . Close to the stagnation point,  $U = 0$ , these functions behave as

$$W_1(U) \sim -\frac{B^2U}{4\dot{a}^2}, \quad W_2(U) \sim \frac{4}{\pi}\frac{Q(t)}{\dot{a}}U. \quad (2.4.11)$$

The condition that  $dW/dU = 0$  at the stagnation point is satisfied if

$$Q = \frac{\pi}{16}\frac{B^2}{\dot{a}}. \quad (2.4.12)$$

This equation together with (2.4.9) provide the jet thickness

$$H_j(t) = \frac{\pi}{16} \frac{B^2}{\dot{a}^2}. \quad (2.4.13)$$

Without the elastic deflection of the plate,  $A_j(t) = 0$  in (2.3.17) and (2.3.39), we find  $a(t) = \sqrt{3t}$  and  $B = -2\sqrt{2a}/\pi$  in the non-dimensional variables. Then the jet thickness (2.4.13) is equal to  $2t^{3/2}/(\sqrt{3}\pi)$ . In the dimensional variables the jet thickness at the entrance to the jet is  $2R(Vt_d/R)^{3/2}/(\sqrt{3}\pi)$ , where  $t_d$  is the dimensional time and  $Vt_d$  is the displacement of the droplet. The obtained results are in agreement with the results by Korobkin and Scolan [2003] in the problem of an elliptic paraboloid impact onto the flat water surface. Note that the uniform velocity in the jet,  $\dot{a}(t)$ , and the constant jet thickness  $H_j$  are approached exponentially quickly as  $X$  increases. In particular,  $\phi_X(X, 0, t) = \dot{a}(t) + O(\exp[-\pi X/2H_j])$  as  $X \rightarrow +\infty$  along the plate. The pressure in the jet-root region is much greater than in the main flow region with  $p = \dot{a}^2/(2\epsilon)$  at the stagnation point. However, the hydrodynamic pressure approaches zero in the jet exponentially quickly as  $X \rightarrow +\infty$ .

## 2.4.2 Jet region

As the flow leaves the jet-root region with  $X \rightarrow +\infty$  it enters a long thin jet sheet detailed here. Motivated by matching to the jet-root region, the axisymmetric flow in the jet sheet is described in cylindrical coordinates  $r, Z$  where  $z = \epsilon Z_p(r, t) + \epsilon^2 Z$ , with  $Z_p(r, t) = -w(r, t) + t$  and  $r > a(t)$ . The substrate corresponds to  $Z = 0$  in the new coordinates, and the free surface of the jet sheet is  $Z = h(r, t)$ . The size of the jet region in the radial direction is of order  $O(1)$  in the non-dimensional variables and it is the same as in the main flow region, see section ???. The vertical scale of the jet region is that of the jet-root region,  $O(\epsilon^2)$ . The horizontal speed of the flow,  $\varphi_r$ , at the entrance to the jet region,  $r = a(t)$ , is  $2\dot{a}(t)/\epsilon$  (see section 2.4.1). The initial thickness of the jet  $h(a(t), t)$  is given by  $H_j(t)$  from (2.4.13). We note here that the jet thickness

in the dimensional variables is  $L^3 h(r, t)/R^2$ .

To describe the flow in the jet region we introduce an inner velocity potential,  $\tilde{\phi}(r, Z, t, \epsilon)$ , defined by

$$\varphi(r, z, t) = \epsilon^{-1} \tilde{\phi}(r, Z, t, \epsilon), \quad (2.4.14)$$

in order to satisfy the matching condition with the horizontal velocity of the flow at the entrance to the jet region emanating from the jet-root.

The Laplace equation for the velocity potential in the inner stretched variables, the body boundary condition (2.2.6) and the kinematic boundary condition (2.2.4) become

$$\begin{aligned} \tilde{\phi} = & \tilde{\phi}_0(r, t) + \epsilon \tilde{\phi}_1(r, t) + \epsilon^2 \tilde{\phi}_2(r, t) + \epsilon^3 \left( \tilde{\phi}_3(r, t) + \left( Z_{p,t} + Z_{p,r} \tilde{\phi}_{0,r} \right) Z \right) \\ & + \epsilon^4 \left( \tilde{\phi}_4(r, t) + Z_{p,r} \tilde{\phi}_{1,r} Z - \frac{1}{2} \left( \tilde{\phi}_{0,rr} + \frac{1}{r} \tilde{\phi}_{0,r} \right) Z^2 \right) + O(\epsilon^5), \end{aligned} \quad (2.4.15)$$

$$h(r, t) = h_0(r, t) + \epsilon h_1(r, t) + O(\epsilon^2), \quad (2.4.16)$$

where the boundary-value problem for the velocity potential of order  $O(\epsilon^4)$  has a solution only if the leading order potential  $\tilde{\phi}_0$  and leading order jet thickness  $h_0(r, t)$  are related by

$$\frac{\partial h_0}{\partial t} + \frac{1}{r} \frac{\partial}{\partial r} \left( r \frac{\partial \tilde{\phi}_0}{\partial r} \frac{\partial h_0}{\partial r} \right) = 0. \quad (2.4.17)$$

This equation corresponds to the one-dimensional axisymmetric equation of mass conservation across the jet sheet. The Bernoulli equation (2.2.8) and the dynamic boundary condition (2.2.7) give the hydrodynamic pressure in the jet at leading order as

$$p(r, Z, t) = \epsilon^2 \left( h_0(r, t) - Z \right) \left( Z_{p,t} + Z_{p,r} \tilde{\phi}_{0,r} \right)_t + O(\epsilon^3), \quad (2.4.18)$$

and equations for the potentials  $\tilde{\phi}_n$ ,  $n = 0, 1, 2, 3, 4$ . In particular, at leading

order, we have

$$\tilde{\phi}_{0,t} + \frac{1}{2} \left( \tilde{\phi}_{0,r} \right)^2 = 0. \quad (2.4.19)$$

It is seen that the pressure distribution over the substrate in the jet region is proportional to the jet thickness and the vertical acceleration of liquid particles travelling along the moving substrate. Differentiating (2.4.19) with respect to  $r$  and introducing the leading-order radial velocity of the flow in the jet sheet,  $u(r, t) = \partial \tilde{\phi}_0 / \partial r$ , we arrive at the equations for the flow velocity in the jet,  $u(r, t)$ , and the jet thickness,  $h_0(r, t)$ ,

$$\frac{\partial h_0}{\partial t} + \frac{1}{r} \frac{\partial}{\partial r} (r u h_0) = 0, \quad (2.4.20)$$

$$\frac{\partial u}{\partial t} + u \frac{\partial u}{\partial r} = 0, \quad (2.4.21)$$

where  $r > a(t)$ . The boundary conditions for (2.4.20) and (2.4.21) are

$$u(a, t) = 2\dot{a}(t), \quad h_0(a, t) = H_j(t). \quad (2.4.22)$$

Equations (2.4.20) and (2.4.21) are the one-dimensional shallow water equations for axisymmetric flow without gravity. Equation (2.4.21) implies that liquid particles move in the jet at speeds which are independent of time. If a liquid particle has entered the jet sheet at a time instant  $\tau$  with speed  $2\dot{a}(\tau)$ , then this particle will be at the distance

$$r = a(\tau) + 2\dot{a}(\tau) (t - \tau), \quad (2.4.23)$$

at time  $t$ , where  $t \geq \tau$ .

To integrate equation (2.4.20), we introduce a new unknown function  $\tilde{h}(\tau, t) = h_0(r(\tau, t), t)$ , where  $r = r(\tau, t)$  is given by (2.4.23). Then using (2.4.20),

$$\frac{\partial \tilde{h}}{\partial t} = \frac{\partial h_0}{\partial t} + \frac{\partial h_0}{\partial r} \frac{\partial r}{\partial t} = - \left( u_r + \frac{u}{r} \right) \tilde{h}, \quad (2.4.24)$$

and

$$\frac{\partial \ln(\tilde{h})}{\partial t} = -\frac{\partial u}{\partial \tau} \frac{\partial \tau}{\partial r} - \frac{2\dot{a}(\tau)}{a(\tau) + 2\dot{a}(\tau)(t - \tau)}, \quad (2.4.25)$$

where  $\partial u / \partial \tau = 2\ddot{a}(\tau)$  and

$$\frac{\partial \tau}{\partial r} = \frac{1}{2\ddot{a}(\tau)(t - \tau) - \dot{a}(\tau)}. \quad (2.4.26)$$

This leaves

$$\frac{\partial \ln(\tilde{h})}{\partial t} = -\frac{1}{t - \tau - \dot{a}(\tau)/2\ddot{a}(\tau)} - \frac{1}{t - \tau + a(\tau)/2\dot{a}(\tau)}, \quad (2.4.27)$$

and then

$$\tilde{h}(\tau, t) \left| t - \tau - \frac{\dot{a}(\tau)}{2\ddot{a}(\tau)} \right| \left| t - \tau + \frac{a(\tau)}{2\dot{a}(\tau)} \right| = C(\tau), \quad (2.4.28)$$

where  $C(\tau)$  is a constant of integration and  $t > \tau$ . This solution and the initial condition,  $\tilde{h}(\tau, \tau) = H_j(\tau)$ , yield the jet sheet thickness as

$$h(r, t) = H_j(\tau) \left( 1 - \frac{2\ddot{a}(\tau)(t - \tau)}{\dot{a}(\tau)} \right)^{-1} \left( 1 + \frac{2\dot{a}(\tau)}{a(\tau)}(t - \tau) \right)^{-1}, \quad (2.4.29)$$

where  $r$  is given by (2.4.23).

This jet thickness has been derived under the assumption that the flow in the main region is described by the Wagner model of liquid impact. The Wagner model requires, in particular, that the contact region expands in time, namely that  $\dot{a}(t) > 0$ . Therefore  $1 + 2\dot{a}(\tau)(t - \tau)/a(\tau) \geq 1$  in (2.4.29). The last term in (2.4.29) describes a decrease of the jet thickness as the particles spread further from the contact line in order to conserve mass.

It can be seen from (2.4.29) that the jet thickness  $h(r, t)$  becomes large if the acceleration of the contact line  $\ddot{a}(\tau)$  is positive as  $\frac{2\ddot{a}(\tau)(t - \tau)}{\dot{a}(\tau)} \rightarrow 1$  at some time instant. This unbounded growth in  $h(r, t)$  violates the assumptions of our shallow water model as the vertical extent of the jet will grow beyond the  $O(\epsilon^2)$  thickness we have assumed. We interpret this break-down of the shallow water model as an indication of the onset of splashing. Note that the contact line acceleration

is strictly negative for a rigid substrate, where  $a(t) = \sqrt{3t}$ , see equation (2.3.17). In this case  $h(r, t)$  in (2.4.29) is always bounded, and the entire jet region is adequately described using the shallow water model. Once we include the elastic plate however, we find that the contact line acceleration  $\ddot{a}(t)$  can become positive, and splashing can be prompted in the jet region.

In light of this requirement on the contact line acceleration for a bounded solution, the jet thickness (2.4.29) yields conditions for when splashing might be observed. For negative acceleration  $\ddot{a}(\tau)$ , we have

$$1 - \frac{2\ddot{a}(\tau)(t - \tau)}{\dot{a}(\tau)} = 1 + \frac{2|\ddot{a}(\tau)|(t - \tau)}{\dot{a}(\tau)} \geq 1, \quad (2.4.30)$$

where  $t \geq \tau$ . If  $\ddot{a}(\tau) > 0$  for a certain  $\tau$ , then  $h(r, t) \rightarrow \infty$  as  $t \rightarrow t_c(\tau)$ , where  $t_c(\tau)$  is determined by the equation

$$\frac{2\ddot{a}(\tau)}{\dot{a}(\tau)}(t_c(\tau) - \tau) = 1, \quad (2.4.31)$$

and  $t_c(\tau) > \tau$ . For a given function  $a(\tau)$ , we need to find the minimum value,  $t_{min}$ , of the function  $t_c(\tau)$ . The solution (2.4.29) can be used only during the initial stage,  $0 < t < t_{min}$ . At  $t = t_{min}$  the solution (2.4.29) predicts the flow in the normal direction to the substrate, which is interpreted here as splashing of the droplet. The elastic plate motion affects the jet behaviour through the initial jet thickness,  $H_j$ , see equations (2.3.38) and (2.4.13) but also it is responsible for triggering splashing through the varying acceleration of the contact line.

To calculate  $t_{min}$  and the radius  $r_s$  at which the splashing occurs, we analyse the following function of  $\tau$ ,

$$\frac{1}{t_c(\tau)} = \frac{2\ddot{a}(\tau)}{\dot{a}(\tau) + 2\tau\ddot{a}(\tau)}, \quad (2.4.32)$$

and find its maxima there, where this function satisfies the inequality

$$0 < \frac{1}{t_c(\tau)} < \frac{1}{\tau}. \quad (2.4.33)$$

This approach provides a graphical way to find the time  $t_{min}$  and the corresponding value of  $\tau = \tau_{min}$ , such that  $t_c(\tau_{min}) = t_{min}$ . The radius  $r_s$  at which splashing occurs then follows from (2.4.23)

$$r_s = a(\tau_{min}) + \frac{\dot{a}^2(\tau_{min})}{\ddot{a}(\tau_{min})}. \quad (2.4.34)$$

## 2.5 Numerical solution

The system (2.3.10), (2.3.13) and (2.3.17) which describes the response of the elastic plate and the flow in the main flow region, is solved numerically. Note that the right-hand sides of (2.3.10) and (2.3.13) depend on the unknown vector-functions  $\mathbf{q}$ ,  $\mathbf{A}$  and the radius of the contact region  $a(t)$ , where  $da/dt > 0$  during the impact stage. It is convenient numerically to take the radius  $a$  as a new time-like variable and consider the time varying functions vectors  $\mathbf{q}$ ,  $\mathbf{A}$  as functions of  $a$ . Differentiating the Wagner condition, (2.3.17), with respect to time, we obtain

$$\frac{dt}{da} = \frac{\frac{2}{3}a + \mathbf{A} \cdot \mathbf{Q}'(a)}{1 - \dot{\mathbf{A}} \cdot \mathbf{Q}(a)} = G(\mathbf{A}, \mathbf{q}, a), \quad (2.5.1)$$

where  $\dot{\mathbf{A}}$  is given by (2.3.13). Note that  $G(\mathbf{A}, \mathbf{q}, a)$  does not depend on the unknown function  $t(a)$ . Next we multiply both sides of equations (2.3.10) and (2.3.13) by  $dt/da$  and use (2.5.1) to derive the equations for  $\mathbf{A}(a)$  and  $\mathbf{q}(a)$ :

$$\frac{d\mathbf{A}}{da} = -(\mathbf{\Lambda} + \mathbf{W}(a))^{-1} (\mathbf{Z}\mathbf{q}(a) - \mathbf{g}(a)) G(\mathbf{A}, \mathbf{q}, a), \quad (2.5.2)$$

$$\frac{d\mathbf{q}}{da} = \mathbf{A}(a)G(\mathbf{A}, \mathbf{q}, a). \quad (2.5.3)$$

The initial conditions for the system of ordinary differential equations (2.5.1)-(2.5.3) are

$$\mathbf{A} = 0, \quad \mathbf{q} = 0, \quad \text{at } t = 0 \text{ or } a = 0. \quad (2.5.4)$$

The initial value problem (2.5.1)-(2.5.4) is regular at  $a = 0$ . In particular,  $t = O(a^2)$ . The new time-like variable allows us to avoid difficulties with starting

simulations from  $t = 0$ , where  $da/dt \rightarrow \infty$  as  $t \rightarrow 0$ , see for example [Korobkin and Khabakhpasheva \[2006\]](#) for more detail. The system of ordinary differential equations (2.5.1)-(2.5.3) is truncated to  $N$  modes and integrated by using the fourth order Runge-Kutta scheme. In total  $2N + 1$  equations are integrated. The step of integration,  $\delta a$ , is related to the time step,  $\delta t$ , by equation (2.5.1),  $\delta t = G\delta a$ , where  $G = O(a)$  for small time. To properly capture the highest  $N$ th mode, the time step  $\delta t$  should be smaller than the non-dimensional period of the  $N$ th mode. The natural frequency of the  $N$ th mode is equal to  $(\beta/\alpha)^{\frac{1}{2}}k_N^2$ , which follows from the plate equation (2.2.9) and equation (2.3.5). The time step  $\delta t$  is at least six times smaller than the period of the  $N$ th mode if

$$\delta t < (\alpha/\beta)^{\frac{1}{2}}k_N^{-2}. \quad (2.5.5)$$

Correspondingly the step  $\delta a$  should be smaller than

$$\delta a < (\alpha/\beta)^{\frac{1}{2}}k_N^{-2}G^{-1}(\mathbf{A}, \mathbf{q}, a). \quad (2.5.6)$$

It is seen that the upper limit of the integration step  $\delta a$  depends on the solution through the speed of the contact radius  $da/dt = G^{-1}(\mathbf{A}, \mathbf{q}, a)$ . Initially the speed is very high, which makes it possible to use a relatively large step  $\delta a$ . However as the speed  $da/dt$  becomes small the right hand side in (2.5.6) decreases and this inequality requires a very small step of integration. In such conditions we swap between numerical stepping in contact line radius,  $a$ , and stepping in time,  $t$ , depending on the contact line velocity  $da/dt$ . We make this transition around  $da/dt = 2.5$ . If the stepping in time is used, the radius  $a(t)$  is obtained from the Wagner condition, (2.3.17), by a root finding method.

It was confirmed numerically that the solution converges with increasing number of modes and that the number of modes used in our calculations captures the physics of the full system with sufficient accuracy. We confirmed the convergence with number of modes by analysing, in particular, the behaviour of the added mass matrix,  $\mathbf{W}(a)$ . It was found that as the number of modes increases the

elements of the added mass matrix rapidly decay, as can be seen in the Appendix D, Figure D.0.1. The convergence with number of modes was found to be fairly good, with 10 modes providing very good accuracy during the impact stage with a partially wetted plate. Later, when the elastic plate is fully wetted, the method is found to have substantially better convergence, with 5 modes providing an adequate long term representation of the flow and plate deflection. This stems from the elastic effects (and hence the added mass contribution) becoming much less important compared with the rigid terms during the stage with a fully wetted plate .

Although the method of normal modes provides a good basis to investigate the velocity field in the droplet, plate deflection and elastic stresses, it does not allow us to accurately determine the pressure distribution over the wetted region. The pressure singularity at the contact line, coupled with poor convergence of the modal series for the plate acceleration  $w_{tt}(r, t)$ , make a series representation of the pressure impractical as discussed by Korobkin [1998]. However, our main goal in this paper is to study the effect of elasticity on the spreading and splashing of a droplet. We assume that the pressure in the wetted part of the substrate does not reduce to the vapour pressure due to the elastic plate vibration. Thus cavitation does not occur, and both the spreading and splashing of the droplet are not affected by finer details of the pressure distribution.

## 2.6 Results

Due to constraints of the Wagner model of liquid impact, simulations should be terminated if the contact region begins to shrink,  $da/dt < 0$ , or if the velocity of the contact region expansion becomes comparable with the speed of sound in the liquid for  $t > 0$ . This means that for some values of the parameters  $\alpha$  and  $\beta$  in (2.2.9) the simulations cannot be completed up to the time the plate is fully wetted. Figure 2.6.1 depicts the regions in the parameter plane  $(\alpha, \beta)$  where these two types of failure were found. The scales of the regions match those found

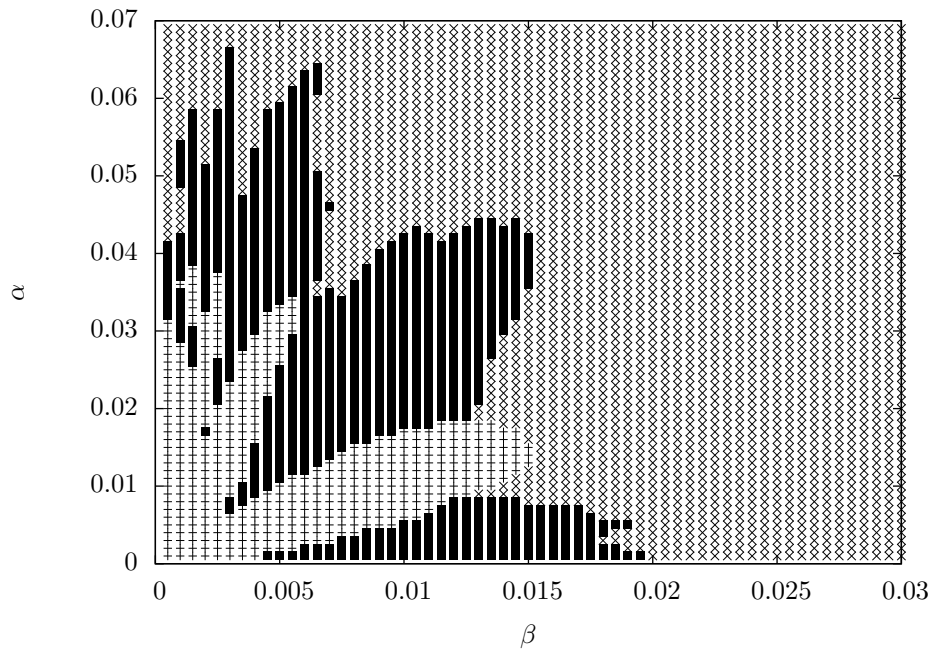


Figure 2.6.1: Parametric plane showing the regions of negative and unbounded contact line velocity. Pluses represent simulations which encountered contact line shrinkage, a cross represents a simulation with no problems and a filled circle represents a simulation with an unbounded contact line velocity.

by [Korobkin and Khabakhpasheva \[2006\]](#) in the corresponding two-dimensional problem of water wave impact onto a simply supported elastic plate. Figure 2.6.1 is obtained by integration of the system (2.5.1)-(2.5.3) in the interval  $0 < a \leq 1$  for values of  $\beta$  from 0.0005 to 0.016 in steps of 0.0005 and  $\alpha$  from 0.001 to 0.07 in steps of 0.001. It is seen that the regions of failure are limited to small values of both  $\alpha$  and  $\beta$ . The Wagner model can be used for any values of  $\beta$  if  $\alpha > 0.07$ . For an aluminium plate, with density  $\rho_p=2700 \text{ kg/m}^3$ , of radius  $L = 1 \text{ mm}$  and a water droplet of density  $\rho = 1000 \text{ kg/m}^3$ , this inequality provides the thickness of the plate as  $26\mu\text{m}$ .

To understand the physical reasons for the very small and very large velocities of the contact line for some conditions of the drop impact, note that the denominator in (2.5.1) is responsible for relative velocity of impact and the numerator for the relative angle between the initial shape of the droplet and the shape of the deformed elastic plate. This becomes more transparent if we return to the Wagner condition (2.2.33) for the radius of the contact region  $a(t)$ , differentiate it in time

and introduce the new variable of integration,  $r = a(t) \sin(\theta)$ ,

$$\frac{da}{dt} \cdot \frac{1}{a^2} \int_0^a \left( r + \frac{\partial w}{\partial r}(r, t) \right) \frac{r^2 dr}{\sqrt{a^2 - r^2}} = \frac{1}{a} \int_0^a \left( 1 - \frac{\partial w}{\partial t}(r, t) \right) \frac{r dr}{\sqrt{a^2 - r^2}}. \quad (2.6.1)$$

In (2.6.1),  $r$  in the first integral is equal to the slope of the initial shape of the droplet and  $\partial w/\partial r$  is the slope of the deformed plate in the contact region,  $0 < r < a$ . The integral on the left-hand side of (2.6.1) divided by  $a^2$  represents the averaged difference of the slopes with the weighting  $r^2/\sqrt{a^2 - r^2}$ . The weighting determines the relative importance of the local difference in slope. The weighting  $r^2/\sqrt{a^2 - r^2}$  indicates that the value of the integral depends mainly on the relative slope near the contact line. The same is valid for the integral on the right hand side of (2.6.1). This integral divided by  $a$  is the averaged relative velocity of the impact with weighting  $r/\sqrt{a^2 - r^2}$ . In the Wagner model of impact, both integrals should be positive. If the velocity of the plate deflection,  $\partial w/\partial t$ , becomes large and the integral in the right hand side of (2.6.1) approaches zero then  $da/dt$  also approaches zero and the contact region stops expanding. This type of failure is shown in Figure 2.6.1 by pluses. Another type of failure corresponds to the case where the slope of the deformed plate,  $-\partial w/\partial r$ , becomes large and approaches the slope,  $r$ , of the free surface of the undisturbed droplet. Then the integral on the left hand side of (2.6.1) approaches zero and  $da/dt \rightarrow \infty$ . Both types of failure occur at the later stage, when the main part of the elastic plate has been wetted. The first type of failure is illustrated by Figures 2.6.2 and 2.6.3 for  $\alpha = 0.01$  and  $\beta = 0.001$ . These values of the non-dimensional parameters  $\alpha$  and  $\beta$  imply that for the aluminium plate of radius 1 mm and droplet radius 5 mm, the impact speed is 9.67m/s and the elastic plate thickness is  $3.7\mu\text{m}$ . Figure 2.6.2 shows that the non-dimensional contact line speed,  $da/dt$ , for this elastic plate is smaller than that for the corresponding rigid substrate, and the contact line speed starts oscillating at  $a \approx 0.65$ , well before the plate is fully wetted. The averaged plate deflection and velocity,

$$\int_0^1 w(r, t) r dr, \quad \int_0^1 w_t(r, t) r dr, \quad (2.6.2)$$

are shown in Figure 2.6.3. Both the averaged deflection and velocity are very small for  $0 < a \leq 0.2$ . However, the plate deflection cannot be neglected even during this early stage. The effect of the plate deflection on the speed of the contact line is significant (see Figure 2.6.2). Note that the acceleration of the contact line,  $d^2a/dt^2$ , is always negative for rigid plates, but oscillates for an elastic plate.

The second type of failure is related to the shape of the deformed plate. The non-dimensional speed of the contact line and the shapes of the plate at time instants corresponding to the radius of the contact line with a step of 0.05 from  $a = 0$  to  $a = 0.9$  are shown in Figure 2.6.4 for  $\alpha = 0.005$  and  $\beta = 0.014$ . These values of  $\alpha$  and  $\beta$  correspond to an aluminium plate of radius 1 mm and the thickness  $2\mu\text{m}$  impacted by a droplet of water with radius 5 mm and speed 0.9 m/s. The speed of the contact line becomes unbounded shortly before the plate is completely wetted. While the elastic plate is partially wetted the contact region expands slower than for a rigid plate, which qualitatively agrees with the results by Pepper et al. [2008]. This is not typically true as the contact line approaches the edge of the plate. This phenomenon was not observed by Pepper et al. [2008], where an elastic film of large radius was considered. The early stages, where the wetted region is far smaller than the elastic plate, act as an approximation to the situation investigated by Pepper et al. [2008].

Since the slope of the substrate is discontinuous at the edge of the simply supported elastic plate, the contact line speed increases rapidly as the contact line passes over the edge of the plate. The present model can take the change in slope into account, as shown in Figure 2.6.5 for  $\alpha = 0.1$  ( $h = 36 \mu\text{m}$ ) and  $\beta = 0.02$  ( $V = 68 \text{ m/s}$ ). This Figure demonstrates that, as the contact line advances beyond the edge of the elastic plate the influence of the plate vibrations on the contact line velocity rapidly decays.

Figure 2.6.6 illustrates the method to determine the conditions of splashing, see section 2.4.2. Splashing occurs for any  $\tau$  such that the function  $1/t_c(\tau)$ , given by

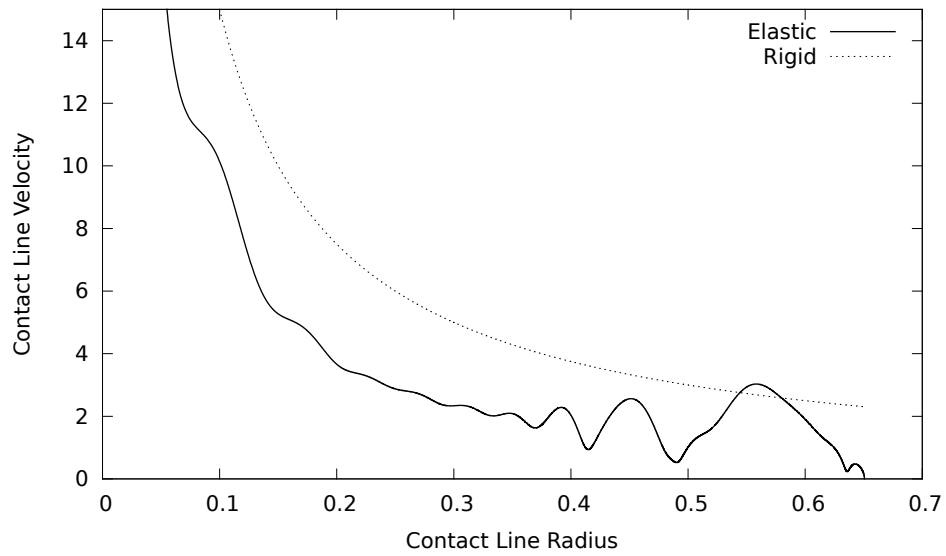


Figure 2.6.2: Contact line velocity  $da/dt$  for  $\alpha = 0.01$ ,  $\beta = 0.001$  as a function of the non-dimensional contact line radius  $a(t)$ .

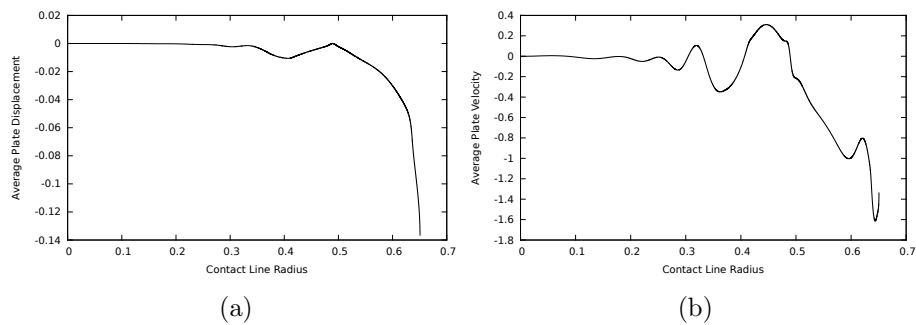


Figure 2.6.3: The averaged plate displacement (a) and averaged plate velocity (b) for  $\alpha = 0.01$ ,  $\beta = 0.001$  as functions of contact line radius  $a$ .

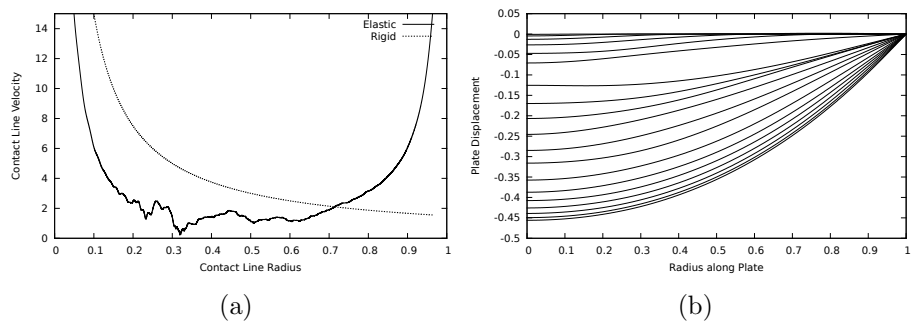


Figure 2.6.4: The contact line velocity (a) and plate shapes (b) calculated at intervals of  $a = 0.05$  for  $\alpha = 0.005$ ,  $\beta = 0.014$ .

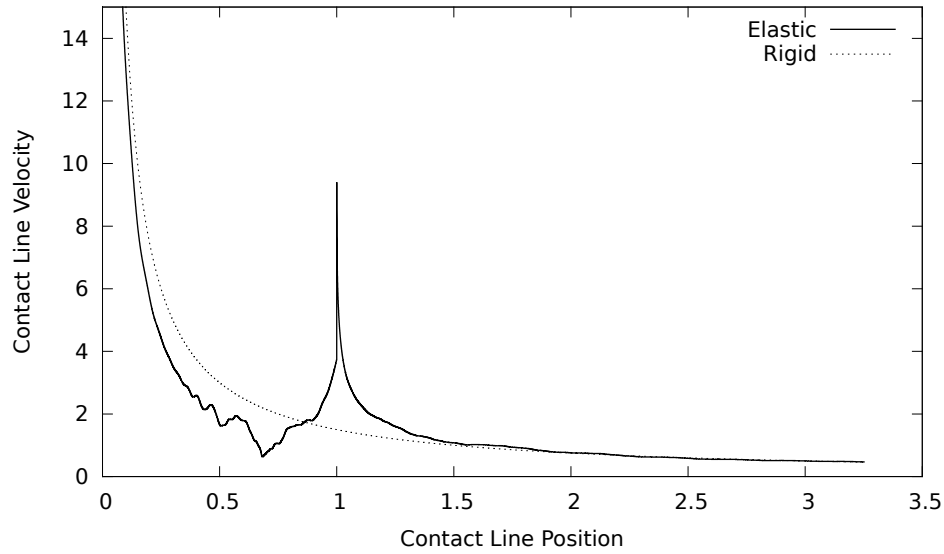


Figure 2.6.5: Contact line velocity  $da/dt$  for  $\alpha = 0.1$ ,  $\beta = 0.02$  as a function of contact line radius  $a$ .

(2.4.32) and shown in Figure 2.6.6 by the solid line, satisfies both inequalities in (2.4.33). The limits in (2.4.33) are shown by dotted lines in Figure 2.6.6. The earliest time of splashing,  $t_{min}$ , corresponds to the maximum of  $1/t_c(\tau)$  under conditions (2.4.33). This value is shown in Figure 2.6.6 by a circle. Splashing occurs also for liquid particles with their Lagrangian coordinates  $\tau$  around 0.2 and 0.35 but slightly later than for the earliest splash. For the parameters shown in Figure 2.6.6 we can see that the first splash occurs at  $\tau = 0.071$  and is seen around non-dimensional time  $t = 1/3.87 \approx 0.258$ . It is expected that surface tension, viscosity and some other factors not included in our model may smooth the predicted splash. Profiles of the jet thickness as functions of the radial coordinate  $r > a(t)$ , at  $t = 0.07, 0.12$  and  $0.19$  are shown in Figure 2.6.7a and in Figure 2.6.7b as functions of the Lagrangian coordinate  $\tau$  at different time instants. It is seen that the jet thickness decreases in front and behind the liquid particle at which splashing occurs.

The region of the parametric plane  $\alpha, \beta$ , where splashing can occur is large, see Figure 2.6.8, and include all cases studied above. As parameter pairs come closer to the edge of the splashing region the time in which we see the splash occur grows rapidly.

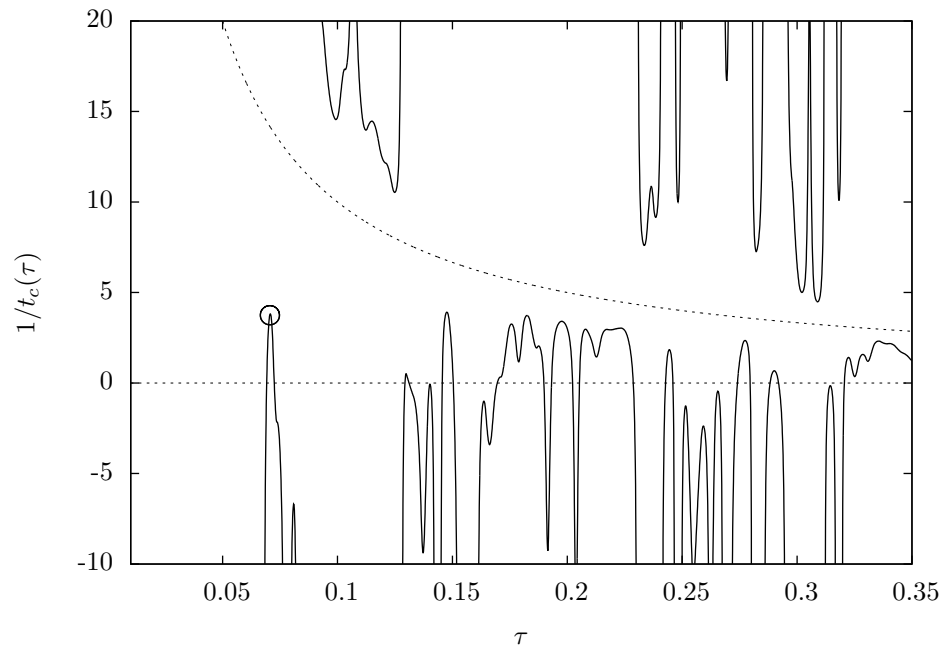


Figure 2.6.6: Plot of splashing conditions (2.4.32) and (2.4.33) for  $\alpha = 0.2$ ,  $\beta = 0.3$ . The circle indicates the value of  $\tau$  for which splashing first occurs.

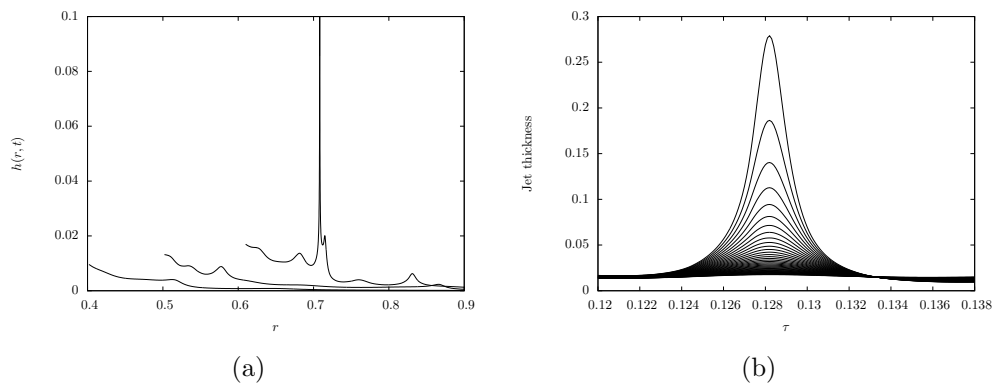


Figure 2.6.7: For the parameters  $\alpha = 0.1$  and  $\beta = 0.5$  (a) shows the jet thickness  $h(r, t)$  given by (2.4.29) as the function of  $r$ , where  $r > a(t)$  for  $t = 0.07, 0.12$  and  $0.19$ . Plot (b) shows the growth of the splash for the interval  $0.12 < \tau < 0.14$  of the Lagrangian coordinate  $\tau$ , from time  $t = 0.07$  to  $t = 0.18$  in steps of  $0.01$ . Increasing time is shown by increasing maximum in both plots.

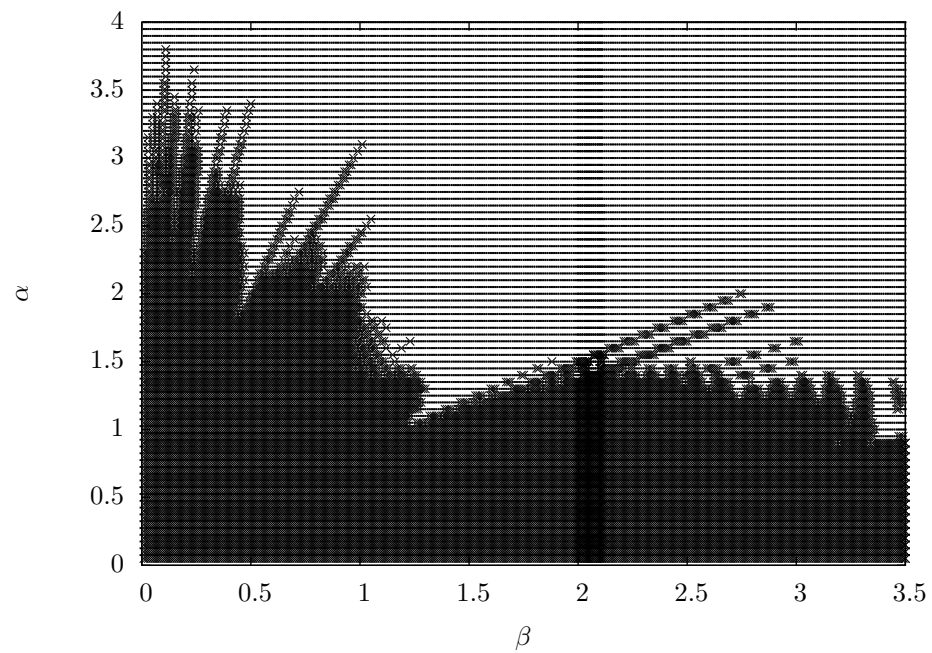


Figure 2.6.8: The  $\alpha - \beta$  parametric plot where splashing is predicted, the dark crossed region, and where it is not predicted, the dotted region.

# Impact of a droplet with a clamped elastic plate

---

In the previous chapter we analysed a liquid droplet impacting a simply supported elastic plate and found the inclusion of the plate was sufficient to cause splashing even when all other common mechanisms that cause splashing, such as the air, were neglected. In light of this result we now model the same situation as in chapter 2, with a change in the edge conditions from simply supported to clamped. This edge condition is more representative of a wide range of real world situations and is motivated by models of weld seams. It is common to model a welded joint using the edge condition (at the weld)

$$\frac{\partial^2 w}{\partial r^2} = h \frac{\partial w}{\partial r}, \quad (3.0.1)$$

where  $h$  is a positive real number [Narita, 1980]. The clamped and simply supported edge conditions act as limiting cases of this model. In this section we will model the plate using a clamped edge condition which, together with the previous section, provide results supporting the more physically relevant situation given by equation (3.0.1)

### 3.1 Problem formulation

We consider the normal impact of an axisymmetric liquid droplet of radius  $R$  with a circular elastic plate of radius  $L$  clamped at its edges to an otherwise rigid flat substrate. The droplet impacts at the centre of the elastic plate which is where we place origin of our cylindrical coordinate system with positive  $z$  pointing towards the incoming liquid droplet. The droplet impacts at a constant speed  $V$  and we assume the radius of the elastic plate to be much smaller than that of the droplet such that

$$\epsilon = L/R \ll 1. \quad (3.1.1)$$

As in the previous section we are interested in a short time after impact, motivating us to take the scales of  $L$  for length,  $V$  for velocity,  $\rho V^2 R/L$  for pressure,  $T = L^2/(VR)$  for time and  $VT$  for displacement. We use a frame of reference where the droplet is held at rest and the substrate move towards it. We introduce the velocity potential  $\varphi(r, z, t)$ , liquid pressure  $p(r, t)$  and elastic plate displacement  $w(r, t)$ . Following linearisation, see the previous section for details, the hydrodynamic part of our problem is formulated as

$$\nabla^2 \varphi = 0, \quad (z > 0), \quad (3.1.2)$$

$$\varphi = 0, \quad (z = 0, r > a(t)), \quad (3.1.3)$$

$$\varphi_z = 1 - w_t(r, t), \quad (z = 0, r \leq a(t)), \quad (3.1.4)$$

$$\varphi \rightarrow 0, \quad (r^2 + z^2 \rightarrow \infty), \quad (3.1.5)$$

with the elastic part being given by

$$\alpha w_{tt} + \beta \nabla^4 w = p(r, \epsilon(t - w(r, t)), t), \quad (r \leq 1), \quad (3.1.6)$$

$$w = 0, \quad w_r = 0, \quad (r = 1), \quad (3.1.7)$$

$$w(r, 0) = 0, \quad w_t(r, 0) = 0 \quad (r \leq 1). \quad (3.1.8)$$

In equations (3.1.2)-(3.1.8) we introduced the contact line  $r = a(t)$  and elastic parameters  $\alpha = \frac{\rho_p h}{\rho L}$  and  $\beta = \frac{Eh^3 \epsilon^2}{12(1-\nu^2)\rho V^2 L^3}$ . Note that the formulation (3.1.2)-(3.1.8) is identical to that used in the previous section except the elastic plate edge condition (3.1.7). As such, we solve the system of equations (3.1.2)-(3.1.8) in the same way as the previous section, using the method of dual integrals for the hydrodynamic problem and method of normal modes for the elastic one.

We begin by considering the elastic problem. We represent the elastic plate using a set of normal modes  $w_n(r)$  such that

$$w(r, t) = \sum_{n=1}^{\infty} A_n(t) w_n(r), \quad (3.1.9)$$

where the modes  $w_n(r)$  are the solutions to the problem

$$\nabla^4 w_n = k_n^4 w_n, \quad r < 1, \quad (3.1.10)$$

$$w_n(1) = 0, \quad w_n'(1) = 0, \quad (3.1.11)$$

with eigenvalues  $k_n$ . [Leissa \[1969\]](#) gives the solution of (3.1.10) as

$$w_n(r) = J_0(k_n r) - \frac{J_0(k_n)}{I_0(k_n)} I_0(k_n r), \quad (3.1.12)$$

with eigenvalues  $k_n$  given by

$$J_0(k_n) I_1(k_n) + I_0(k_n) J_1(k_n) = 0. \quad (3.1.13)$$

Note that the difference in plate boundary condition between this chapter and the previous has been captured purely by the frequencies of the modes, governed by equation (3.1.12). The equations governing the shape of the elastic modes in this section and the previous section, (3.1.12) and (2.3.7), are the same but the equations governing the frequencies (3.1.13) and (2.3.8) are different. The first 4 modes from equation (3.1.9) are plotted in Figure 3.1.1 for the clamped and simply supported boundary conditions. Note the difference in mode behaviour

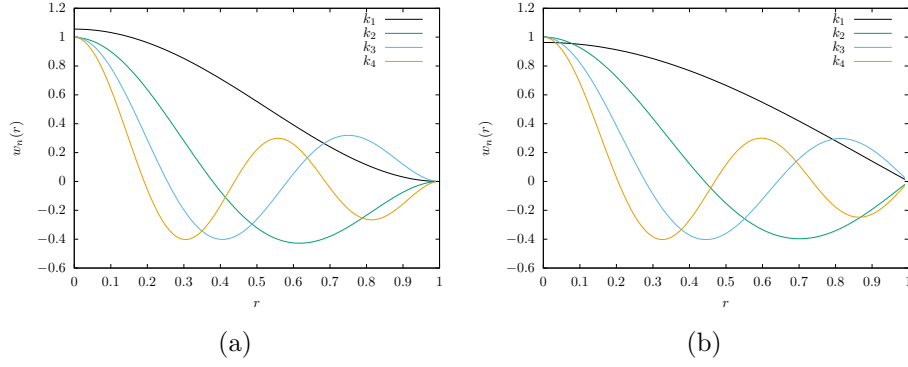


Figure 3.1.1: The first 4 normal modes for the clamped boundary condition (a) and simply supported (b).

near  $r = 1$ , this will be the factor driving any changes in our results presented in section 3.2. As such the equations governing the problem are the same, aside from (3.1.13), and are solved using the same methods as in the previous section. We use the same symbols as in that section, so that we have to solve

$$\dot{\mathbf{q}} = \mathbf{A}, \quad (3.1.14)$$

$$\dot{\mathbf{A}} = -(\mathbf{\Lambda} + \mathbf{W}(a))^{-1}(\mathbf{Z}\mathbf{q} - \mathbf{g}(a)), \quad (3.1.15)$$

subject to initial conditions

$$\mathbf{A}(0) = 0, \quad \mathbf{q}(0) = 0, \quad (3.1.16)$$

with the motion of the contact line being given by

$$a^2(t) = 3t - 3\mathbf{A}(t)\mathbf{Q}(a), \quad (3.1.17)$$

The change in plate boundary condition between this and the previous chapter does not affect the jet root or jet regions explicitly, so the jet sheet thickness will be given by

$$h(r, t) = H_j(\tau) \left(1 - \frac{2\ddot{a}(\tau)(t - \tau)}{\dot{a}(\tau)}\right)^{-1} \left(1 + \frac{2\dot{a}(\tau)}{a(\tau)}(t - \tau)\right)^{-1}. \quad (3.1.18)$$

The system of equations (3.1.14)-(3.1.15) is solved using the same set of numerical

methods as outlined in the previous chapter.

## 3.2 Results

We begin by analysing the contact line motion for a typical set of plate parameters. In Figure 3.2.1 we show the contact line motion for both a clamped and simply supported plate with the same set of parameters  $\alpha = \beta = 1.5$ . We can see that initially the contact line behaviour is similar for the simply supported and clamped elastic plate, however later on around  $a(t) = 0.6$  the contact line on the clamped plate speeds up relative to both the simply supported and rigid plates. As we can see from the plate shapes in Figure 3.2.10, as the contact line approaches the edge of the plate the clamped plate begins to decelerate while the simply supported plate is still accelerating downwards. This leads the contact line on the clamped plate to gain speed relative to the contact line on the simply supported plate.

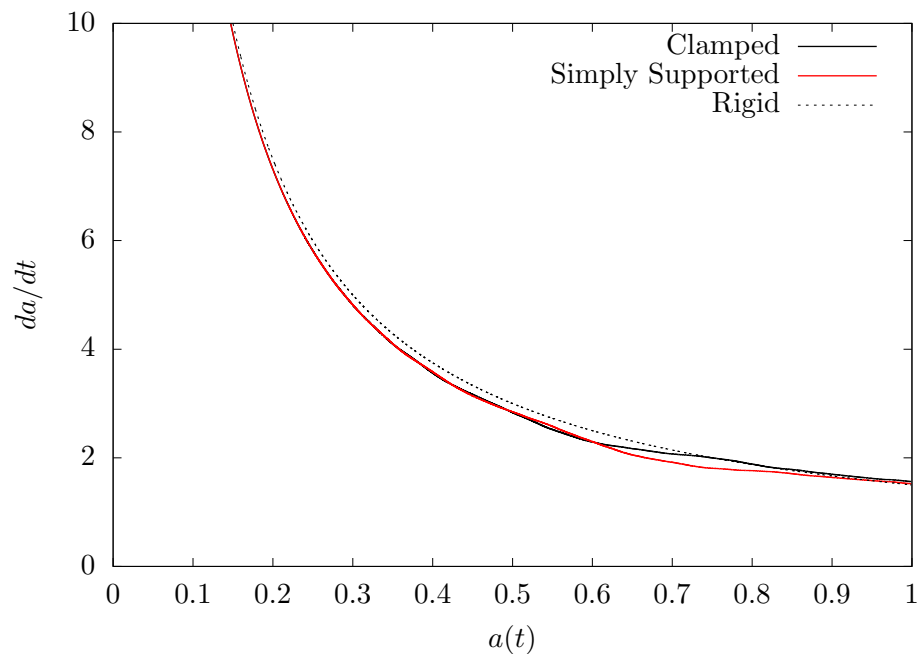


Figure 3.2.1: Contact line velocity against contact line position for the clamped, simply supported and rigid substrates. The elastic plates have parameters  $\alpha=1.5$ ,  $\beta=1.5$ .

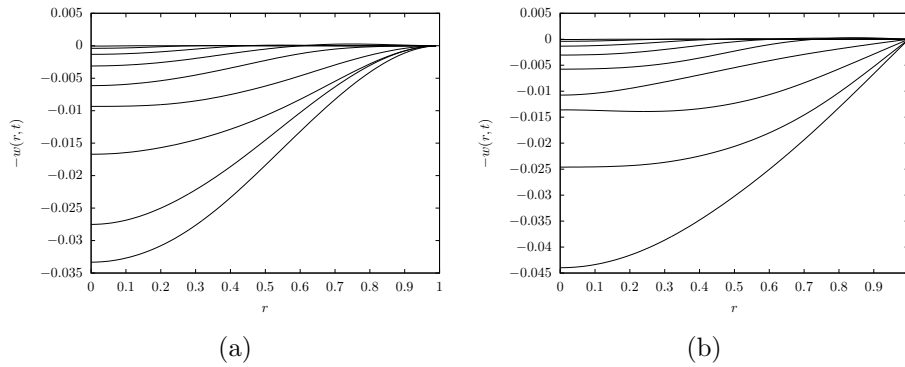


Figure 3.2.2: Plate shapes taken at snapshots of  $a = 0.1$  for the plate parameters  $\alpha = \beta = 1.5$ . Figure (a) is a clamped plate and Figure (b) simply supported

As with the previous section there is a range of plate parameters for which the contact line velocity either stops or grows extremely large. If either of these things happen we must immediately stop the numerics due to a break down in the Wagner model. In Figure 3.2.3 we show the regions where the contact line stops in blue stars and where the contact line velocity becomes extremely large in red crosses. When comparing Figure 3.2.3 to the equivalent for the simply supported plate, Figure 2.6.1 the parameter region where these break downs are encountered is much smaller for the clamped case. The shape of Figures 3.2.3 and 2.6.1 are qualitatively very similar.

In addition to the small parameter regimes shown in Figure 3.2.3 we can investigate a wide range of  $\alpha$  and  $\beta$ . We will do so while focusing on splashing as that was the key result from the previous chapter. Showing that elastic substrates can cause splashing, rather than simply reduce it as seen by Pepper et al. [2008] and Howland et al. [2016] is a key result. However the simply supported edge condition is less physically relevant than a clamped plate. Since the clamped plate is generally less responsive to the liquid droplet than a simply supported plate of the same parameters some changes in the splashing behaviour are expected. In Figure 3.2.4 we plot the conditions described in section 2.4.2 and by equation (2.4.33). Following those methods Figure 3.2.4 indicates that splashing does occur for this set of parameters and the time of splashing is  $t = 1/4.12 = 0.24$  occurring at Lagrangian coordinate  $\tau = 0.097$ . In

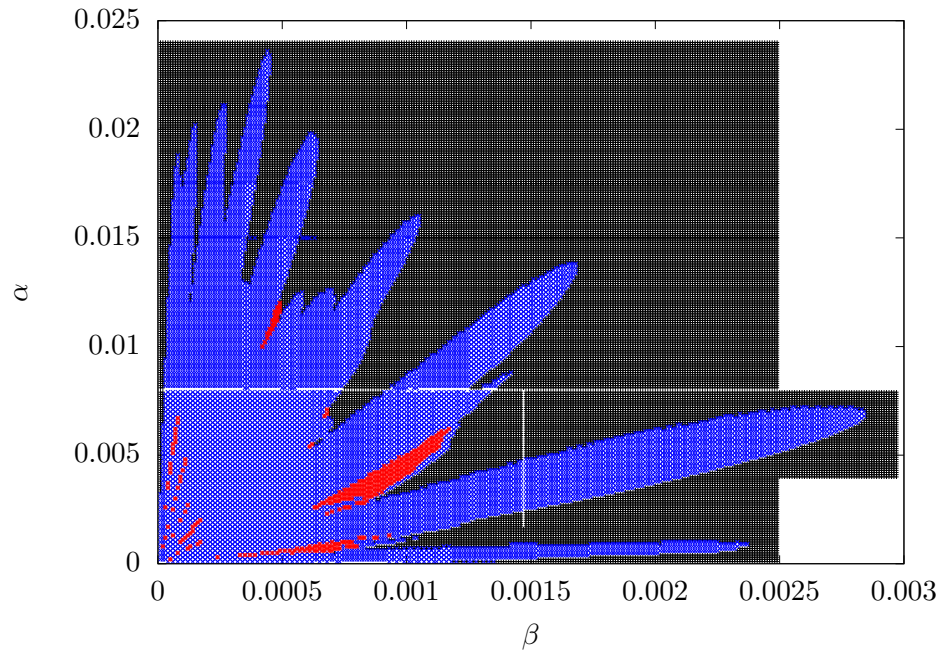


Figure 3.2.3: A parametric  $\alpha - \beta$  plot showing regions where the contact line velocity becomes zero (blue stars), very large (red crosses) and reaches the end of the plate with no issue (black pluses)

Figure 3.2.5 we show the jet profile corresponding to the splashing conditions in Figure 3.2.4. As we can see by comparing these two Figures to Figures 2.6.6 and 2.6.7 we see that the generation, growth and eventual splash of the jet has the same mechanism whether the plate is simply supported or clamped.

In Figure 3.2.6 we perform a parametric analysis, showing the regions of  $\alpha$  and  $\beta$  for which splashing is predicted. Compared with the same result for the simply supported plate Figure 2.6.8 we can see that splashing is far less common for the clamped plate. This is not unexpected as the time scale of the clamped plates oscillations is longer than that of the simply supported plate as evidence by the difference in  $k_1$  (3.196 for clamped and 2.222 for simply supported). This causes the clamped plate to become fully wetted quicker than the simply supported plate with the same parameters, for example for a plate with parameters  $\alpha = 0.1$  and  $\beta = 0.5$  the clamped plate is fully wetted at time  $t = 0.349$  and the simply supported plate at time  $t = 0.3977$ . Since the clamped plate has less influence over the motion of the contact line, and the clamped plate effect on the contact

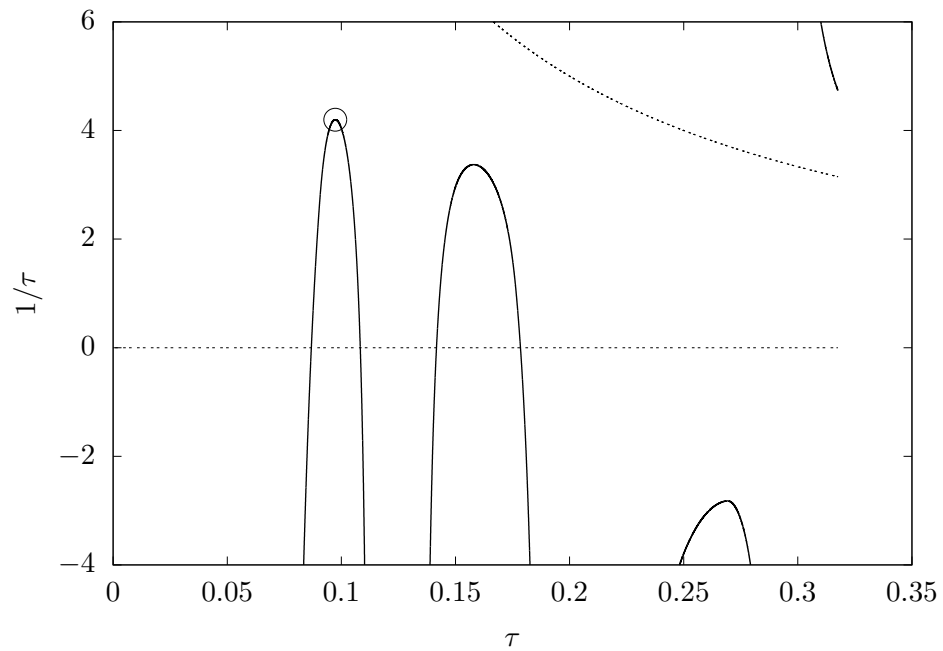


Figure 3.2.4: Plot of splashing conditions (2.4.33) for  $\alpha = 0.1$  and  $\beta = 0.5$ . The circle indicates the  $\tau$  at which splashing is first seen.

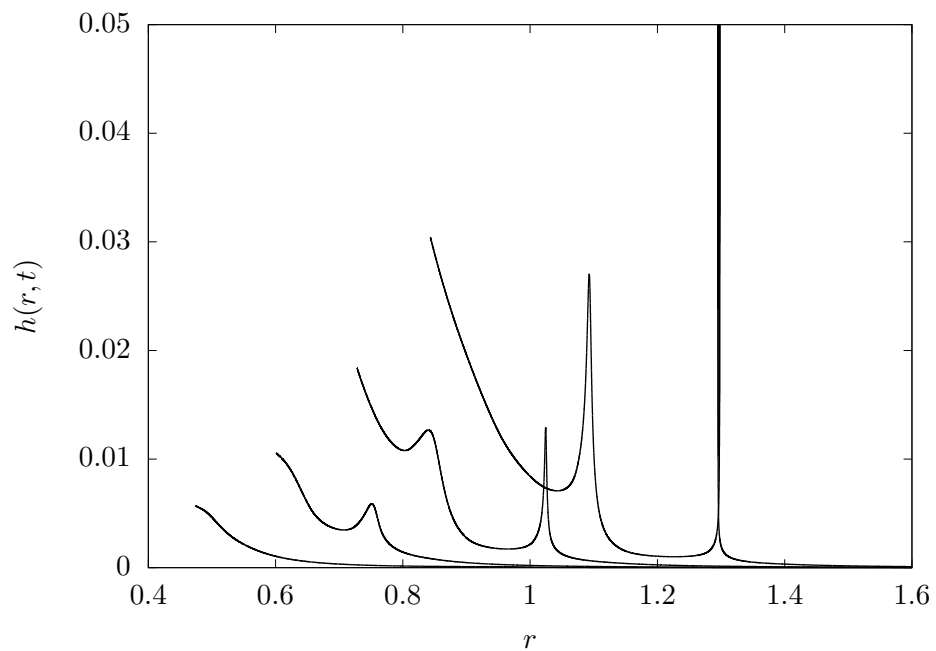


Figure 3.2.5: The shape of the jet at times  $t = 0.1, 0.155, 0.21, 0.265$  for plate parameters  $\alpha = 0.1$  and  $\beta = 0.5$

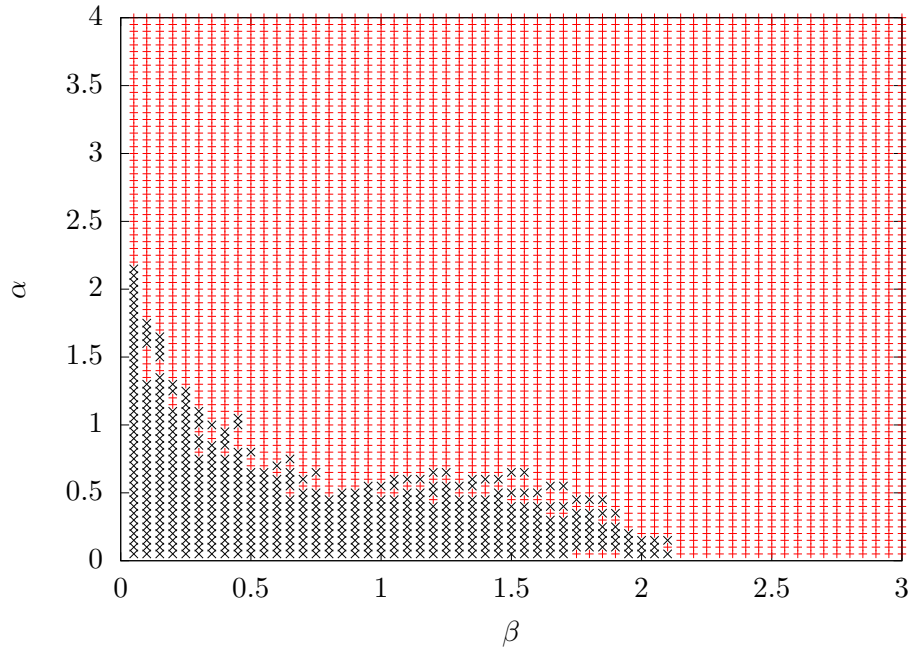


Figure 3.2.6: A parametric  $\alpha$ – $\beta$  plot showing regions where splashing is predicted (black crosses) and not predicted (red pluses)

line is the cause of splashing in our model, as discussed in the previous chapter, the reduction in the size of the  $\alpha$  –  $\beta$  region in which we predict splashing for a clamped plate makes sense. When comparing Figures 3.2.6 and 2.6.8 we can see that there are some areas in which splashing is predicted for both plate types, some where it doesn't happen in either as in Figure 3.2.1 and some where splashing is predicted for the simply supported plate but not the clamped plate. In Figure 3.2.7 we plot the contact line velocity against contact line position for  $\alpha = 1.5$  and  $\beta = 0.5$ . This pair of parameters are such that splashing is predicted to occur on the simply supported plate but not the clamped one. Although hard to see, the gradient of the clamped plate contact line velocity never becomes positive, however at  $a = 0.964$  the simply supported contact line have a small positive velocity, causing splashing. In Figure 3.2.9 we show the contact line velocity again but for this set of parameters ( $\alpha = 0.1$  and  $\beta = 0.5$ ) splashing is predicted for both the clamped and simply supported plate.

These results confirm the findings in the previous chapter in relation to the presence of an elastic plate causing splashing and extend them to a more

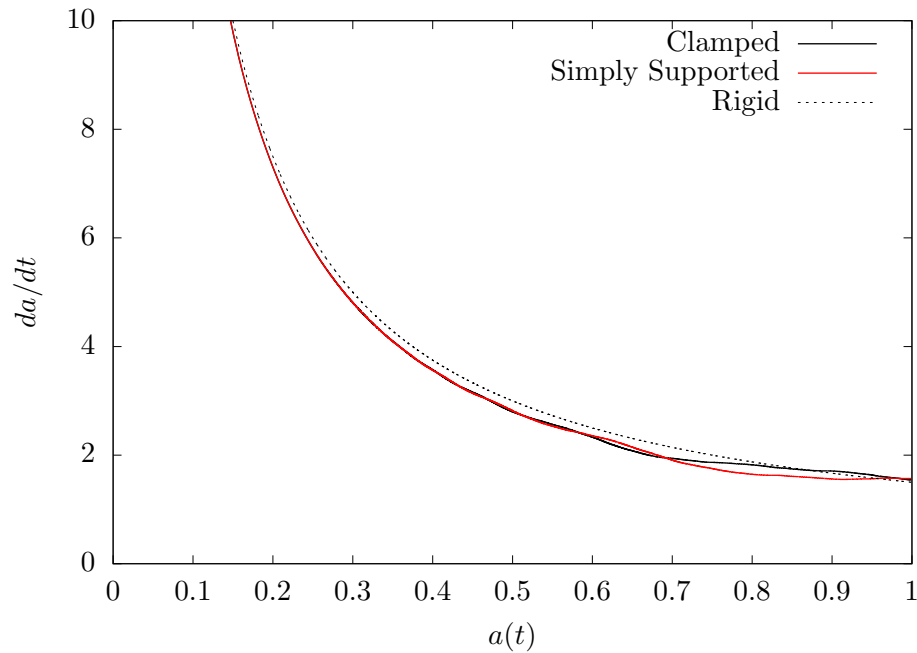


Figure 3.2.7: Contact line velocity for clamped, simply supported and rigid substrates. The elastic substrates have parameters  $\alpha = 1.5$  and  $\beta = 0.5$ . For these parameters a splash is predicted for the simply supported plate only.

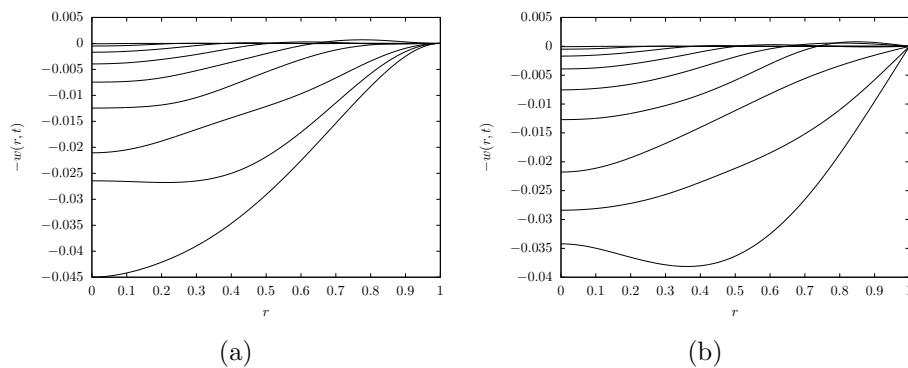


Figure 3.2.8: Plate shapes taken at snapshots of  $a = 0.1$  for the plate parameters  $\alpha = 1.5$  and  $\beta = 0.5$ . Figure (a) is a clamped plate and Figure (b) simply supported

physically relevant clamped plate. This provides experimentalists with a much simpler set up to test our findings, this is of great interest as previous experimental results surrounding deformable solids have shown a decrease in splashing, as opposed to our situation where we generate splashing purely due to the deformable substrate. By predicting splashing for both simply supported and clamped plates we also expect to see it for a plate with a welded edge, modelled by equation (3.0.1), although this is left as future work.

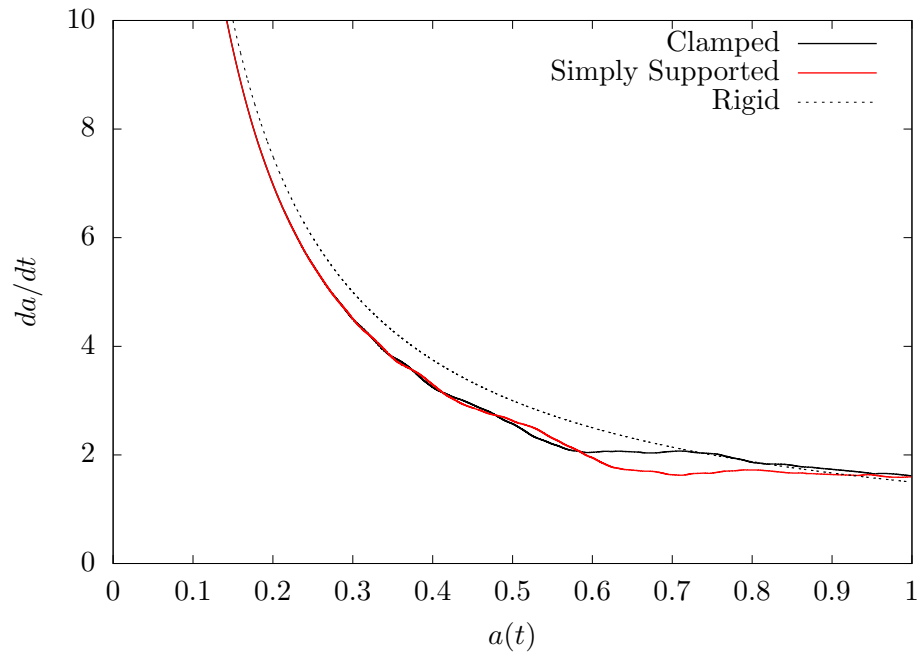


Figure 3.2.9: Contact line velocity for clamped, simply supported and rigid substrates. The elastic substrates have parameters  $\alpha = 0.1$  and  $\beta = 0.5$ . For these parameters a splash is predicted for both the simply supported and clamped plates.

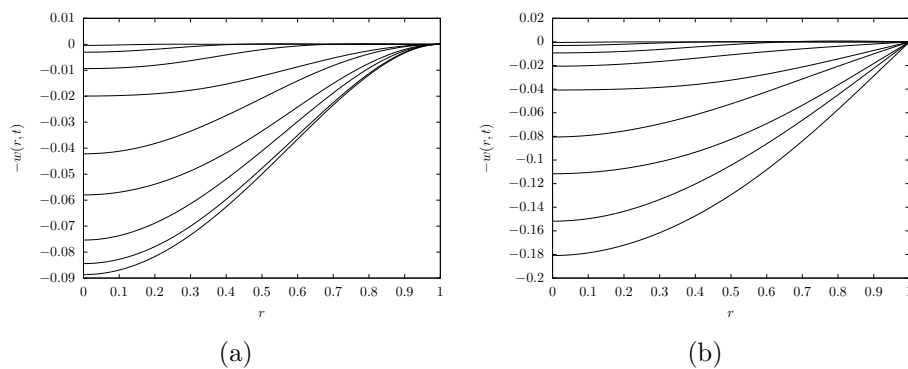


Figure 3.2.10: Plate shapes taken at snapshots of  $a = 0.1$  for the plate parameters  $\alpha = 0.1$  and  $\beta = 0.5$ . Figure (a) is a clamped plate and Figure (b) simply supported

# Air cushioning

---

## 4.1 Air cushioning with an elastic substrate

In this chapter we analyse the pre-impact deformation in a liquid free surface and elastic substrate due to the presence of a gas layer. A coupled lubrication style problem is derived from the dimensional Navier-Stokes equation and solved in section 4.1.2. The numerical methods used to solve the coupled lubrication problem are discussed in section 4.2 with validation presented in section 4.2.1. The touchdown point is investigated using asymptotic methods in section 4.2.2. Results and analysis are presented in section 4.3.

### 4.1.1 Problem Definition

We investigate the pre-impact gas cushioning behaviour of a droplet approaching touchdown onto a partially elastic substrate. We assume the two dimensional liquid droplet is initially a circle of radius  $R$  and approaches the substrate with a normal velocity  $U$ . Using a Cartesian coordinate system  $(x, y)$  with origin placed directly below the centre of the liquid droplet on the solid substrate. The time origin  $t = 0$  is the time at which an uncushioned droplet would first impact the solid substrate. The undisturbed liquid free surface  $f(x, t)$  is given by

$$y = f(x, t) = \pm\sqrt{R^2 - x^2} + R - Ut. \quad (4.1.1)$$

The substrate contains an elastic plate of length  $L \geq 0$  centred at  $x = x_0$ . The solid substrate is described by

$$y = W(x, t) = \begin{cases} 0 & x \leq x_0 - \frac{L}{2}, \\ w(x, t) & x_0 - \frac{L}{2} < x < x_0 + \frac{L}{2}, \\ 0 & x_0 + \frac{L}{2} \leq x, \end{cases} \quad (4.1.2)$$

where  $w(x, t)$  is the displacement of the elastic part of the substrate. A schematic of the problem geometry can be seen in Figure 4.1.1.

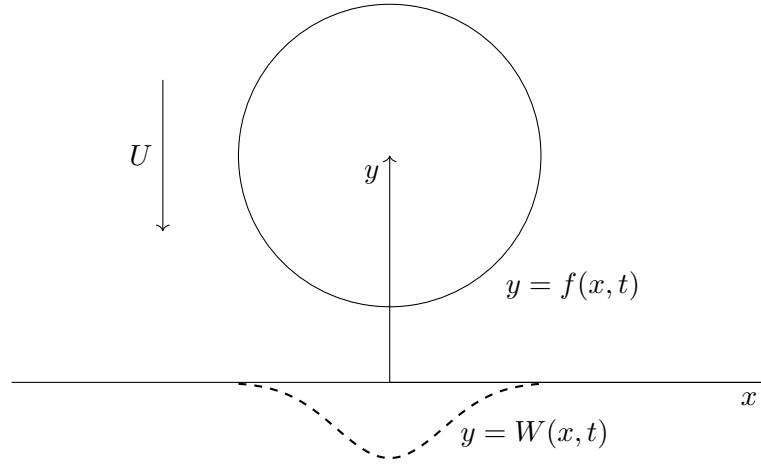


Figure 4.1.1: Schematic showing the problem being considered in this section.

The liquid droplet is assumed to be incompressible and irrotational. The liquid velocity field  $\mathbf{u}_1 = (u_1, v_1)$  is governed by the Navier-Stokes equations

$$\nabla \cdot \mathbf{u}_1 = 0, \quad (4.1.3)$$

$$\frac{D_1 \mathbf{u}_1}{Dt} = \left( \frac{\partial}{\partial t} + \mathbf{u}_1 \cdot \nabla \right) \mathbf{u}_1 = -\frac{1}{\rho_1} \nabla p_1 + \frac{\mu_1}{\rho_1} \nabla^2 \mathbf{u}_1. \quad (4.1.4)$$

Subscript 1 denotes a property of the liquid. In equation (4.1.4)  $\rho_1$  is the liquid density,  $\mu_1$  is the liquid dynamic viscosity and  $p_1$  is the liquid pressure, measured relative to an atmospheric pressure  $p_a$  such that  $p_l = p_a + p_1$  gives the total hydrodynamic pressure in the liquid droplet.

We denote gas properties by a subscript 2. The gas is assumed to be irrotational

and incompressible. The gases velocity field  $\mathbf{u}_2 = (u_2, v_2)$  is governed by

$$\nabla \cdot \mathbf{u}_2 = 0, \quad (4.1.5)$$

$$\frac{D_2 \mathbf{u}_2}{Dt} = \left( \frac{\partial}{\partial t} + \mathbf{u} \cdot \nabla \right) \mathbf{u}_2 = -\frac{1}{\rho_2} \nabla p_2 + \frac{\mu_2}{\rho_2} \nabla^2 \mathbf{u}_2. \quad (4.1.6)$$

As in the liquid we measure the gas pressure relative to the atmospheric pressure  $p_a$  so  $p_g = p_a + p_2$  provides the total pressure in the gas. The material parameters  $\rho_2$  and  $\mu_2$  are the density and dynamic viscosity of the gas respectively. On the free surface interface between the liquid and gas,  $y = f(x, t)$ , we have the kinematic and dynamic boundary conditions

$$\frac{D_1(y - f(x, t))}{Dt} = \frac{D_2(y - f(x, t))}{Dt} = 0, \quad (4.1.7)$$

$$\mathbf{n} \cdot (\mathbf{T}_1 - \mathbf{T}_2) \cdot \mathbf{n} = \sigma \nabla \cdot \mathbf{n}, \quad (4.1.8)$$

$$\mathbf{n} \cdot (\mathbf{T}_1 - \mathbf{T}_2) \cdot \mathbf{t} = 0. \quad (4.1.9)$$

We have introduced the constant surface tension  $\sigma$ , inward pointing unit normal and tangential vectors to the free surface  $\mathbf{n}$  and  $\mathbf{t}$  and liquid and gas stress tensors  $\mathbf{T}_1$  and  $\mathbf{T}_2$ . The stress tensors are given by

$$\mathbf{T}_1 = -p_1 \mathbf{I} + 2\mu_1 (\nabla \mathbf{u}_1 + (\nabla \mathbf{u}_1)^T) \quad (4.1.10)$$

On the interface between the gas and solid substrate,  $y = W(x, t)$ , we have the no slip and impermeability conditions

$$v_2 = \frac{\partial W}{\partial t}, \quad u_2 = 0. \quad (4.1.11)$$

As in the previous chapters we use thin plate theory to model the elastic part of the substrate. Modelling the plate as an Euler beam with clamped edges at  $x = x_0 \pm L/2$ . The governing equation for the plate shape is given by

$$\mu_p \frac{\partial^2 w}{\partial t^2} + EI \frac{\partial^4 w}{\partial x^4} = p_2(x, y = w(x, t), t), \quad (4.1.12)$$

$$\frac{\partial w}{\partial x} = w = 0, \quad x = x_0 \pm \frac{L}{2}. \quad (4.1.13)$$

In the plate equation (4.1.12)  $\mu_p$  is the mass per unit length of the plate and the product  $EI$  is the flexural rigidity.

We assume that at some time  $t = t_0 < 0$  the droplet free surface is undeformed and gas pressure is the same as atmospheric pressure and the plate is flat and stationary. These assumptions form our initial conditions

$$f(x, t_0) = \pm \sqrt{R^2 - x^2} - Ut_0 + r, \quad p_2(x, y, t_0) = 0, \quad (4.1.14)$$

$$w(x, t_0) = 0, \quad \frac{\partial w(x, t_0)}{\partial t} = 0. \quad (4.1.15)$$

We now non-dimensionalise the model. The droplet radius  $R$  is used as the characteristic length scale, impact speed  $U$  as velocity scale, the ratio  $R/U$  as time scale. Since the dynamic effects of the incoming droplet dominate the problem we use  $\rho_1 U^2$  as the pressure scale. The free surface and elastic plate shapes are non-dimensionalised using the same scale as the vertical coordinate,  $R$ . Denoting dimensionless variables with an over-bar,  $x = R\bar{x}$  for instance, we have the liquid governing equations

$$\bar{\nabla} \cdot \bar{\mathbf{u}}_1 = 0, \quad (4.1.16)$$

$$\frac{D_1 \bar{\mathbf{u}}_1}{D\bar{t}} = -\bar{\nabla} \bar{p}_2 + \frac{1}{Re} \bar{\nabla}^2 \bar{\mathbf{u}}_1. \quad (4.1.17)$$

We have introduced the liquid Reynolds number  $Re = \rho_1 UR/\mu_1$ . The free surface

boundary conditions become

$$\frac{D_1(\bar{y} - \bar{f}(\bar{x}, \bar{t}))}{D\bar{t}} = \frac{D_2(\bar{y} - \bar{f}(\bar{x}, \bar{t}))}{D\bar{t}} = 0, \quad (4.1.18)$$

$$\mathbf{n} \cdot \left( (\bar{p}_2 - \bar{p}_1) \mathbf{I} + \frac{2}{Re} (\bar{\nabla} \bar{\mathbf{u}}_1 - (\bar{\nabla} \bar{\mathbf{u}}_1)^\top) - \frac{2\mu_2}{\mu_1 Re} (\bar{\nabla} \bar{\mathbf{u}}_2 - (\bar{\nabla} \bar{\mathbf{u}}_2)^\top) \right) \cdot \mathbf{n} = \frac{1}{We} \bar{\nabla} \cdot \bar{\mathbf{n}}, \quad (4.1.19)$$

$$\mathbf{n} \cdot \left( (\bar{p}_2 - \bar{p}_1) \mathbf{I} + \frac{2}{Re} (\bar{\nabla} \bar{\mathbf{u}}_1 - (\bar{\nabla} \bar{\mathbf{u}}_1)^\top) - \frac{2\mu_2}{\mu_1 Re} (\bar{\nabla} \bar{\mathbf{u}}_2 - (\bar{\nabla} \bar{\mathbf{u}}_2)^\top) \right) \cdot \mathbf{t} = 0, \quad (4.1.20)$$

where  $We = R\rho_1 U^2 / \sigma$  is the Weber number. The gas governing equations take the form

$$\bar{\nabla} \cdot \bar{\mathbf{u}}_2 = 0, \quad (4.1.21)$$

$$\frac{\bar{\rho}_2}{\rho_1} \frac{D_2 \bar{\mathbf{u}}_2}{D\bar{t}} = -\bar{\nabla} \bar{p}_2 + \frac{\mu_2}{Re \mu_1} \bar{\nabla}^2 \bar{\mathbf{u}}_2. \quad (4.1.22)$$

The elastic plate governing equations take the form

$$\bar{W}(\bar{x}, \bar{t}) = \begin{cases} 0 & \bar{x} \leq \bar{x}_0 - \frac{\bar{L}}{2}, \\ \bar{w}(\bar{x}, \bar{t}) & \bar{x}_0 - \frac{\bar{L}}{2} < \bar{x} < \bar{x}_0 + \frac{\bar{L}}{2}, \\ 0 & \bar{x} \geq \bar{x}_0 + \frac{\bar{L}}{2}, \end{cases} \quad (4.1.23)$$

$$\alpha \frac{\partial^2 \bar{w}}{\partial \bar{t}^2} + \beta \frac{\partial^4 \bar{w}}{\partial \bar{x}^4} = \bar{p}_2(\bar{x}, \bar{y} = \bar{w}, \bar{t}), \quad (4.1.24)$$

$$\frac{\partial \bar{w}}{\partial \bar{x}} = \bar{w} = 0, \quad \bar{x} = \bar{x}_0 \pm \frac{\bar{L}}{2}, \quad (4.1.25)$$

where

$$\alpha = \frac{\rho_p h}{\rho_1 R}, \quad \beta = \frac{EI}{\rho_1 R^3 U^3}. \quad (4.1.26)$$

As in the previous chapters, the parameter  $\alpha$  governs the important of the structural mass of the plate to the added mass of the liquid and depends on the plate thickness  $h$  and plate density  $\rho_p$ . The parameter  $\beta$  can be thought of as

the dynamic rigidity of the plate. The initial conditions applied at some time  $\bar{t} = \bar{t}_0 < 0$  are given in non-dimensional form by

$$\bar{f}(\bar{x}, \bar{t}_0) = \pm\sqrt{1 - \bar{x}^2} - \bar{t}_0 + 1, \quad \bar{p}_2(\bar{x}, \bar{y}, \bar{t}_0) = 0, \quad (4.1.27)$$

$$\bar{w}(\bar{x}, \bar{t}_0) = 0, \quad \frac{\partial \bar{w}(\bar{x}, \bar{t}_0)}{\partial \bar{t}} = 0. \quad (4.1.28)$$

The gas-substrate boundary conditions retain their form

$$\bar{v}_2 = \frac{\partial \bar{W}}{\partial \bar{t}}, \quad \bar{u}_2 = 0, \quad \bar{y} = \bar{W}. \quad (4.1.29)$$

In addition to the droplet radius  $R$  there is another, shorter, length scale  $H$ . The scale of  $H$  corresponds to the thickness of the air gap when pressure in the air film makes a leading order contribution to the free surface and elastic plate deformation. We assume that  $H \ll R$  and introduce a small parameter  $\delta$

$$\delta = \frac{H}{R}. \quad (4.1.30)$$

Since the gas has a much lower density than the liquid it only has an appreciable effect on the liquids movement when the gap between solid substrate and liquid droplet is very small. We investigate the air cushioning dynamics during a short time before impact, motivating a rescaling of time  $\bar{t} = \delta^2 t$ . We reuse symbols from the dimensional terms, with the understanding that from here on in all variables are dimensionless and scaled. As in the Wagner model of liquid impacts we are interested in a small square window close to the touchdown region, motivating a rescaling of coordinates to  $(\bar{x}, \bar{y}) = \delta(x, y)$ . However even on this small vertical scale the pressure in the gas is not high enough to deform the liquid free surface. As such in the gas we have a separation of vertical and horizontal scales, providing  $(\bar{x}, \bar{y}) = \delta(x, \delta y)$ . In order to maintain conservation of mass the length scales force the gas velocity scales  $(\bar{u}_2, \bar{v}_2) = (\delta^{-1} u_2, v_2)$ . To allow for deformations in the free surface and substrate deformation the substrate is scaled to match the vertical

scale,  $\bar{f} = \delta^2 f$ . Pressure is scaled,  $\bar{p}_2 = \delta^{-1} p_2$ , is motivated from matching the liquid pressure scale discussed below. We substitute

$$(\bar{x}, \bar{y}, \bar{t}, \bar{u}_2, \bar{v}_2, \bar{f}, \bar{p}_2) = (\delta x, \delta^2 y, \delta^2 t, \delta^{-1} u_2, v_2, \delta^2 f, \delta^{-1} p_2) \quad (4.1.31)$$

into the horizontal component of the gas momentum balance equation (4.1.22)

$$\delta^2 \frac{\rho_2}{\rho_1} \frac{D_2 u_2}{Dt} = -\delta^3 \frac{\partial p_2}{\partial x} + \frac{\mu_2}{Re \mu_1} \left( \delta^2 \frac{\partial^2 u_2}{\partial x^2} + \frac{\partial^2 u_2}{\partial y^2} \right). \quad (4.1.32)$$

When considering a typical gas-liquid pairing, air and water for instance, we find that the ratios  $\rho_2/\rho_1$  and  $\mu_2/\mu_1$  are both small, with the density ratio smaller than the viscosity ratio. From this we can see that for some range of  $Re$  the  $\partial^2 u/\partial^2 y$  term is the largest in equation (4.1.32). In order to satisfy boundary conditions this must be balanced by another term. The pressure gradient term is the next largest, motivating a balance between the pressure gradient and  $\partial^2 u/\partial y^2$  which requires  $\delta$  to take the form

$$\delta = \left( \frac{\mu_2}{Re \mu_1} \right)^{\frac{1}{3}}. \quad (4.1.33)$$

Note that depending on the parameters the inertial term could be larger than the viscous term which would have a different form of the small parameter  $\delta$ . This inviscid air cushioning is what [Wilson \[1991\]](#) studied.

Using the definition of  $\delta$  above and by comparing the viscous to inertial terms in equation (4.1.32) we find that

$$Re < \left( \frac{\nu_2}{\nu_1} \right)^3 \left( \frac{\mu_1}{\mu_2} \right)^2, \quad (4.1.34)$$

for our value of  $\delta$  to be correct. Substituting the values for, say, air and water into equation (4.1.34) we find  $Re < 10^7$ . Similarly by requiring that  $\delta < 1$  and again using the dynamic viscosities of water and air we find  $Re > 0.02$ , providing a wide range of applicability for our model. The leading order vertical and horizontal components of the gas momentum equation (4.1.32) become the

lubrication equations

$$\frac{\partial p_2}{\partial y} = 0, \quad \frac{\partial^2 u_2}{\partial y^2} = \frac{\partial p_2}{\partial x}, \quad (4.1.35)$$

with the gas continuity equation reading

$$\frac{\partial u_2}{\partial x} + \frac{\partial v_2}{\partial y} = 0. \quad (4.1.36)$$

Substituting the scales (4.1.31) into the kinematic boundary condition (4.1.7) provides

$$u_2 = 0, \quad v_2 = \frac{\partial f}{\partial t}, \quad y = f(x, t). \quad (4.1.37)$$

When considering scales for the liquid phase we are interested the same small time just before impact, providing the time scale  $\bar{t} = \delta^2 t$ . The horizontal scale must match that used in the gas  $\bar{x} = \delta x$ . The vertical scale is one order of magnitude bigger,  $\bar{y} = \delta y$ . In the gas the vertical scale is of order  $O(\delta^2)$  to allow for the gas, with its comparatively low density, to act against the liquid. This is not required in the liquid giving us a difference in vertical scales between the gas and liquid. We match the vertical scale in the liquid with that of the gas so that  $\bar{v}_1 = v_1$ . Conservation of mass (4.1.17) then requires we set the horizontal velocity scale to  $\bar{u}_1 = u_1$ . By examining the horizontal and vertical components of the momentum conservation equation (4.1.16) and giving pressure and unknown scale  $\bar{p}_1 = \delta^a p_1$  we find

$$\delta^{-2} \frac{\partial \bar{u}_1}{\partial \bar{t}} + \delta^{-1} \bar{u}_1 \frac{\partial \bar{u}_1}{\partial \bar{x}} + \delta^{-1} \bar{v}_1 \frac{\partial \bar{u}_1}{\partial \bar{y}} = -\delta^{a-1} \frac{\partial \bar{p}_1}{\partial \bar{x}} + \delta^{-2} Re^{-1} \left( \frac{\partial^2 \bar{u}_1}{\partial \bar{x}^2} + \frac{\partial^2 \bar{u}_1}{\partial \bar{y}^2} \right), \quad (4.1.38)$$

$$\delta^{-2} \frac{\partial \bar{v}_1}{\partial \bar{t}} + \delta^{-1} \bar{u}_1 \frac{\partial \bar{v}_1}{\partial \bar{x}} + \delta^{-1} \bar{v}_1 \frac{\partial \bar{v}_1}{\partial \bar{y}} = -\delta^{a-1} \frac{\partial \bar{p}_1}{\partial \bar{y}} + \delta^{-2} Re^{-1} \left( \frac{\partial^2 \bar{v}_1}{\partial \bar{x}^2} + \frac{\partial^2 \bar{v}_1}{\partial \bar{y}^2} \right). \quad (4.1.39)$$

By matching the pressure terms to the time derivatives we find  $a = -1$  so that the pressure scale  $\bar{p}_1 = \delta^{-1} p_1$  which also informed the previously used gas pressure

scale. We now substitute all scales

$$(\bar{x}, \bar{y}, \bar{u}_1, \bar{v}_1, \bar{f}, \bar{p}_1) = (\delta x, \delta y, u_1, v_1, \delta^2 f, \delta^{-1} p) \quad (4.1.40)$$

into the liquid governing equations (4.1.16) and (4.1.17) and retain only leading order terms to obtain the linearised Euler equations

$$\frac{\partial u_1}{\partial x} + \frac{\partial v_1}{\partial y} = 0, \quad \frac{\partial u_1}{\partial t} = -\frac{\partial p_1}{\partial x}, \quad \frac{\partial v_1}{\partial t} = -\frac{\partial p_1}{\partial y}. \quad (4.1.41)$$

The normal stress boundary condition, with compressibility neglected in the gas, takes the form

$$p_1 - p_2 = \delta W e^{-1} \nabla \cdot \mathbf{n}. \quad (4.1.42)$$

We can neglect the effects of surface tension provided  $\delta W e^{-1} \ll O(1)$  or smaller. Using water as our liquid the inverse Weber number  $W e^{-1} = \sigma / (R \rho_1 U^2) = 7.28 \times 10^{-5} \text{m}^3 \text{s}^{-2} / (R U^2)$ . Considering droplets in the millimetre to centimetre range we require  $U > 0.26 \text{ms}^{-1}$  and  $U > 0.085 \text{ms}^{-1}$ . Considering our Reynolds number has the limit  $Re < 10^7$  we can comfortably neglect the effects of surface tension. Under this assumption the dynamic boundary condition takes the form

$$p_1 = p_2, \quad y = f(x, t). \quad (4.1.43)$$

The plate is governed by the same short time scale as the other phases,  $\bar{t} = \delta^2 t$ . In order to retain a coupled problem the plate deformation has the same scale as free surface deformations  $\bar{w} = \delta^2 w$ . The small square region close to the contact point motivates coordinate scalings of  $(\bar{x}, \bar{y}) = \delta(x, y)$  for the elastic plate. The pressure scale matches that used in the gas problem  $\bar{p}_2 = \delta^{-1} p_2$ . If we use a different scale for the plate deformation  $\bar{w}$  or pressure the plate problem will decouple from the gas-liquid problem, removing its dynamics from any leading order behaviour further on in this chapter. Substituting the scales

$$(\bar{x}, \bar{y}, \bar{t}, \bar{w}, \bar{p}_2) = (\delta x, \delta y, \delta^2 t, \delta^2 w, \delta^{-1} p_2), \quad (4.1.44)$$

into the plate governing equation (4.1.24) and boundary conditions (4.1.25)

$$\hat{\alpha} \frac{\partial^2 w}{\partial t^2} + \hat{\beta} \frac{\partial^4 w}{\partial x^4} = p_2, \quad (4.1.45)$$

$$\frac{\partial w}{\partial x} = w = 0, \quad x = x_0 \pm \frac{L}{2}, \quad (4.1.46)$$

$$\frac{\partial w}{\partial t} = v_2, \quad x = x_0 \pm \frac{L}{2}, y = f(x, t), \quad (4.1.47)$$

where we defined two new parameters

$$\hat{\alpha} = \frac{\alpha}{\delta} = \frac{\rho_p h U^{\frac{1}{3}}}{(\rho_1 R)^{\frac{2}{3}} \mu_2^{\frac{1}{3}}}, \quad \hat{\beta} = \frac{\beta}{\delta} = \frac{EI}{\rho_1^{\frac{2}{3}} R^{\frac{8}{3}} U^{\frac{8}{3}} \mu_2^{\frac{1}{3}}}. \quad (4.1.48)$$

We assume that  $\hat{\alpha}$  and  $\hat{\beta}$  are both of order  $O(1)$ . For example if we consider a water droplet of radius 1 cm impacting an aluminium plate of thickness 0.05 mm at a speed of 4 m/s we get  $\hat{\alpha} = 1/7$  and  $\hat{\beta} = 1.66$  with a Weber number  $We = 4.5 \times 10^{-4} \ll 1$  and Reynolds number of  $Re = 2 \times 10^{-4} \ll 10^{-7}$ .

### 4.1.2 Problem Solution

The pre-impact gas cushioning problem derived in the previous sections is non-linear, coupled to both liquid and elastic phases and very difficult to solve. The introduction of scaling arguments, based on considering a short time pre-impact, has simplified equations to be solved. Nevertheless, the problem remains coupled to both liquid and elastic phase and non-linear. We turn the system above into a pair of coupled integral equations together with the plate equation to be solved with numerical methods described later.

To begin with use the equations (4.1.35) to find  $u_2$ ,

$$u_2(x, y, t) = \frac{1}{2} \frac{\partial p_2(x, t)}{\partial x} y^2 + A(x, t)y + B(x, t), \quad (4.1.49)$$

where  $A$  and  $B$  are unknown functions, introduced by integration. In order to

set these functions we make use of the boundary conditions on the free surface and solid substrate, equations (4.1.37) and (4.1.29) respectively. We arrive at a system of two equations,

$$\frac{1}{2} \frac{\partial p_2}{\partial x} f^2 + Af + B = 0, \quad (4.1.50)$$

$$\frac{1}{2} \frac{\partial w}{\partial x} w^2 + Aw + B = 0. \quad (4.1.51)$$

The simultaneous equations (4.1.50)-(4.1.51) are solved for  $A$  and  $B$  providing

$$A = -\frac{1}{2} \frac{\partial p_2}{\partial x} (f + w), \quad B = \frac{1}{2} \frac{\partial p_2}{\partial x} fw. \quad (4.1.52)$$

Now we take the gas continuity equation (4.1.36) and integrate across the gas from  $y = w(x, t)$  to  $y = f(x, t)$ ,

$$\int_{w(x,t)}^{f(x,t)} \frac{\partial u_2}{\partial x} dy + v \Big|_{w(x,t)}^{f(x,t)} = 0. \quad (4.1.53)$$

Substituting our expression for  $u_2$ , equation (4.1.49) with (4.1.50)-(4.1.51), and using boundary conditions (4.1.37) and (4.1.47) we find

$$\frac{1}{2} \frac{\partial}{\partial x} \left( \frac{\partial p_2}{\partial x} \left( \int_w^f y^2 - (f+w)y + fw \right) \right) + \frac{\partial}{\partial t} (f - w) = 0. \quad (4.1.54)$$

Integrating equation (4.1.54) provides us with the first governing equation,

$$\frac{1}{12} \frac{\partial}{\partial x} \left( \frac{\partial p_2}{\partial x} (f - w)^2 \right) = \frac{\partial}{\partial t} (f - w). \quad (4.1.55)$$

We take the liquid governing equations (4.1.41) and differentiate the horizontal and vertical momentum equations with respect to  $x$  and  $y$  respectively,

$$\frac{\partial}{\partial y} \left( \frac{\partial v_1}{\partial t} \right) = \frac{\partial}{\partial x} \left( \frac{\partial p_1}{\partial x} \right), \quad \frac{\partial}{\partial x} \left( \frac{\partial v_1}{\partial t} \right) = -\frac{\partial}{\partial y} \left( \frac{\partial p_1}{\partial x} \right), \quad (4.1.56)$$

which are the Cauchy-Riemann equations for  $v_1$  and  $p_1$ . By definition equations (4.1.56) give us an analytic function  $K(z, t) = \frac{\partial v_1}{\partial t} + i \frac{\partial p_1}{\partial x}$  in the fluid  $y \geq f(x, t)$ .

Using the Hilbert formula provides

$$\Re [K(x + if, t)] = \frac{1}{\pi} P.V. \int_{-\infty}^{\infty} \Im [K(\xi + if, t)] \frac{d\xi}{x - \xi}, \quad (4.1.57)$$

where *P.V.* indicates a principal value integral. Substituting *K* into equation (4.1.57) results in

$$\frac{\partial v_1(x, f, t)}{\partial t} = \frac{1}{\pi} P.V. \int_{-\infty}^{\infty} \frac{\partial p_1(\xi, f, t)}{\partial \xi} \frac{d\xi}{x - \xi}. \quad (4.1.58)$$

The dynamic and kinematic boundary conditions on  $y = f(x, t)$  then give us the second governing equation

$$\frac{\partial^2 f}{\partial t^2} = \frac{1}{\pi} P.V. \int_{-\infty}^{\infty} \frac{\partial p_2(\xi, t)}{\partial \xi} \frac{d\xi}{x - \xi}. \quad (4.1.59)$$

## 4.2 Numerical Methods

The full system of governing equations,

$$\frac{\partial}{\partial x} \left( \frac{\partial p_2}{\partial x} (f - w)^3 \right) = 12 \frac{\partial}{\partial t} (f - w), \quad (4.2.1)$$

$$\frac{\partial^2 f}{\partial t^2} = \frac{1}{\pi} P.V. \int_{-\infty}^{\infty} \frac{\partial p_2(\xi, t)}{\partial \xi} \frac{d\xi}{x - \xi}, \quad (4.2.2)$$

$$\hat{\alpha} \frac{\partial^2 w}{\partial t^2} + \hat{\beta} \frac{\partial^4 w}{\partial x^4} = p_2, \quad x_0 - \frac{L}{2} \leq x \leq x_0 + \frac{L}{2}, \quad (4.2.3)$$

together with boundary conditions

$$\frac{\partial w}{\partial x} = 0, \quad w = 0, \quad x = x_0 \pm \frac{L}{2}, \quad (4.2.4)$$

$$p_2 = 0, \quad f = \frac{x^2}{2} - t, \quad x^2 \rightarrow \infty, \quad (4.2.5)$$

and initial conditions

$$p_2 = 0, \quad f = \frac{x^2}{2} - t, \quad w = 0, \quad t \rightarrow -\infty, \quad (4.2.6)$$

form coupled system of linear partial differential equations to be solved with one spatial dimension and time. We use finite differences to solve the liquid and gas problems (5.3.10b)-(4.2.2) and the method of normal modes to solve the plate equation (4.1.45).

For the finite difference solutions we use uniform grids in  $x$  and  $t$  with node spacings of  $\delta x$ ,  $\delta t$  respectively. We introduce the notation

$$f(x, t) = F_j^i, \quad p_2(x, t) = P_j^i, \quad w(x, t) = W_j^i, \quad (4.2.7)$$

where the subscript  $j$  and superscript  $i$  refer to the value of the function at the time node  $t_j$  and position node  $x_i$  respectively. Implementing the trapezium rule using first order centred differences we find that the free surface equation (4.2.2) gives

$$\frac{F_{j-1}^i - 2F_j^i + F_{j+1}^i}{(\delta t)^2} = \sum_{\substack{k=0 \\ k \neq i}}^N \frac{P_j^{k+1} - P_j^{k-1}}{(x_i - x_k)} m_k, \quad (4.2.8)$$

where  $m_k$  is the weight function such that  $m_k = 2\delta x$  at the end points  $k = 0, k = N$  and  $m_k = \delta x$  otherwise. The  $k \neq i$  is required for the principal value integration in order to avoid the singularity when  $x_i = x_k$ . In the far field we assume that the gas pressure and liquid free surface are undisturbed from their starting values,  $P_j^i = 0$  and  $F_j^i = (x^i)^2 / 2 - t_j^i$  for  $i \notin [0, N]$ .

Equation (4.2.8) is rearranged to give the next time steps value of the free surface in terms of known quantities

$$F_{j+1}^i = 2F_j^i - F_{j-1}^i + (\delta t)^2 \sum_{\substack{k=0 \\ k \neq i}}^N \frac{P_j^{k+1} - P_j^{k-1}}{(x_i - x_k)} m_k. \quad (4.2.9)$$

In the pressure integro-differential equation (5.3.10b) we expand the left hand side,

$$\frac{\partial^2 p_2}{\partial x^2} (f - w)^3 + 3(f - w)^2 \frac{\partial p_2}{\partial x} \frac{\partial (f - w)}{\partial x}, \quad (4.2.10)$$

which we then use finite differences to find

$$\begin{aligned}
& P_j^{i-1} \left( 4 (F_j^i - W_j^i)^3 - 3 (F_j^i - W_j^i)^2 \left( (F_j^{i+1} - W_j^{i+1}) - (F_j^{i-1} - W_j^{i-1}) \right) \right) \\
& + P_j^{i+1} \left( 4 (F_j^i - W_j^i)^3 + 3 (F_j^i - W_j^i)^2 \left( (F_j^{i+1} - W_j^{i+1}) - (F_j^{i-1} - W_j^{i-1}) \right) \right) \\
& - 8 P_j^i (F_j^i - W_j^i)^3 = \frac{24\delta x^2}{\delta t} \left( (F_{j+1}^i - W_{j+1}^i) - (F_{j-1}^i - W_{j-1}^i) \right). \quad (4.2.11)
\end{aligned}$$

The pressure equation (4.2.11) can be written as a tridiagonal matrix of the form

$$\begin{pmatrix} b_0 & c_1 & & 0 \\ a_1 & b_1 & \ddots & \\ & \ddots & \ddots & c_N \\ 0 & & a_N & b_N \end{pmatrix} \begin{pmatrix} P_j^0 \\ P_j^1 \\ \vdots \\ P_j^N \end{pmatrix} = \begin{pmatrix} d_0 \\ d_1 \\ \vdots \\ d_N \end{pmatrix}, \quad (4.2.12)$$

where

$$a_i = \left( 4 (F_j^i - W_j^i)^3 - 3 (F_j^i - W_j^i)^2 \left( (F_j^{i+1} - W_j^{i+1}) - (F_j^{i-1} - W_j^{i-1}) \right) \right), \quad (4.2.13)$$

$$b_i = -8 (F_j^i - W_j^i)^3 \quad (4.2.14)$$

$$c_i = P_j^{i+1} \left( 4 (F_j^i - W_j^i)^3 + 3 (F_j^i - W_j^i)^2 \left( (F_j^{i+1} - W_j^{i+1}) - (F_j^{i-1} - W_j^{i-1}) \right) \right) \quad (4.2.15)$$

$$d_i = \frac{24\delta x^2}{\delta t} \left( (F_{j+1}^i - W_{j+1}^i) - (F_{j-1}^i - W_{j-1}^i) \right). \quad (4.2.16)$$

The matrix problem (4.2.12) is solved for  $P_j^i$  using standard linear algebra numerical methods.

For the plate problem (4.1.45) we use the method of normal modes to find the plate displacement. This method expresses the plate displacement in terms of eigenfunctions of its free vibrations, such that  $w = w(x) \sin(\omega t)$ . To find the normal modes of the plate equation we let  $p = 0$  in the plate equation (4.1.45) and substitute the expansion above to obtain

$$\frac{d^4 w}{dx^4} = \frac{\alpha \omega^2}{\beta} w. \quad (4.2.17)$$

The eigenvector problem (4.2.17) has the general solution

$$w(x) = A \cos(kx) + B \sin(kx) + C \cosh(kx) + D \sinh(kx), \quad (4.2.18)$$

where  $k^4 = \alpha\omega^2/\beta$ . If the problem has an elastic plate with its centre at  $x_0 = 0$ , then the boundary conditions can be written as

$$\frac{dw}{dx} = 0, \quad w = 0, \quad x = \pm \frac{L}{2}, \quad (4.2.19)$$

which we can use to set  $B = D = 0$  and retain only the boundary conditions at  $L/2$  to set  $A$  and  $C$ . The remaining problem can be written in matrix form

$$\begin{pmatrix} \cos\left(\frac{kL}{2}\right) & \cosh\left(\frac{kL}{2}\right) \\ -\sin\left(\frac{kL}{2}\right) & \sinh\left(\frac{kL}{2}\right) \end{pmatrix} \begin{pmatrix} A \\ D \end{pmatrix} = \begin{pmatrix} 0 \\ 0 \end{pmatrix}. \quad (4.2.20)$$

There is a non-trivial solution if the  $2 \times 2$  determinant is zero, which provides us with a set of  $k_j$   $j \geq 1$  which are the frequencies for the normal modes,  $w_j(x)$ . Taking the determinant we find that  $k_j$  are the positive non-trivial real roots of

$$f(k_j) = \cos\left(\frac{k_j L}{2}\right) \sinh\left(\frac{k_j L}{2}\right) + \sin\left(\frac{k_j L}{2}\right) \cosh\left(\frac{k_j L}{2}\right). \quad (4.2.21)$$

We then use the first line of (4.2.20) to obtain a relationship between  $A$  and  $D$  which allows us to write the modes, up to an arbitrary scalar coefficient, as

$$w_j(x) = \cos(k_j x) - \frac{\cos\left(\frac{k_j L}{2}\right)}{\cosh\left(\frac{k_j L}{2}\right)} \cosh(k_j x), \quad (4.2.22)$$

for the plate with its centre at  $x_0 = 0$ . If the centre of the elastic plate is not at the origin,  $x_0 \neq 0$ , then we have to solve (4.2.18) subject to

$$\frac{dw}{dx} = 0, \quad w = 0, \quad x = a, b, \quad (4.2.23)$$

where we have introduced  $a = x_0 - L/2$  and  $b = x_0 + L/2$ . We can let  $x \rightarrow x - a$

to translate the problem to

$$\frac{dw}{dx} = 0, \quad w = 0, \quad x = (0, L). \quad (4.2.24)$$

Solution for the eigenvalue problem (4.2.17) subject to conditions (4.2.24) was given by Leissa [1969]. Using his solution we can write the normal modes, in the off-centred plate case, as

$$w_j = \begin{cases} \cos \left( l_j \left( \frac{x-a}{L} - \frac{1}{2} \right) \right) + \frac{\sin \left( \frac{l_j}{2} \right)}{\sinh \left( \frac{l_j}{2} \right)} \cosh \left( l_j \left( \frac{x-a}{L} - \frac{1}{2} \right) \right), & i = 2, 4, 6, \dots, \\ \sin \left( k_j \left( \frac{x-a}{L} - \frac{1}{2} \right) \right) + \frac{\sin \left( \frac{k_j}{2} \right)}{\sinh \left( \frac{k_j}{2} \right)} \sinh \left( k_j \left( \frac{x-a}{L} - \frac{1}{2} \right) \right), & j = 1, 3, 5, \dots \end{cases} \quad (4.2.25)$$

where  $\{l_j\}$  and  $\{k_j\}$  are the sets of non-trivial positive real roots of

$$\tan \left( \frac{l_j}{2} \right) + \tanh \left( \frac{l_j}{2} \right) = 0, \quad (4.2.26)$$

$$\tan \left( \frac{k_j}{2} \right) - \tanh \left( \frac{k_j}{2} \right) = 0, \quad (4.2.27)$$

respectively. Since the modes (4.2.22) and (4.2.25) form a complete orthogonal set we express the plate displacement in terms of them,

$$w(x, t) = \sum_{j=1}^{\infty} A_j(t) w_j(x), \quad (4.2.28)$$

so that the plate equation takes the form

$$\sum_{j=1}^{\infty} \left( \alpha \ddot{A}_j(t) + \beta k_j^4 A_j(t) \right) w_j(x) = p_2(x, t). \quad (4.2.29)$$

Taking the projection of  $w_i(x)$  against (4.2.29) and using the mode orthogonality,

$$U_{i,j} \delta_{i,j} = \int_{-\frac{L}{2}+x_0}^{\frac{L}{2}+x_0} w_i(x) w_j(x) dx, \quad (4.2.30)$$

we move all spatial dependence to just the pressure term,

$$\sum_{i=1}^{\infty} U_{ii} \left( \alpha \ddot{A}_i(t) + \beta k_i^2 \right) = \int_{-\frac{L}{2}+x_0}^{\frac{L}{2}+x_0} w_i(x) p_2(x, t) dx. \quad (4.2.31)$$

The integral in the right-hand side of (4.2.31) is calculated using the discrete form of  $p_2(x, t)$  as

$$\int_{-\frac{L}{2}+x_0}^{\frac{L}{2}+x_0} w_i(x) p_2(x, t) dx = \sum_{k=a}^{k=b} P_j^k w_i(x_k) m_k, \quad (4.2.32)$$

where  $m_k$  is the discrete weight function defined earlier and  $x_a$  and  $x_b$  give the end points of the elastic plate. We can then solve the plate equation (4.2.29) for the future value of  $A(t)$  using finite differences to arrive at

$$A_{j,k+1} = 2A_{j,k} - A_{j,k-1} - \frac{(\delta t)^2}{\alpha} \left( \beta g_j^4 A_{j,k} + \sum_{k=a}^{k=b} P_j^k w_i(x_k) m_k \right), \quad (4.2.33)$$

$$g_j = \begin{cases} k_j, & x_0 = 0, \\ \frac{l_j}{L}, & x_0 \neq 0, j = 2, 4, 6... \\ \frac{k_j}{L}, & x_0 \neq 0, j = 1, 3, 5... \end{cases} \quad (4.2.34)$$

The plate deformation can then be put into discrete form via

$$W_j^i = \begin{cases} \sum_{l=0}^{\infty} \sum_{k=a}^b A_{l,j} w_l(x_k) \\ 0 \end{cases} \quad \text{for all } x_k \quad k \neq [a, b], \quad (4.2.35)$$

with  $W_j^i$  being used in the pressure equation (4.2.12).

We now have the three equations to be solved, (4.2.9), (4.2.12) and (4.2.33). At each time step we use the known current and past values of  $F$ ,  $P$  and  $W$  to calculate an approximate for the next value of the free surface  $F_{j+1}^i$  via (4.2.9). The approximate value of  $F$  and previous values of  $P$  and  $W$  then give the pressure from (4.2.12) which is then used to calculate a plate shape (4.2.33). The approximate values of  $F$ ,  $P$  and  $W$  are then iterated until the change in pressure between successive iterations is acceptably small. In testing requiring the maximum difference between pressure at two iterations,  $P_{err}$ , to be less than  $10^{-7}$  is sufficient. The values of  $F$ ,  $P$  and  $W$  are then updated and the process restarted.

As the gap between the substrate and free surface become small the number of iterations required for convergence increases. We set a cap on how many iterations is allowed to occur prior to stopping the algorithm. This cap is typically set at 100 iterations, with a convergent set of  $F, P$  and  $W$  being found in less than 5 iterations for the majority of the simulation time. When we are interested in dynamics close to touch down we reduce the time step and increase the iteration cap.

We start our simulations from a time  $t = t_0 < 0$ , this time is such that the droplet is far enough from the substrate so that gas pressure is zero, the droplet free surface is a parabola and the elastic plate flat and stationary. A typical value of this starting time is  $t_0 = -10$ . We chose the width of the simulation in  $x$  to be such that the free surface at the edges matches the far field condition throughout the simulation. When choosing the range of our simulation we have found requiring the edge of the zone is at least 10 away from the furthest edge of the elastic plate is sufficient. In testing, we have found that  $M = 10$  plate modes are sufficient for accurate and convergent modelling of the plate behaviour, although this does depend on the plate parameters and typically  $M = 20$  is used. In testing choices of  $\delta x$  we have found that for most elastic plate parameters  $\delta x = 0.01$  provides accurate simulation. If the elastic plate is small or has a very high frequency then a smaller  $\delta x$  may be required in order to accurately perform the integral (4.2.32).

As mentioned previously, as the gas between free surface and solid substrate becomes very thin the number of iterations to find a convergent set of  $F, P$  and  $W$  grows rapidly. As the gap between free surface and substrate,  $F - W$  becomes small the pressure  $P$  becomes locally extremely large. This is seen in all lubrication style problems. From reality we know that the free surface does touch down, or impact, the substrate. Local asymptotics are used in a later section to show that a touch down does occur in finite time for our problem.

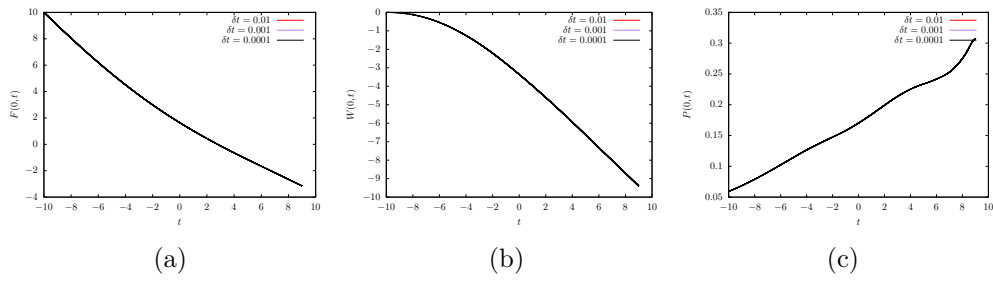


Figure 4.2.1: Time evolution of the free surface height (a), elastic plate deflection (b) and pressure (c) at the origin for plate parameters  $\alpha = 1.0, \beta = 1.0, x_0 = 0, L = 10$ . In each Figure there are 3 plots, calculated with differing time steps and a spatial step of  $\delta x = 0.01$ .

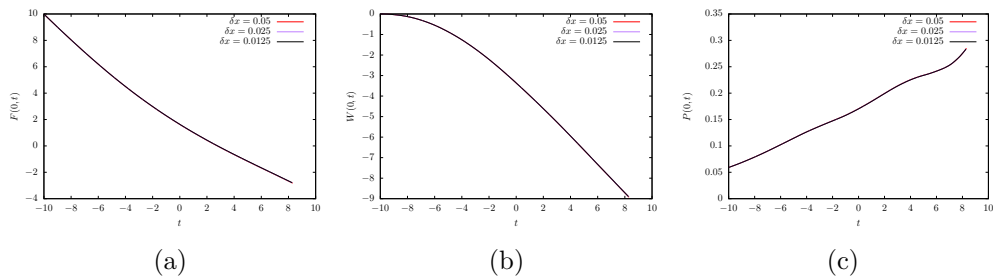


Figure 4.2.2: Time evolution of the free surface height (a), elastic plate deflection (b) and pressure (c) at the origin for plate parameters  $\alpha = 1.0, \beta = 1.0, x_0 = 0, L = 10$ . In each Figure there are 3 plots, calculated with different spatial step and a time step of  $\delta t = 0.01$ .

#### 4.2.1 Numerical Validation

The numerical scheme described in section 4.2 contains many parameters which must be chosen correctly to obtain accurate and reliable results. We have the spatial and temporal step sizes  $\delta x$  and  $\delta t$ , the number of modes used in solving the elastic plate problem  $M$ , the initial time  $t_0$  and the maximum error allowed in the pressure per iteration  $P_{err}$ . Within a given time step we take an estimated free surface shape  $F$  which is used to estimate  $P$  which is used to estimate  $W$  which is then used to estimate a new  $F$ . This iteration continues until the maximum difference between two subsequent pressure estimations is less than  $P_{err}$ . In Figure 4.2.1 we plot the free surface height, elastic plate deflection and pressure at the origin against time for different time steps. The Figures show very good convergence with the time step. The time we halt simulation at is different for the three time steps shown in Figure 4.2.1. For the plate parameters used in Figure

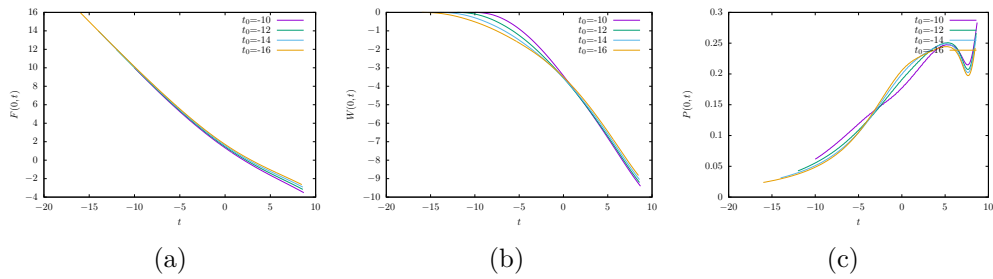


Figure 4.2.3: Time evolution of the free surface height (a), elastic plate deflection (b) and pressure (c) at the origin for plate parameters with different starting times  $t = t_0$ .

4.2.1 the  $\delta t = 0.01$  simulation ran until time  $t = 8.28$ , the  $\delta t = 0.0001$  ran until time  $t = 9.007$ . This is not an issue with convergence, we could continue any of the simulations further by allowing more iterations at each time step. In Figure 4.2.2 we also see very good convergence with respect to node spacing  $\delta x$ . As we will see in the results, for example in Figure 4.3.1, touchdown often occurs at a sharp corner like structure. Decreasing  $\delta x$  allows this structure to be examined more closely but the resolution required to round this point off requires a long computational time. Instead we investigate this touchdown region asymptotically in the next section.

Finally we look at the effect the initial time,  $t = t_0$ , has on our numerics. When choosing  $t_0$  we must ensure that any influence due to the droplet moving through  $-\infty < t < t_0$  is small. In Figure 4.2.3 we can see the free surface height, elastic plate deflection and pressure at the origin against time for 4 values of starting time ranging from  $t_0 = -10$  to  $t_0 = -16$ . As we can see, while there is some quantitative difference in the plots qualitatively the behaviour shown is consistent between the different initial times. In addition the difference between successive choices of  $t_0$  reduces meaning that, while we could keep reducing  $t_0$  to very large numbers the accuracy will not increase significantly for the increase in computational time and a choice of  $t_0 = -10$  is adequate for most situations.

### 4.2.2 Touchdown

In the numerical solution to the air cushioning problem (5.3.10b)-(4.2.3), discussed in section 4.2, we approach, but do not encounter, touchdown. Smith et al. [2003] investigated the local asymptotics for the touchdown region, the analysis in this section follows his ideas, with the added complication of the presence of the elastic plate. The numerical solution does indicate touchdown occurring at some finite time and position,  $T_0$  and  $X_0$  respectively. As an estimate we can use the final time and location of the thinnest gas film from the numerics. We investigate the region local to the touchdown point by using matched asymptotics. We assume there is a similarity variable  $\eta$  of the form

$$X - X_0 = (T_0 - T)^a \eta, \quad (4.2.36)$$

and that the free surface, pressure and plate shape all scale as

$$f \approx (T_0 - T)^b \tilde{F}(\eta) + A_0, \quad p_2 \approx (T_0 - T)^c \tilde{P}(\eta), \quad w \approx (T_0 - T)^d \tilde{W}(\eta) + A_0, \quad (4.2.37)$$

where  $\tilde{F} > 0$  and  $\tilde{W} > 0$  and  $A_0$  is some constant determined by matching to the outer solution. We substitute the local coordinates and functions (4.2.36) and (4.2.37) into the cushioning problem (5.3.10b)-(4.2.3) to arrive at the local problem

$$(T_0 - T)^{b-2} \left( b(b-1)\tilde{F} + a\eta(2b-1)\tilde{F}' + a^2\eta^2\tilde{F}'' \right) = \frac{(T_0 - T)^{c-a}}{\pi} \text{PV} \int_{-\infty}^{\infty} \frac{\tilde{P}'(\hat{\eta})d\hat{\eta}}{\eta - \hat{\eta}}, \quad (4.2.38)$$

$$\frac{1}{12} \left( \tilde{P}' \left( \tilde{F} - (T_0 - T)^{d-b} \tilde{W} \right)^3 \right)' = (T_0 - T)^{2a-2b-c-1} \left( a\eta \left( \tilde{F}' - (T_0 - T)^{d-b} \tilde{W}' \right) - b\tilde{F} + d(T_0 - T)^{d-b} \tilde{W} \right), \quad (4.2.39)$$

$$\alpha (T_0 - T)^{d-2} \left( d(d-1)\tilde{W} - a\eta(2d-1)\tilde{W}' + a^2\eta^2\tilde{W}'' \right) + \beta (T_0 - T)^{d-4a} \tilde{W}'''' = -(T_0 - T)^c P. \quad (4.2.40)$$

By inspection we set  $b = d$  in order to retain both  $\tilde{F}$  and  $\tilde{W}$  in (4.2.39). Then in order to maintain a critical balance in equations (4.2.39) and (4.2.38) we set  $b = (a + 1)/3$  and  $c = (4a - 5)/3$ . Since the local pressure must be regular but large  $a$  is restricted to  $0 < a < \frac{5}{4}$ . Using these scalings we can rewrite the local plate equation (4.2.40) as

$$\begin{aligned} & \alpha (T_0 - T)^{\frac{12a-4}{3}} \left( \frac{(a+1)(a-2)}{9} \tilde{W} - \frac{a\eta}{3} (2a-1) \tilde{W}' + a^2 \eta^2 \tilde{W}'' \right) + \beta \tilde{W}'''' \\ & = - (T_0 - T)^{5a-\frac{4}{3}} P. \end{aligned} \quad (4.2.41)$$

The dominant terms are given by

$$\tilde{W}'''' = 0, \quad \frac{1}{3} < a < \frac{5}{4}, \quad (4.2.42)$$

$$\frac{\alpha}{9} \left( -\frac{20}{9} \tilde{W} - \frac{\eta}{3} \tilde{W}' + \eta^2 \tilde{W}'' \right) + \beta \tilde{W}'''' = 0, \quad a = \frac{1}{3}, \quad (4.2.43)$$

$$\frac{(a+1)(a-2)}{9} \tilde{W} - \frac{a\eta}{3} (2a-1) \tilde{W}' + a^2 \eta^2 \tilde{W}'' = 0, \quad 0 < a < \frac{1}{3}. \quad (4.2.44)$$

We require that in the far field the plate displacement must be finite to match with the outer solution. The only way to satisfy this is if  $\tilde{W} = A$ , where  $A$  is a constant. Our inner problem (4.2.38)-(4.2.40) takes the form

$$\frac{(a+1)(a-2)}{9} \tilde{F} - \frac{a\eta}{3} (2a+1) \tilde{F}' + a^2 \eta^2 \tilde{F}'' = \frac{1}{\pi} \text{PV} \int_{-\infty}^{\infty} \frac{\tilde{P}(\hat{\eta}) d\hat{\eta}}{\eta - \hat{\eta}}, \quad (4.2.45)$$

$$\frac{1}{12} \left( \tilde{P}' (\tilde{F} - A)^3 \right)' = a\eta \tilde{F}' - \frac{a+1}{3} (\tilde{F} - A). \quad (4.2.46)$$

Smith et al. [2003] attempted to solve the local problem (4.2.45)-(4.2.46) numerically with  $A = 0$ . They could not find an acceptable smooth solution. The inclusion of an  $A \neq 0$  does not change this. The implication is that the solution of equations (4.2.45) and (4.2.46) should be irregular at some point,  $\eta = -c_1$  such that

$$\tilde{F} \approx |\eta + c_1|^{\frac{2}{3}}, \quad \tilde{P} \approx |\eta + c_1|^{-\frac{1}{3}}, \quad \tilde{W} \approx A, \quad \eta \rightarrow -c_1. \quad (4.2.47)$$

This motivates the consideration of a shorter time scale,

$$X - X_0 = -(T_0 - T)^a c_1 + (T_0 - T)^n \xi, \quad n > a. \quad (4.2.48)$$

By analysing the largest order terms we find that the free surface and pressure behave as

$$f \approx (T_0 - T)^{\frac{2n-a+1}{3}} \tilde{F}_1 + A, \quad p_2 \approx (T_0 - T)^{\frac{5a-5-n}{3}} \tilde{P}_1, \quad (4.2.49)$$

where the  $A$  term takes into account the elastic plate. The scaled free surface and pressure are governed by

$$\tilde{P}'_1(\xi)(\tilde{F}_1(\xi) - A_1)^3 = -12ac_1 (\tilde{F}_1 - C - A_1), \quad (4.2.50)$$

$$a^2 c^2 \tilde{F}'_1(\xi) = \frac{1}{\pi} \text{PV} \int_{-\infty}^{\infty} \frac{\tilde{P}'_1(\hat{\xi}) d\hat{\xi}}{\xi - \hat{\xi}}, \quad (4.2.51)$$

where  $C$  is a constant introduced via integration. The matching conditions are

$$\tilde{F}_1 \approx \lambda_1 \xi^{\frac{2}{3}}, \quad P \approx \lambda_2 \xi^{-\frac{1}{3}}, \quad \xi \rightarrow \infty, \quad (4.2.52)$$

$$\tilde{F}_1 \rightarrow C - A_1, \quad P \approx \lambda_3 |\xi|^{-\frac{1}{3}}, \quad \xi \rightarrow -\infty, \quad (4.2.53)$$

with the  $\lambda$  constants set via

$$\lambda_1 = \left( \frac{12}{ac_1} \right)^{\frac{1}{3}} \frac{3^{\frac{5}{6}}}{2^{\frac{1}{3}}}, \quad \lambda_2 = (12a^5 c_1^5)^{\frac{1}{3}} \left( \frac{2}{3} \right)^{\frac{2}{3}}, \quad \lambda_3 = 2\lambda_2. \quad (4.2.54)$$

The  $\tilde{F}_1 \rightarrow B - A_1$  condition comes from first considering a form of the far field condition  $\tilde{F}_1 \rightarrow \lambda_4 |\xi|^{\frac{2}{3}}$ , and finding that  $\lambda_4$  is required to be non-physically negative at large negative  $\xi$ .

The problem defined by equations (4.2.50)-(4.2.54) can be made identical to that analysed by [Smith et al. \[2003\]](#) by the substitution of  $\tilde{F}_1 - A \rightarrow \tilde{F}_1$ . As such, the presence of the elastic plate does not cause any local changes to the mechanics of touchdown relative to the impact of a liquid with a flat solid

substrate. In the paper by [Smith et al. \[2003\]](#) a numerical solution of equations (4.2.50)-(4.2.54) with  $\tilde{A} = 0$  was presented with a brief description of their method. Their method involves substituting equation (4.2.50) into equation (4.2.51) to obtain an equation for only  $F$  which is then iterated upon until a converged solution is found. The details of their numerical procedure are not given. I could not find a converged solution using their method, despite trying a range of parameters such as grid resolutions and distance the far field conditions are imposed. A variety of numerical schemes were used and none gave a converged solution. Despite corresponding with the lead author of the work, I could not replicate their results.

### 4.3 Results

For comparison with later results, and validation against other air-cushioning works, we first present a set of results with a rigid solid substrate at  $y = 0$ . In Figure 4.3.1 we show time evolution of the free surface and pressure. Figure 4.3.1 shows the same qualitative features seen in [Smith et al. \[2003\]](#), although the initial free surface shapes are different. Here a free surface equation of  $F(x, t) = x^2/2 - t$  is used, where in [Smith et al. \[2003\]](#)  $F(x, t) = x^2 - t$  was used. We have the 1/2 in our shape from considering circular droplets. Despite this difference the underlying features of air cushioning are the same. We initially see the droplet uniformly moving at a velocity very close to  $-1$ . As the gap between the lowest part of the droplet, initially at  $x = 0$  and the substrate shrinks we see pressure start to rise and the centre of the droplet slow then stop its decent. As the centre of the droplet slows areas away from  $x = 0$  encounter a lower pressure and continue to move downwards. This causes the lowest part of the droplet to change from a single minimum to two symmetrical minima. The lowest part of the free surface continues to move out and down with the maximal pressure constantly increasing until our iterative procedure cannot converge in a reasonable time, at which point we stop the simulation. Touchdown has been significantly delayed

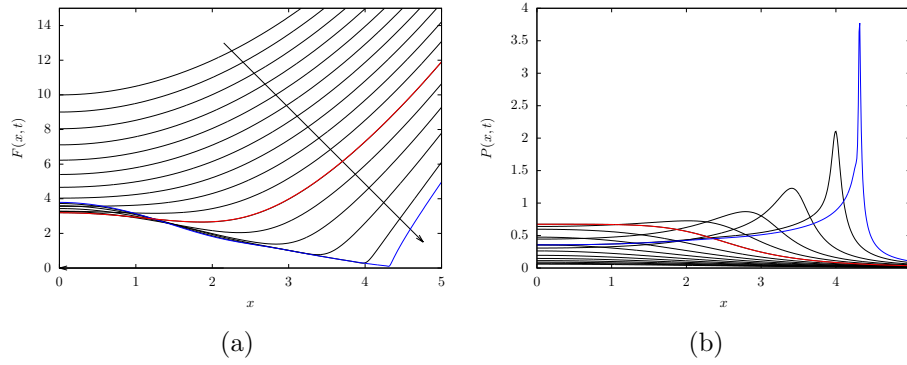


Figure 4.3.1: Time evolution of the free surface (a) and pressure (b) with a rigid substrate. Curves are taken at time intervals of  $t = 1$  and at the time step before termination of the simulation. The red line corresponds to time  $t = 0$  and blue to the final iteration.

by the air-cushioning effect, occurring at time  $t = 4.601$  rather than time  $t = 0$ . The touchdown occurs as  $x = \pm 4.51$ . Both the touchdown locations and time of touchdown match the values given by Hicks and Purvis [2017] to two decimal places.

In Figures 4.3.2 and 4.3.3 we show the free surface, substrate and pressure evolution over time for a substrate with an elastic plate of length  $L = 10$  and parameters  $\alpha = \beta = 1.0$ . The presence of the elastic plate acts to delay the time of impact. As the pressure begins to build under the centre of the droplet it begins to move both the free surface and elastic part of the substrate. Since there are two moveable surfaces for the pressure to work against the influence of the pressure on the free surface alone is reduced relative to the rigid substrate case, as seen in Figure 4.3.2a. However the gap between the free surface and substrate, depicted in Figure 4.3.3 shows a qualitatively similar behaviour to that of the rigid case from Figure 4.3.1. The main difference we see is the elastic plate acts to delay touchdown. For the plate parameters in Figure 4.3.2 touchdown occurs at a time  $t = 8.875$  compared with  $t = 4.601$  for the rigid case. This increased touchdown time also causes the droplet to spread further, touching down at  $x = \pm 5.11$  and trapping a higher volume gas bubble of 33.16 compared to 16.4 for the rigid plate.

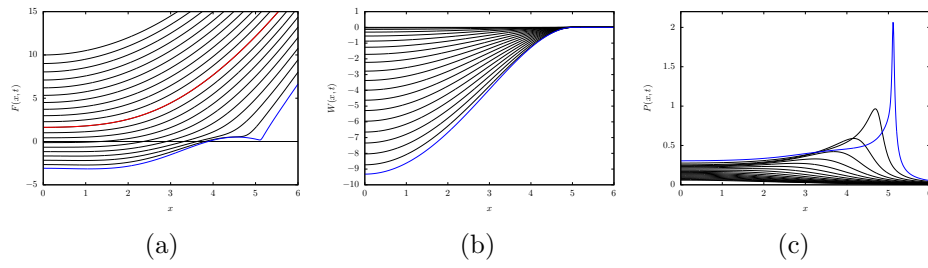


Figure 4.3.2: Time evolution of the free surface (a), elastic plate deformation (b) and pressure (c) for a substrate with elastic parameters  $L = 10$ ,  $\alpha = \beta = 1.0$ . Curves are taken at time intervals of  $t = 1$  and at the time step before termination of the simulation. The red line corresponds to time  $t = 0$  and blue to the final iteration.

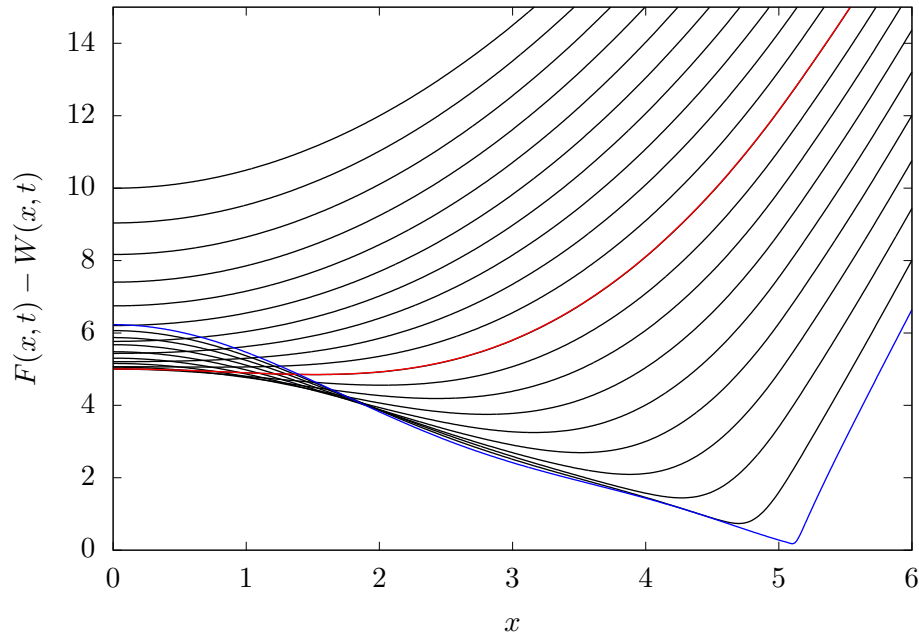


Figure 4.3.3: Time evolution of the distance between the free surface and substrate for elastic parameters  $L = 10$ ,  $\alpha = \beta = 1.0$ . Curves are taken at time intervals of  $t = 1$  and at the time step before termination of the simulation. The red line corresponds to time  $t = 0$  and blue to the final iteration.

In Figures 4.3.2 and 4.3.3 the touchdown occurs almost immediately beyond the edge of the elastic plate. By varying plate parameters we can cause touchdown to occur on the plate itself. In Figure 4.3.4 we have a plate of length  $L = 20$  and parameters  $\alpha = \beta = 1.0$ . Touchdown occurs at  $x = \pm 8.12$ , significantly after the 5.11 of our previous case but still on the elastic plate which extends to  $x = \pm 10$ . It takes significantly longer for this droplet to touch down, occurring at time  $t = 30.6$  and trapping a much larger gas bubble of volume 54.45.

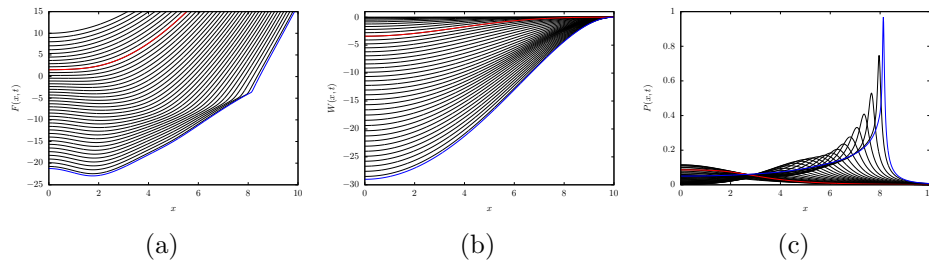


Figure 4.3.4: Time evolution of the free surface (a), elastic plate deformation (b) and pressure (c) for a substrate with elastic parameters  $L = 20$ ,  $\alpha = \beta = 1.0$ . Curves are taken at time intervals of  $t = 1$  and at the time step before termination of the simulation. The red line corresponds to time  $t = 0$  and blue to the final iteration.

In Figures 4.3.5 and 4.3.6 we show time evolution of the gap between free surface and substrate  $F - W$  and pressure  $P$  for a range of plate parameters  $\alpha$  and  $\beta$ . The Figures are presented such that reading down a column fixes  $\beta$  with  $\alpha$  increasing and reading across a row fixes  $\alpha$  with  $\beta$  increasing. We can immediately see that increases in both  $\alpha$  and  $\beta$  cause a reduction in the volume of the bubble trapped at touchdown. In Figure 4.3.6 we also see the pressure at both the touchdown points and more generally across the gas increasing with both  $\alpha$  and  $\beta$ . Not shown in Figures 4.3.5 and 4.3.6 but of interest is the impact of  $\alpha$  and  $\beta$  on touchdown time, in general the more flexible the elastic plate the longer touch down takes. For example, for  $\beta = 0.5$  and  $\alpha = 0.5, 1.0$  and  $2.0$  the touchdown times are  $t = 10.02, 9.89$  and  $9.26$  respectively. Physically these results make sense, since the pressure acts on both the free surface and solid substrate we can decelerate the gap  $F - W$  to near zero speed with a much lower pressure than would be needed to stop the free surface with a rigid substrate. This causes the lower pressures at touch down we see in Figure 4.3.6 and further throughout this chapter. It also explains the longer touch down time, as the gap  $F - W$  is easier to decelerate than just the free surface  $F$ .

In the previous results we considered only the case where the centre of the elastic plate was at the origin,  $x_0 = 0$ . However, we formulated the problem to allow us any combination of plate centre  $x_0$  and plate length  $L$ . From here we will be considering the effect moving the impact location away from the centre of

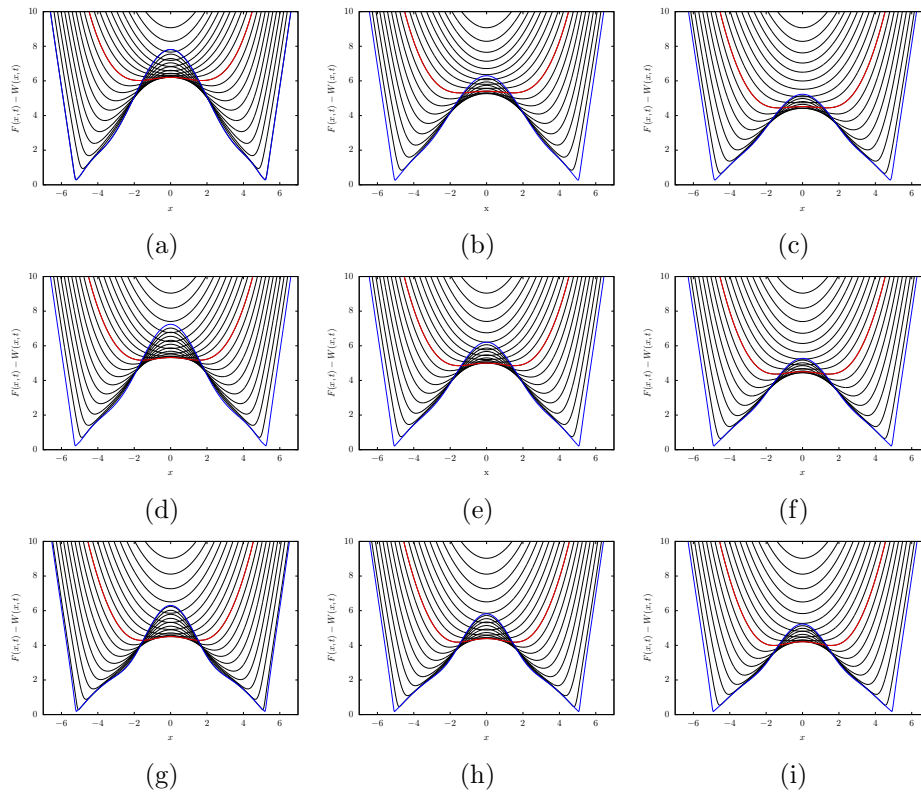


Figure 4.3.5: A set of plots showing the time evolution of the gap between free surface and substrate  $F - W$  for different plate parameters. In each Figure the plate length  $L = 10$ . Figures are arranged such that columns from left to right have  $\beta = 0.5, 1.0$  and  $2.0$  while rows from top to bottom have  $\alpha = 0.5, 1.0$  and  $2.0$ .

the elastic plate has on the air cushioning mechanics, and any resulting effects it has on touchdown. By moving the impact away from the centre of the elastic plate we introduce a variable element of asymmetry into the problem which can produce some interesting results. In Figure 4.3.7 we see the effect of changing the plate position, we keep the plate parameters of  $\alpha = \beta = 1.0$  and  $L = 10$  but move the plate centre across  $x_0 = 0, 2, 4, 6$  which is shown in each column of Figure 4.3.7 respectively. The rows, from top to bottom, show the free surface  $F$ , gap between the free surface and substrate  $F - W$ , substrate deformation  $W$ , pressure  $P$ , horizontal gas velocity at the centre of the gap  $U(x, y = (F - W)/2, t)$  and horizontal gas flux. Note the difference in  $x$ -ranges in Figures showing the substrate deformation and horizontal velocity versus the other Figures. In Figures 4.3.7f-4.3.7h we see the free surface gap in  $x < 0$  moves qualitatively similar to both the centred substrate in Figure 4.3.7e and the classical problem of a

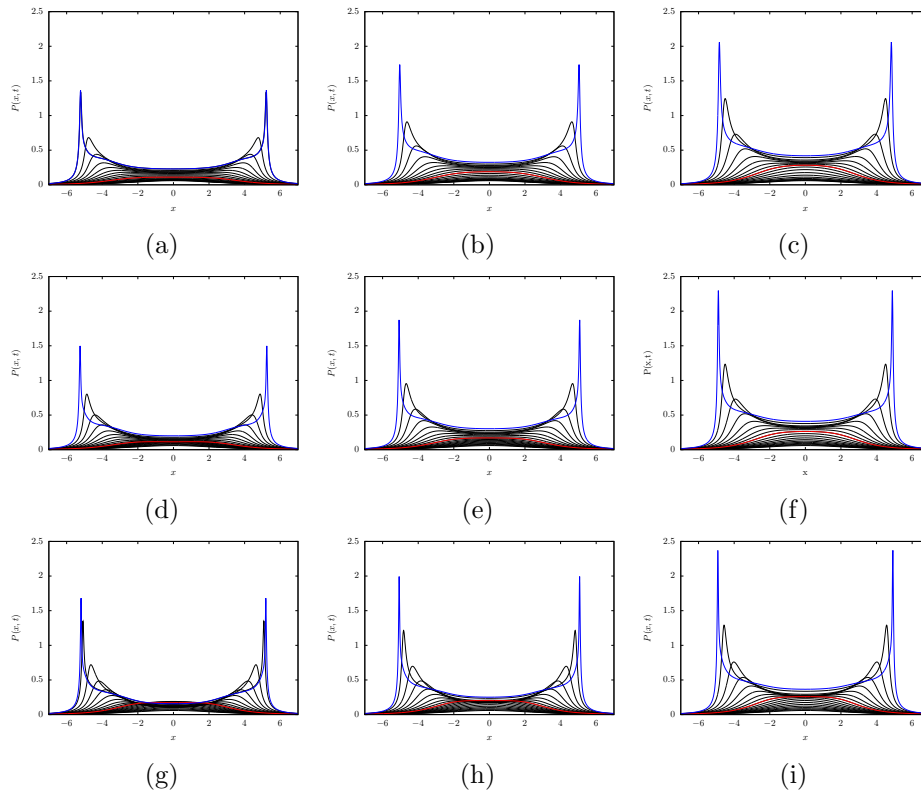


Figure 4.3.6: A set of plots showing the time evolution of the gas pressure  $P$  for different plate parameters. In each Figure the plate length  $L = 10$ . Figures are arranged such that columns from left to right have  $\beta = 0.5, 1.0$  and  $2.0$  while rows from top to bottom have  $\alpha = 0.5, 1.0$  and  $2.0$ .

simple solid substrate shown in Figure 4.3.1a. Unlike the symmetric situations considered earlier we see a touchdown at only one point.

An unexpected result seen in the pressure. In Figures 4.3.7n-4.3.7p we can see the maximum pressure under the touchdown points is markedly higher than in the symmetric case 4.3.7m. Not only that, but the pressure in the centre of droplet is also higher in the off-centre cases. The reason for this can best be seen in the fluxes 4.3.7u-4.3.7x. As the free surface moves towards the solid substrate the air must be pushed out of the way, in the symmetric case 4.3.7u we see that the flux on either side is balanced, with both touchdown points pushing air out of the squeeze film either into the bubble or towards the far field. In the off-centre case however the one touchdown point pushes the air not into the 'bubble' but out towards both far fields, this can best be seen in Figure 4.3.7v. In order for this to happen there must be a higher pressure under the centre of the droplet

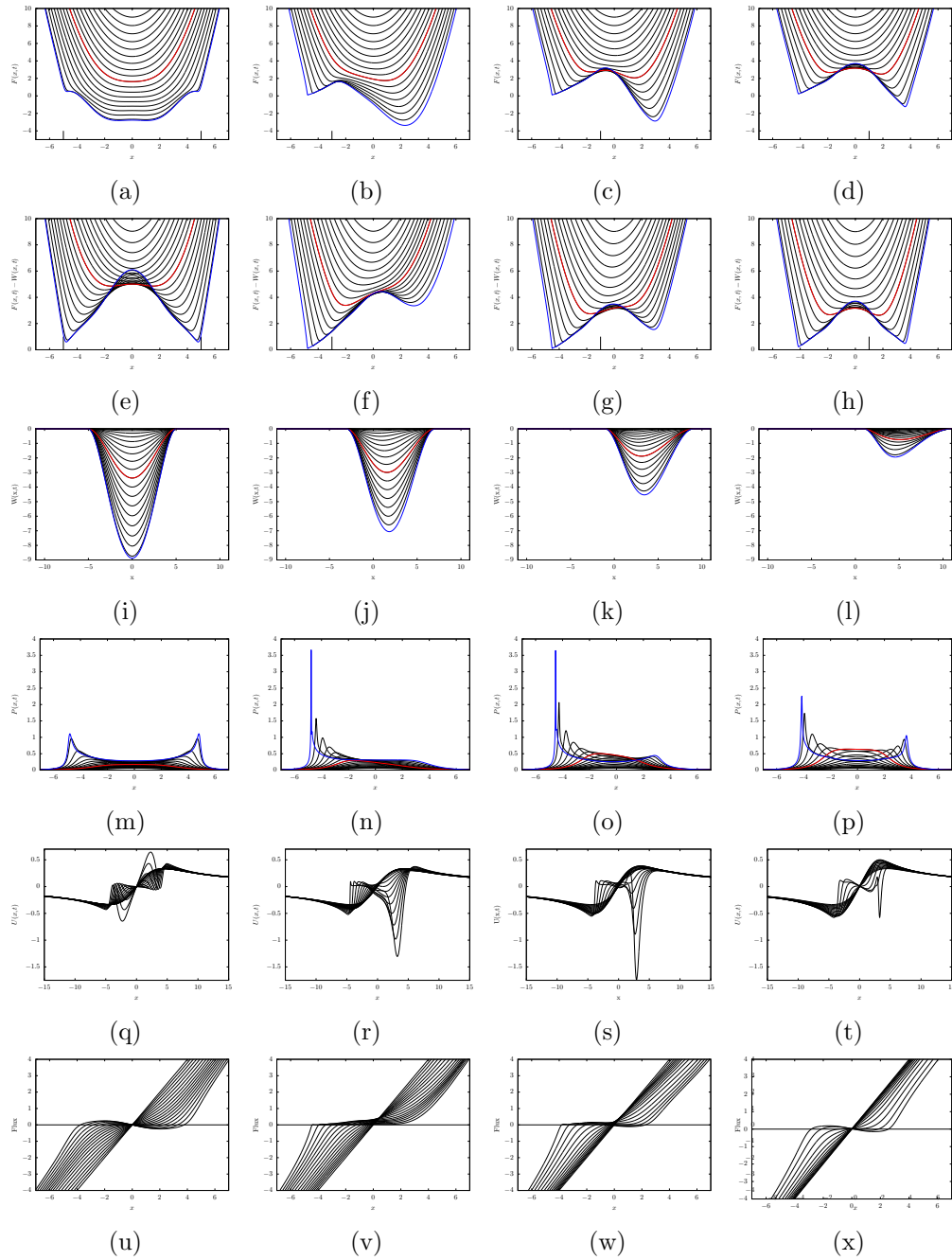


Figure 4.3.7: A set of plots showing the effect of altering the location of the elastic plate. Columns from left to right have plate centres at  $x_0 = 0, 2, 4$  and  $6$  respectively. Rows from top to bottom show the free surface  $F(x, t)$ , gap between free surface and substrate  $F(x, t) - W(x, t)$ , plate deformation  $W(x, t)$ , pressure  $P(x, t)$  and horizontal velocity of the gas at the centre of the gap  $U(x, y = (F(x, t) - W(x, t))/2, t)$  and horizontal flux of the gas. In all Figures the plate has parameters  $\alpha = 1.0, \beta = 1.0$  and a length of  $L = 10$ . In the first two rows of Figures the vertical lines show the edge of the elastic plate.

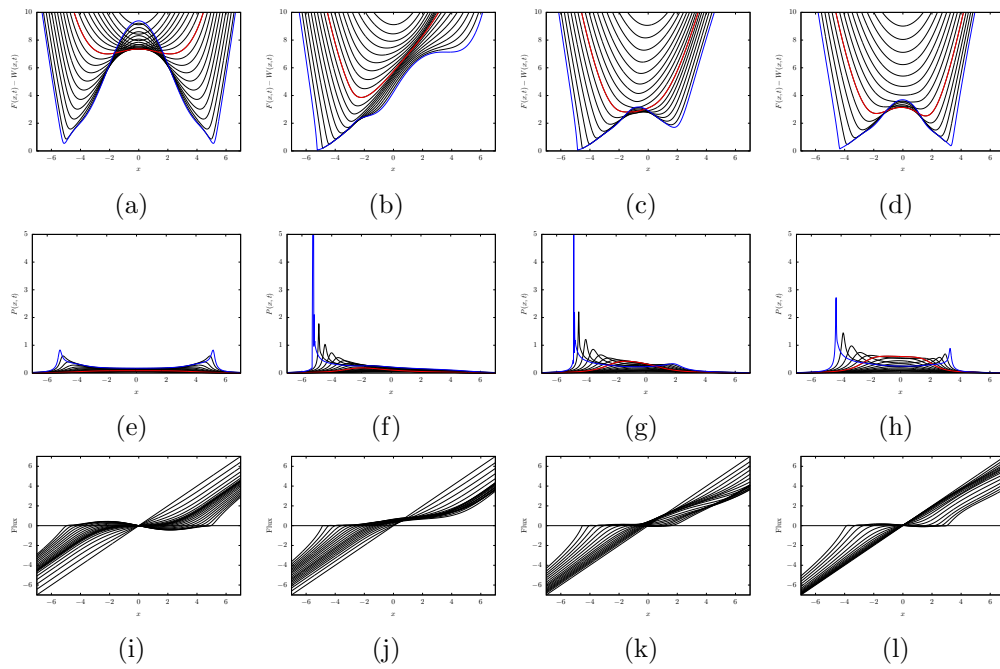


Figure 4.3.8: A set of plots showing the effect of altering the location of the elastic plate. Columns from left to right have plate centres at  $x_0 = 0, 2, 4$  and  $6$  respectively. Rows from top to bottom show the gap between free surface and substrate  $F(x, t) - W(x, t)$ , pressure  $P(x, t)$  and horizontal flux of the gas. In all Figures the plate has parameters  $\alpha = 0.3, \beta = 0.3$  and a length of  $L = 10$ . In the first two rows of Figures the vertical lines show the edge of the elastic plate.

which then requires the squeeze film under the touchdown point to have a higher pressure. We see this effect in a wide range of plate parameters, in Figure 4.3.8l we show the same effect for plate parameters  $\alpha = \beta = 0.3$ .

As we have seen from Figures 4.3.7-4.3.8 introducing even a small level of asymmetry by moving the plate centre from  $x_0 = 0$  to  $x_0 = 2$  causes a dramatic change in the air cushioning behaviour. Touch down occurs in only one place and with a gas pressure which is far more complicated than the symmetric case, being much higher close to the one touch down point but generally lower elsewhere.

# Impact of a droplet which contains a trapped gas cavity

---

## 5.1 Problem definition

After investigating air cushioning and the asymptotic behaviour of the touch down points at the pre-impact stage we now seek an understanding of the spreading and impact of the cushioned droplet with a solid substrate. Unlike the previous sections an elastic substrate will not be included in this section. We will only consider here the two dimensional impact with solid substrates for simplicity. There are several factors complicating the definition of our problem. We must choose a model for the free surface shape and trapped gas. We will be analysing a situation where the free surface at the initial contact points is smooth and flat. We begin our problem definition by considering a droplet of radius  $R$  with a trapped cavity of length  $2L$  and height at its centre  $H$ . We introduce the length scale  $L$  such that the two initial impact points are located at  $x = \pm 1$ . We introduce the non-dimensional free surface shape such that

$$y = \begin{cases} \frac{L}{R}f(x), & |x| > 1, \\ \frac{H}{L}g(x), & |x| < 1. \end{cases} \quad (5.1.1)$$

Where  $L/R$  is the scale of the droplet free surface and  $H/L$  is the scale of the trapped cavity. If  $H/L \approx L/R$  then we have the situation where both the outer

droplet and inner cavity are of the same scale which gives rise to a coupled problem where there exists a dynamic contact point on either side of each contact region. By considering the scales and simulations from the previous chapter we have  $H \approx 4R\delta^2$  and  $L \approx 4R\delta$  where  $\delta \ll 1$ . With these scales we see that  $H/L$  is indeed of the same small scale as  $L/R = \epsilon \ll 1$ . As such we replace the split free surface shape from equation (5.1.1) with one of the form,

$$y = \epsilon F(x), \quad (5.1.2)$$

in the non-dimensional variables.

We need a model for the behaviour of the gas in the trapped cavity. We make the assumption that the gas pressure is uniform (independent of position) and that the gas is ideal. Gas compressibility was not included in the previous sections work on air cushioning as that was not the main focus of that chapter. However gas compressibility has been included in air cushioning models by ?. We start with the gas in equilibrium. As we can see in Figure 4.3.5 for a large portion of the cavity the free surface is approximately stationary and pressure distribution is flat. The assumption that the gas is ideal and pressure distribution independent of position is influenced by, but not entirely justified by, the dynamics of the pre-impact air cushioning. Instead we use it to simplify an already highly complicated non-linear problem.

We assume the flow is irrotational and the liquid is inviscid and incompressible. The liquid impacts at constant speed  $V$  normal to the flat solid surface occupying  $y = 0$ , see Figure 5.1.1. We introduce the displacement potential  $\phi(x, y, t)$ , such that

$$\frac{\partial \phi}{\partial x} = X(x, y, t), \quad \frac{\partial \phi}{\partial y} = Y(x, y, t), \quad (5.1.3)$$

where  $X$  and  $Y$  are the liquid displacements in the  $x$  and  $y$  directions respectively. The axis  $x$  points along the flat solid surface and  $y$  perpendicular to it, with positive  $y$  towards the liquid droplet. The origin is placed on the solid surface under the centre of the liquid droplet.

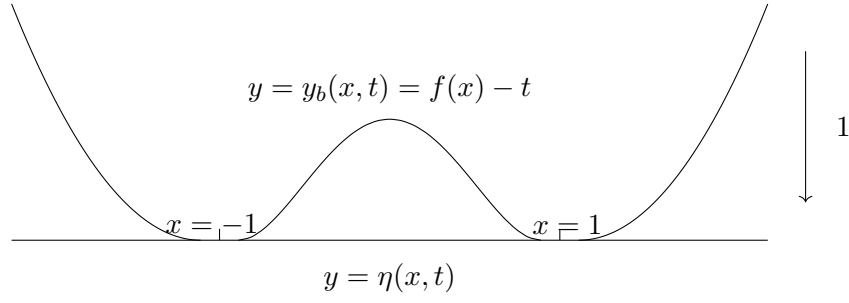


Figure 5.1.1: A schematic showing the problem being considered after inversion from a liquid impacting solid problem to a solid impacting liquid one.

We introduce the following scales in this chapter.  $L$ , the initial half length of the cavity, as the length scale.  $H$  as the scale of liquid displacements.  $HL$  as the scale of the displacement potential. The constant speed of impact  $V$  as the velocity scale. The ratio  $H/V$  is taken as the time scale and  $\rho V^2/\epsilon$  as pressure scale. Under these scales the touch down points are initially at  $x = \pm 1$ . The non-dimensional linearised Wagner model for the displacement potential is given by

$$\nabla^2 \phi = 0, \quad y < 0, \quad (5.1.4)$$

$$\frac{\partial \phi}{\partial x} = 0, \quad y = 0, x \notin [-b, -a] \cup [a, b] \quad (5.1.5)$$

$$\frac{\partial \phi}{\partial y} = f(x) - h(t) = y_b(x, t), \quad y = 0, x \in [-b, -a] \cup [a, b], \quad (5.1.6)$$

$$\phi \rightarrow 0, \quad x^2 + y^2 \rightarrow \infty, \quad (5.1.7)$$

$$p_c(t) = C_0 V_c(t)^{-\gamma}, \quad -a \leq x \leq a, \quad (5.1.8)$$

where the points  $x = -b(t), x = -a(t), x = a(t), x = b(t)$  are the four contact points from left to right. The system of equations (5.1.4)-(5.1.8) are solved subject to the initial conditions

$$a(0) = 1, \quad b(0) = 1, \quad V_c(0) = \int_{-1}^1 f(x) dx, \quad \phi = 0. \quad (5.1.9)$$

In equation (5.1.8)  $p_c(t)$  is the pressure in the cavity,  $V_c(t)$  is the volume of the cavity,  $\gamma$  is the gas constant, equal to 1.4 for air, and  $C_0 = p_c(0)/V_c(0)^{-\gamma}$  is the

compressibility factor. All other symbols are reused from earlier in this chapter but with the understanding that from here on all quantities are dimensionless unless explicitly stated otherwise. In the set of equations (5.1.4)-(5.1.8) we have inverted the problem, so that rather than a liquid droplet approaching a flat solid surface from above a flat liquid occupies the lower half plane with an appropriately shaped solid approaching it from above. Performing this transformation does not alter the leading order dynamics in anyway but allows for the use of some complex analysis tools to solve the problem.

## 5.2 Problem Solution

We now solve the system of equations (5.1.4)-(5.1.8) subject to initial conditions (5.1.9). A sketch of this boundary value problem can be seen in Figure 5.2.1. From conservation of mass (5.1.4) and definition of the displacement potential (5.1.3) we can write  $X_x + Y_y = 0$ . By requiring there be no vorticity in the liquid we have

$$\nabla \times \nabla \phi = \nabla \times (X(x, y, t), Y(x, y, t)) = \mathbf{0}, \quad (5.2.1)$$

which provides  $X_y - Y_x = 0$ . These two expressions linking  $X$  and  $Y$  are the Cauchy-Riemann equations for the complex displacement  $w(z, t) = X(z, t) - iY(z, t)$ . The function  $w(z, t)$  is analytic in the lower half plane. In the contact zones,  $x \in [-b, -a] \cup [a, b]$  boundary condition (5.1.6) provides  $Y(x, y = 0, t) = y_b(x, t)$ . Along the rest of the boundary  $y = 0$  we have  $X(x, y = 0, t) = 0$ . We introduce a function  $G(z)$ , which is analytic in the lower half plane, on  $y = 0$ .  $G(x)$  is purely imaginary for  $a(t) \leq |x| \leq b(t)$ , and real otherwise. The function

$$\begin{array}{ccccccccc} \underbrace{\hspace{1.5cm}}_{x = -b(t)} & \underbrace{\hspace{1.5cm}}_{x = -a(t)} & \underbrace{\hspace{1.5cm}}_{x = a(t)} & \underbrace{\hspace{1.5cm}}_{x = b(t)} & \underbrace{\hspace{1.5cm}}_{x} \\ \frac{\partial \phi}{\partial x} = 0 & \frac{\partial \phi}{\partial y} = y_b(x, t) & \frac{\partial \phi}{\partial x} = 0 & \frac{\partial \phi}{\partial y} = y_b(x, t) & \frac{\partial \phi}{\partial x} = 0 \\ \nabla^2 \phi(x, y, t) = 0 \end{array}$$

Figure 5.2.1: Sketch of the boundary value problem (5.1.4)-(5.1.8).

$G(z, t) = \sqrt{(z^2 - b^2)(z^2 - a^2)}$ , has the correct behaviour on the boundary  $z = x - i0$ . The function  $G(z)$  takes the values of

$$G(x - 0i, t) = \begin{cases} \sqrt{(x^2 - a^2)(x^2 - b^2)}, & x \leq -b, \\ i\sqrt{(b^2 - x^2)(x^2 - a^2)}, & -b \leq x \leq -a, \\ -\sqrt{(b^2 - x^2)(x^2 - a^2)}, & -a \leq x \leq a, \\ -i\sqrt{(b^2 - x^2)(x^2 - a^2)}, & a \leq x \leq b, \\ \sqrt{(x^2 - b^2)(x^2 - a^2)}, & b \leq x, \end{cases} \quad (5.2.2)$$

along the boundary  $y = 0$  when we approach from the lower half plane.

We introduce a new unknown function  $F(z, t) = w(z, t)G(z, t)$  which is analytic in the lower half plane by construction. The real values of  $F$  along the boundary  $y = 0$  are

$$\Re F(x, t) = \begin{cases} 0, & x \leq -b, \\ y_b(x, t)H(x, t), & -b \leq x \leq -a, \\ 0, & -a \leq x \leq a, \\ -y_b(x, t)H(x, t), & a \leq x \leq b, \\ 0, & b \leq x, \end{cases} \quad (5.2.3)$$

where  $H(x, t) = \sqrt{(b^2 - x^2)(x^2 - a^2)}$  can now be solved. We will use the Hilbert equation to relate real and complex parts of the analytic function  $F(z, t)$  along the boundary  $y = 0$ . However the Hilbert equation requires  $F(x, t) \rightarrow 0$  as  $|x| \rightarrow \infty$ . It is well known that the vertical displacement  $Y(x, t) \approx 1/x^2$  as  $x \rightarrow 0$ . This result was derived by [Korobkin \[1996\]](#) for a more simple set of boundary conditions. However in the limit  $|x| \rightarrow \infty$  the influence of the two finite contact regions become negligible and the far field behaviour holds. We can see that  $G(x, t) \approx x^2$  in the far field, so it is reasonable to assume  $F(x, t) \approx -i\phi_y(x, t)/x^2 \rightarrow i\bar{A}(t)$  where  $\bar{A}$  is a real function. We can now use the Hilbert equation for the function  $F(z, t) - i\bar{A}(t)$  since it decays in the far field

by construction and is analytic in the lower half plane. We obtain

$$\Im(F(x, t)) - \bar{A}(t) = \frac{1}{\pi} \int_{-\infty}^{\infty} \frac{\Re F(\tau, t) d\tau}{\tau - x}. \quad (5.2.4)$$

From equation (5.2.4) we can extract the vertical displacement away from the contact regions,

$$Y(x, 0, t) = \begin{cases} \frac{1}{\pi \sqrt{(b^2 - x^2)(a^2 - x^2)}} \left( A(t) - 2 \int_a^b \frac{\tau y_b(\tau, t) \sqrt{(b^2 - \tau^2)(\tau^2 - a^2)}}{\tau^2 - x^2} d\tau \right), & -a \leq x \leq a, \\ \frac{1}{\pi \sqrt{(x^2 - b^2)(x^2 - a^2)}} \left( 2 \int_a^b \frac{\tau y_b(\tau, t) \sqrt{(b^2 - \tau^2)(\tau^2 - a^2)}}{\tau^2 - x^2} d\tau - A(t) \right), & b \leq |x|. \end{cases} \quad (5.2.5)$$

where we have set  $A(t) = \pi \bar{A}(t)$ .

The Wagner condition requires the vertical displacement at the contact points to be finite, this provides the two conditions

$$A(t) + 2 \int_a^b \tau y_b(\tau, t) \sqrt{\frac{\tau^2 - a^2}{b^2 - \tau^2}} d\tau = 0, \quad (5.2.6)$$

$$2 \int_a^b \tau y_b(\tau, t) \sqrt{\frac{b^2 - \tau^2}{\tau^2 - a^2}} d\tau - A(t) = 0. \quad (5.2.7)$$

An implicit assumption in the Wagner model requires that the contact points do not stop moving, as if they do we cannot maintain a finite displacement at the contact point. We therefore require  $\dot{b}(t) > 0$  and  $\dot{a}(t) < 0$ . In the Wagner impact of a parabolic free surface with a rigid plate in two dimension there are only two contact points. The location of these points behave as  $a(t) \approx 2\sqrt{t}$  in two dimensions, so that their velocity only reaches zero as  $t \rightarrow \infty$ . In our problem it is possible for the velocity of the inner contact line to become zero in finite time due to the influence of the gas trapped in the cavity.

We remove singularities from the integrands in the Wagner conditions (5.2.6)-

(5.2.7) by the use of a substitution  $\tau = (b - a) \sin^2(\theta) + a$ , providing

$$4(b - a) \int_0^{\frac{\pi}{2}} \sin^2(\theta) ((b - a) \sin^2(\theta) + a) y_b((b - a) \sin^2(\theta) + a, t) \sqrt{\frac{(b - a) \sin^2(\theta) + 2a}{(b - a) \sin^2(\theta) + b + a}} d\theta + A(t) = 0, \quad (5.2.8)$$

$$4(b - a) \int_0^{\frac{\pi}{2}} \cos^2(\theta) ((b - a) \sin^2(\theta) + a) y_b((b - a) \sin^2(\theta) + a, t) \sqrt{\frac{(b - a) \sin^2(\theta) + b + a}{(b - a) \sin^2(\theta) + 2a}} d\theta - A(t) = 0. \quad (5.2.9)$$

Equations (5.2.8)-(5.2.9) are differentiated in time providing these two ordinary differential equations for the contact line velocities,

$$c_{11}(t)\dot{a} + c_{12}(t)\dot{b} + c_{13}(t) + \dot{A}(t) = 0, \quad (5.2.10)$$

$$c_{21}(t)\dot{a} + c_{22}(t)\dot{b} + c_{23}(t) - \dot{A}(t) = 0, \quad (5.2.11)$$

where

$$\begin{aligned} c_{11}(t) &= -4 \int_0^{\frac{\pi}{2}} \sin^2(\theta) ((b - a) \sin^2(\theta) + a) y_b((b - a) \sin^2(\theta) + a, t) \sqrt{\frac{(b - a) \sin^2(\theta) + 2a}{b + a + (b - a) \sin^2(\theta)}} d\theta + 4(b - a) \int_0^{\frac{\pi}{2}} \cos^2(\theta) \sin^2(\theta) y_b((b - a) \sin^2(\theta) + a, t) \sqrt{\frac{(b - a) \sin^2(\theta) + 2a}{b + a + (b - a) \sin^2(\theta)}} d\theta \\ &\quad + 4(b - a) \int_0^{\frac{\pi}{2}} \cos^2(\theta) \sin^2(\theta) ((b - a) \sin^2(\theta) + a) y'_b((b - a) \sin^2(\theta) + a, t) \sqrt{\frac{(b - a) \sin^2(\theta) + 2a}{b + a + (b - a) \sin^2(\theta)}} d\theta + 2(b - a) \int_0^{\frac{\pi}{2}} \frac{\sin^2(\theta) (2 - \sin^2(\theta)) ((b - a) \sin^2(\theta) + a) y_b((b - a) \sin^2(\theta) + a, t) d\theta}{\sqrt{((b - a) \sin^2(\theta) + 2a)(b + a + (b - a) \sin^2(\theta))}} \\ &\quad - 2(b - a) \int_0^{\frac{\pi}{2}} \sin^2(\theta) \cos^2(\theta) ((b - a) \sin^2(\theta) + a) y_b((b - a) \sin^2(\theta) + a, t) \sqrt{\frac{(b - a) \sin^2(\theta) + 2a}{(b + a + (b - a) \sin^2(\theta))^3}} d\theta \end{aligned}$$

$$\begin{aligned}
c_{12}(t) = & 4 \int_0^{\frac{\pi}{2}} \sin^2(\theta) ((b-a) \sin^2(\theta) + a) y_b((b-a) \sin^2(\theta) \\
& + a, t) \sqrt{\frac{(b-a) \sin^2(\theta) + 2a}{b+a+(b-a) \sin^2(\theta)}} d\theta \\
& + 4(b-a) \int_0^{\frac{\pi}{2}} \sin^4(\theta) y_b((b-a) \sin^2(\theta) + a, t) \sqrt{\frac{(b-a) \sin^2(\theta) + 2a}{b+a+(b-a) \sin^2(\theta)}} d\theta \\
& + 4(b-a) \int_0^{\frac{\pi}{2}} \sin^4(\theta) ((b-a) \sin^2(\theta) + a) y'_b((b-a) \sin^2(\theta) \\
& + a, t) \sqrt{\frac{(b-a) \sin^2(\theta) + 2a}{b+a+(b-a) \sin^2(\theta)}} d\theta \\
& + 2(b-a) \int_0^{\frac{\pi}{2}} \frac{\sin^4(\theta) ((b-a) \sin^2(\theta) + a) y_b((b-a) \sin^2(\theta) + a, t) d\theta}{\sqrt{((b-a) \sin^2(\theta) + 2a)(b+a+(b-a) \sin^2(\theta))}} \\
& - 2(b-a) \int_0^{\frac{\pi}{2}} \sin^2(\theta) (1 + \sin^2(\theta)) ((b-a) \sin^2(\theta) + a) y_b((b-a) \sin^2(\theta) \\
& + a, t) \sqrt{\frac{(b-a) \sin^2(\theta) + 2a}{(b+a+(b-a) \sin^2(\theta))^3}},
\end{aligned}$$

$$\begin{aligned}
c_{13}(t) = & 4(b-a) \int_0^{\frac{\pi}{2}} \sin^2(\theta) ((b-a) \sin^2(\theta) + a) \dot{y}_b((b-a) \sin^2(\theta) \\
& + a, t) \sqrt{\frac{(b-a) \sin^2(\theta) + 2a}{(b-a) \sin^2(\theta) + a + b}}.
\end{aligned}$$

$$\begin{aligned}
c_{21}(t) = & -4 \int_0^{\frac{\pi}{2}} ((b-a) \sin^2(\theta) + a) \cos^2(\theta) y_b((b-a) \sin^2(\theta) \\
& + a, t) \sqrt{\frac{b+a+(b-a) \sin^2(\theta)}{(b-a) \sin^2(\theta) + 2a}} d\theta \\
& + 4(b-a) \int_0^{\frac{\pi}{2}} \cos^4(\theta) y_b((b-a) \sin^2(\theta) + a, t) \sqrt{\frac{b+a+(b-a) \sin^2(\theta)}{(b-a) \sin^2(\theta) + 2a}} d\theta \\
& + 4(b-a) \int_0^{\frac{\pi}{2}} \cos^4(\theta) ((b-a) \sin^2(\theta) + a) y'_b((b-a) \sin^2(\theta) \\
& + a, t) \sqrt{\frac{b+a+(b-a) \sin^2(\theta)}{(b-a) \sin^2(\theta) + 2a}} d\theta \\
& + 2(b-a) \int_0^{\frac{\pi}{2}} \frac{\cos^4(\theta) ((b-a) \sin^2(\theta) + a) y_b((b-a) \sin^2(\theta) + a, t) d\theta}{\sqrt{(b+a+(b-a) \sin^2(\theta))((b-a) \sin^2(\theta) + 2a)}} \\
& - 2(b-a) \int_0^{\frac{\pi}{2}} (2 - \sin^2(\theta)) \cos^2(\theta) ((b-a) \sin^2(\theta) + a) y_b((b-a) \sin^2(\theta) \\
& + a, t) \sqrt{\frac{b+a+(b-a) \sin^2(\theta)}{((b-a) \sin^2(\theta) + 2a)^3}},
\end{aligned}$$

$$\begin{aligned}
c_{22}(t) &= 4 \int_0^{\frac{\pi}{2}} \cos^2(\theta) ((b-a) \sin^2(\theta) + a) y_b ((b-a) \sin^2(\theta) \\
&\quad + a, t) \sqrt{\frac{b+a+(b-a)\sin^2(\theta)}{(b-a)\sin^2(\theta)+2a}} d\theta + 4(b \\
&\quad - a) \int_0^{\frac{\pi}{2}} \sin^2(\theta) \cos^2(\theta) y_b ((b-a) \sin^2(\theta) + a, t) \sqrt{\frac{b+a+(b-a)\sin^2(\theta)}{(b-a)\sin^2(\theta)+2a}} d\theta \\
&\quad + 4(b-a) \int_0^{\frac{\pi}{2}} \sin^2(\theta) \cos^2(\theta) ((b-a) \sin^2(\theta) + a) y_b' ((b-a) \sin^2(\theta) \\
&\quad + a, t) \sqrt{\frac{b+a+(b-a)\sin^2(\theta)}{(b-a)\sin^2(\theta)+2a}} + 2(b \\
&\quad - a) \int_0^{\frac{\pi}{2}} \frac{\cos^2(\theta) (1 + \sin^2(\theta)) ((b-a) \sin^2(\theta) + a) y_b ((b-a) \sin^2(\theta) + a, t) d\theta}{\sqrt{(b+a+(b-a)\sin^2(\theta))((b-a)\sin^2(\theta)+2a)}} \\
&\quad - 2(b-a) \int_0^{\frac{\pi}{2}} \sin^2(\theta) \cos^2(\theta) ((b-a) \sin^2(\theta) + a) y_b ((b-a) \sin^2(\theta) \\
&\quad + a, t) \sqrt{\frac{b+a+(b-a)\sin^2(\theta)}{((b-a)\sin^2(\theta)+2a)^3}},
\end{aligned}$$

$$\begin{aligned}
c_{23}(t) &= 4(b-a) \int_0^{\frac{\pi}{2}} \cos^2(\theta) ((b-a) \sin^2(\theta) + a) \dot{y}_b ((b-a) \sin^2(\theta) \\
&\quad + a, t) \sqrt{\frac{b+a+(b-a)\sin^2(\theta)}{(b-a)\sin^2(\theta)+2a}} d\theta.
\end{aligned}$$

By rearranging equations (5.2.10)-(5.2.11) we then have the evolution of the contact line velocities given by

$$\frac{da}{dt} = \frac{c_{12}(t) (c_{23}(t) - \dot{A}(t)) - c_{22}(t) (c_{13}(t) + \dot{A}(t))}{c_{22}(t)c_{11}(t) - c_{12}(t)c_{21}(t)}, \quad (5.2.12)$$

$$\frac{db}{dt} = \frac{c_{11}(t) (c_{23}(t) - \dot{A}(t)) - c_{21}(t) (c_{13}(t) + \dot{A}(t))}{c_{21}(t)c_{12}(t) - c_{11}(t)c_{22}(t)}. \quad (5.2.13)$$

We introduce  $u(x, y, t)$  and  $v(x, y, t)$ , the horizontal and vertical velocity of the

flow respectively. The velocities are governed by the set of equations

$$\frac{\partial u}{\partial x} + \frac{\partial v}{\partial y} = 0, \quad y < 0, \quad (5.2.14)$$

$$\frac{\partial v}{\partial x} - \frac{\partial u}{\partial y} = 0, \quad y < 0, \quad (5.2.15)$$

$$v = \dot{y}_b(x, t), \quad y = 0, x \in [-b, -a] \cup [a, b], \quad (5.2.16)$$

$$u = 0, \quad y = 0, x \notin [-b, -a] \cup [a, b], \quad (5.2.17)$$

by using the conservation of mass, vorticity and boundary conditions. The combination  $u - iv$  forms a function which is analytic in the lower half plane. We will use the same method as previously used of constructing a function with  $u$  and  $v$  which has real values are known along the boundary  $y = 0$  and apply the Hilbert equation to find the velocities. Multiplying the function  $u - iv$  by  $G$  defined in (5.2.2) provides another analytic function which has real values along the boundary given by,

$$\Re(G(x, t) (u(x, t) - iv(x, t))) = \begin{cases} 0, & x \leq -b, \\ \dot{y}_b \sqrt{(b^2 - x^2)(x^2 - a^2)}, & -b \leq x \leq -a, \\ 0, & -a \leq x \leq a, \\ -\dot{y}_b \sqrt{(b^2 - x^2)(x^2 - a^2)}, & a \leq x \leq b, \\ 0, & b \leq x. \end{cases} \quad (5.2.18)$$

From here on we will take  $\dot{y}_b = -1$  to match the constant speed of impact described in the problem definition. In order to use the Hilbert equation we must again take care of the far-field behaviour of our analytic function. By definition velocity is the time derivative of displacement so,  $v = \dot{Y}$ . It follows that that  $v \approx 1/x^2$  as  $|x| \rightarrow \infty$ , while  $G \approx x^2$  as  $|x| \rightarrow \infty$  so that the combination  $G(u - iv) \rightarrow i\bar{C}$  as  $x \rightarrow \infty$ , where  $\bar{C}(t)$  is a real function. By constructing a new analytic function

$$G(x, t) (u(x, t) - iv(x, t)) - i\bar{C}(t), \quad (5.2.19)$$

we satisfy the requirements of the Hilbert equation for the function to decay in the far field and be analytic in the lower half plane. Using the Hilbert equation provides

$$\Im G(x, t) (u(x, t) - iv(x, t)) - \bar{C}(t) = \frac{2}{\pi} \int_a^b \frac{\tau \sqrt{(b^2 - x^2)(x^2 - a^2)} d\tau}{\tau^2 - x^2}. \quad (5.2.20)$$

We can find the vertical velocity away from the contact regions,

$$v(x, t) = \begin{cases} \frac{1}{\pi \sqrt{(b^2 - x^2)(a^2 - x^2)}} \left( C(t) + 2 \int_a^b \frac{\tau \sqrt{(b^2 - \tau^2)(\tau^2 - a^2)} d\tau}{\tau^2 - x^2} \right), & -a \leq x \leq a, \\ \frac{-1}{\pi \sqrt{(x^2 - b^2)(x^2 - a^2)}} \left( 2 \int_a^b \frac{\tau \sqrt{(b^2 - \tau^2)(\tau^2 - a^2)} d\tau}{\tau^2 - x^2} + C(t) \right), & b \leq x, \end{cases} \quad (5.2.21)$$

where we have introduced  $\bar{C}(t) = \pi C(t)$ . The horizontal velocity in the contact regions is given by

$$u(x, t) = \frac{-1}{\pi \sqrt{(b^2 - x^2)(x^2 - a^2)}} \left( 2 \int_a^b \frac{\tau \sqrt{(b^2 - \tau^2)(\tau^2 - a^2)} d\tau}{\tau^2 - x^2} + C(t) \right). \quad (5.2.22)$$

We now evaluate the behaviour of the vertical velocity, from equation (5.2.21), and vertical displacement, from equation (5.2.5) in the far field,  $x \rightarrow \infty$ . We find  $v \approx -C(t)/\pi x^2$  and  $Y \approx -A(t)/\pi x^2$ . By using the kinematic boundary condition

$$\frac{\partial Y}{\partial t} = v, \quad y = 0, \quad x \notin [-b - a] \cup [a, b], \quad (5.2.23)$$

we find

$$\frac{dA}{dt} = C(t). \quad (5.2.24)$$

We seek to simplify the integrals in equations (5.2.21) and (5.2.22), we consider the integral

$$\int_a^b \frac{\tau \sqrt{(b^2 - \tau^2)(\tau^2 - a^2)} d\tau}{\tau^2 - x^2}. \quad (5.2.25)$$

By making a substitution of  $\tau^2 = u$  and multiplying numerator and denominator

by the square roots we obtain

$$\int_a^b \frac{\tau \sqrt{(b^2 - \tau^2)(\tau^2 - a^2)} d\tau}{\tau^2 - x^2} = \frac{1}{2} \int_{a^2}^{b^2} \frac{(b^2 - u)(u - a^2) du}{(u - x^2) \sqrt{(b^2 - u)(u - a^2)}}. \quad (5.2.26)$$

The non-square root terms can be rewritten using

$$\frac{(b^2 - u)(u - a^2)}{u - x^2} = \left(1 + \frac{x^2 - a^2}{u - x^2}\right) (b^2 - u) = (b^2 - u - x^2 + a^2) + (x^2 - a^2) \left(\frac{b^2 - x^2}{u - x^2}\right). \quad (5.2.27)$$

We substitute (5.2.27) into the right hand integral in equation (5.2.26) and separate the resulting expression into two integrals,

$$\begin{aligned} \frac{1}{2} \int_{a^2}^{b^2} \frac{(b^2 - u)(u - a^2) du}{(u - x^2) \sqrt{(b^2 - u)(u - a^2)}} &= \frac{1}{2} \int_{a^2}^{b^2} \frac{(b^2 - u - x^2 + a^2) du}{\sqrt{(b^2 - u)(u - a^2)}} \\ &+ \frac{(x^2 - a^2)(b^2 - x^2)}{2} \int_{a^2}^{b^2} \frac{du}{(u - x^2) \sqrt{(b^2 - u)(u - a^2)}}. \end{aligned} \quad (5.2.28)$$

We let  $u = A + B\xi$  such that  $\xi = -1$  corresponds to  $u = a^2$  and  $\xi = 1$  corresponds to  $u = b^2$ . This provides  $A = (a^2 + b^2)/2$  and  $B = (b^2 - a^2)/2$ . Making this substitution transforms the right hand side of equation (5.2.28) into

$$\frac{1}{2} \int_{-1}^1 \frac{(B(1 - \xi) + (a^2 - x^2)) d\xi}{\sqrt{1 - \xi^2}} + \frac{x^2 - a^2}{2B} \int_{-1}^1 \frac{d\xi}{\left(\xi - \frac{A - x^2}{B}\right) \sqrt{1 - \xi^2}}. \quad (5.2.29)$$

We begin by considering just the regular integral on the left hand side of equation (5.2.29), direct integration provides

$$\frac{1}{2} \int_{-1}^1 \frac{B(1 - \xi) + a^2 - x^2}{\sqrt{1 - \xi^2}} d\xi = \frac{\pi}{2} \left( \frac{b^2 + a^2}{2} - x^2 \right). \quad (5.2.30)$$

For  $x \in [-b, -a] \cup [a, b]$  we have  $0 \leq \frac{A - x^2}{B} \leq 1$ . It is a standard result that for this range of  $x$  this principal value integral is zero. Then we have

$$\frac{x^2 - a^2}{2B} \int_{-1}^1 \frac{d\xi}{\left(\xi - \frac{A - x^2}{B}\right) \sqrt{1 - \xi^2}} = \frac{x^2 - a^2}{2B} \int_{-1}^1 \frac{d\xi}{\left(\xi - \frac{A - x^2}{B}\right) \sqrt{1 - \xi^2}}, \quad x \notin [-b, -a] \cup [a, b], \quad (5.2.31)$$

which we can then directly integrate to obtain

$$\frac{x^2 - a^2}{2B} \int_{-1}^1 \frac{d\xi}{\left(\xi - \frac{A-x^2}{B}\right) \sqrt{1-\xi^2}} = -\frac{\pi}{2} \sqrt{(a^2 - x^2)(b^2 - x^2)}, \quad x \notin [-b, -a] \cup [a, b]. \quad (5.2.32)$$

Using results from equations (5.2.30) and (5.2.32) together with equations (5.2.21) and (5.2.22) allows us to find horizontal velocity in the contact regions  $u$ ,

$$u(x, 0, t) = \frac{\pi \left(x^2 - \frac{b^2+a^2}{2}\right) - C(t)}{\pi \sqrt{(b^2 - x^2)(x^2 - a^2)}}, \quad a \leq x \leq b. \quad (5.2.33)$$

and the vertical velocity in the cavity,

$$v(x, 0, t) = \frac{C(t) - \pi \sqrt{(b^2 - x^2)(a^2 - x^2)} + \pi \left(\frac{b^2+a^2}{2} - x^2\right)}{\pi \sqrt{(x^2 - b^2)(x^2 - a^2)}}, \quad -a \leq x \leq a. \quad (5.2.34)$$

To set  $C(t)$  and find  $A(t)$  we use the cavity properties of pressure, velocity potential and volume. We find the time derivative of cavity volume from the integral

$$\frac{dV_c}{dt} = 2 \frac{d}{dt} \int_0^a (y_b(x, t) - \eta_b(x, t)) dx = -2 \int_0^a (1 + v(x, t)) dx, \quad (5.2.35)$$

where we used  $y_b(a, t) - \eta(a, t) = 0$  and the kinematic boundary condition. The form of equation (5.2.35) comes from our inversion from a liquid droplet impacting a flat solid substrate to a shaped solid impacting an initially flat free surface.

Substituting the vertical velocity equation (5.2.34) into (5.2.35) provides

$$\frac{dV}{dt} = - \left( \frac{2K\left(\frac{a}{b}\right)}{b} \frac{C(t) + \pi \left(\frac{b^2+a^2}{2}\right)}{\pi} - 2b \left( K\left(\frac{a}{b}\right) - E\left(\frac{a}{b}\right) \right) \right), \quad (5.2.36)$$

where  $K$  and  $E$  are complete elliptic integrals defined as

$$K(x) = \int_0^{\frac{\pi}{2}} \frac{d\theta}{\sqrt{1 - x^2 \sin^2(\theta)}}, \quad (5.2.37)$$

and

$$E(x) = \int_0^{\frac{\pi}{2}} \sqrt{1 - x^2 \sin^2(\theta)} d\theta, \quad (5.2.38)$$

respectively. By using the definition of the velocity potential,  $u(x, t)\partial\varphi/\partial x$ , and integrating across the contact region  $[a, b]$  we find

$$\int_a^b u(x, t) dx = -\varphi(a, t) = -\varphi_c(t), \quad (5.2.39)$$

where  $\varphi_c(t)$  is the velocity potential of in the cavity and is linked to the pressure in the cavity through the non-dimensional Bernoulli equation,

$$p_c(t) = -\dot{\varphi}_c(t). \quad (5.2.40)$$

Substituting the horizontal velocity (5.2.33) into equation (5.2.39) provides

$$-\varphi_c(t) = bE\left(\frac{\sqrt{b^2 - a^2}}{b}\right) - K\left(\frac{\sqrt{b^2 - a^2}}{b}\right)\left(\frac{\frac{\pi}{2}(b^2 + a^2) + C(t)}{b\pi}\right), \quad (5.2.41)$$

which is rearranged for  $C(t)$

$$C(t) = -\frac{\pi b}{K\left(\frac{\sqrt{b^2 - a^2}}{b}\right)}\left(bE\left(\frac{\sqrt{b^2 - a^2}}{b}\right) + \varphi_c(t)\right) - \frac{\pi}{2}(b^2 + a^2). \quad (5.2.42)$$

We then have a set of coupled ordinary differential equations to be solved;

$$\frac{da}{dt} = \frac{c_{12}(t) \left( c_{23}(t) - \dot{A}(t) \right) - c_{22}(t) \left( c_{13}(t) + \dot{A}(t) \right)}{c_{22}(t)c_{11}(t) - c_{12}(t)c_{21}(t)}, \quad (5.2.43)$$

$$\frac{db}{dt} = \frac{c_{11}(t) \left( c_{23}(t) - \dot{A}(t) \right) - c_{21}(t) \left( c_{13}(t) + \dot{A}(t) \right)}{c_{21}(t)c_{12}(t) - c_{11}(t)c_{22}(t)}, \quad (5.2.44)$$

$$\frac{dA}{dt} = C(t), \quad (5.2.45)$$

$$\frac{dV_c}{dt} = - \left( \frac{2K \left( \frac{a}{b} \right) C(t) + \pi \left( \frac{b^2+a^2}{2} \right)}{b} - 2b \left( K \left( \frac{a}{b} \right) - E \left( \frac{a}{b} \right) \right) \right), \quad (5.2.46)$$

$$\frac{d\varphi_c(t)}{dt} = -p_c(t), \quad (5.2.47)$$

$$p_c(t) = C_0 V_c^{-\gamma}, \quad (5.2.48)$$

$$C(t) = - \frac{\pi b}{K \left( \frac{\sqrt{b^2-a^2}}{b} \right)} \left( bE \left( \frac{\sqrt{b^2-a^2}}{b} \right) + \varphi_c(t) \right) - \frac{\pi}{2} (b^2 + a^2), \quad (5.2.49)$$

together with initial conditions

$$a = b = 1, \quad V_c = \int_{-1}^1 f(x) dx, \quad A = 0, \quad C = 0, \quad \varphi = 0, \quad t = 0. \quad (5.2.50)$$

### 5.2.1 Numerical Solution

We solve the set of ordinary differential equations (5.2.43)-(5.2.49) using the Runge-Kutta Fourth order method. It is difficult to start the numerical scheme from time  $t = 0$  using time as the independent variable due to the time derivatives of the contact line positions being undefined. Instead we rewrite the problem with

$a(t)$ , the inner contact line position, as the independent variable.

$$\frac{dt}{da} = \frac{c_{22}(t)c_{11}(t) - c_{12}(t)c_{21}(t)}{c_{12}(t)(c_{23}(t) - \dot{A}(t)) - c_{22}(t)(c_{13}(t) + \dot{A}(t))}, \quad (5.2.51)$$

$$\frac{db}{da} = \frac{c_{21}(t)(c_{13}(t) + \dot{A}(t)) - c_{11}(t)(c_{23}(t) - \dot{A}(t))}{c_{12}(t)(c_{23}(t) - \dot{A}(t)) - c_{22}(t)(c_{13}(t) + \dot{A}(t))}, \quad (5.2.52)$$

$$\frac{dA}{da} = \frac{dt}{da} C(t), \quad (5.2.53)$$

$$\frac{dV_c}{da} = -\frac{dt}{da} \left( \frac{2K\left(\frac{a}{b}\right)C(t) + \pi\left(\frac{b^2+a^2}{2}\right)}{b\pi} - 2b\left(K\left(\frac{a}{b}\right) - E\left(\frac{a}{b}\right)\right) \right), \quad (5.2.54)$$

$$\frac{d\varphi_c(t)}{da} = -\frac{dt}{da} p_c(t). \quad (5.2.55)$$

Doing this allows us to bypass the unbounded velocity in our numerics by forcing the contact line position to move and updating time  $t$  to match this movement. Since  $\dot{a}$  is unbounded at time  $t = 0$  we have  $dA/da = 0$ ,  $dV_c/da = 0$ ,  $d\varphi_c/da = 0$  initially. However,  $\dot{b}$  is also unbounded at time  $t = 0$  so we must investigate the very initial moments of impact to find  $db/da$  in order to act as an initial condition for our numerics. In the Wagner impact problems discussed in previous chapters this was not needed. Here it is needed because of the presence of the cavity, which provides two pairs of different contact points, that causes this additional complexity. At initial times the two contact regions will not affect each other, so we consider the behaviour local to one impact point only and for simplicity move this contact point to the origin. If we have the location of the solid substrate given by

$$y_b(x, t) = f(x) - t, \quad f(x) = f(-x), \quad (5.2.56)$$

then as shown in [Korobkin \[1982\]](#) the Wagner condition for a body of the form (5.2.56) is given by

$$\int_0^{\frac{\pi}{2}} y_b(c(t) \sin(\theta), t) d\theta = 0, \quad (5.2.57)$$

where  $c(t)$  is the position of the symmetric contact line. For example, for  $f_1(x) = x^4/2$  and  $f_2(x) = x^2/2$  (5.2.56) provides  $c_1(t) = \left(\frac{16t}{3}\right)^{\frac{1}{4}}$  and  $c_2(t) = 2\sqrt{t}$

respectively.

$$y_b(x, t) = \begin{cases} f_1(x, t) - t, & x < 0, \\ f_2(x, t) - t, & x > 0. \end{cases} \quad (5.2.58)$$

Where in this local model we would identify  $c_1(t)$  as  $1 + a(t)$  and  $c_2(t)$  as  $1 + b(t)$ . Given we are interested in the ratio of velocities, that is  $db/da = dc_2/dc_1$ , only at time  $t = 0$  we assume that each contact moves as it would do if the free surface were of the form in equation (5.2.56). For example for  $f_1 = x^4/2$  and  $f_2 = x^2/2$  we assume  $c_1(t) = (\frac{16t}{3})^{\frac{1}{4}}$  and  $c_2(t) = 2\sqrt{t}$  at time  $t = 0$ . Then we have  $db/da = dc_2/dc_1 \approx t^{\frac{1}{4}} = 0$  at time  $t = 0$ . So, if the free surface inside the cavity is of a different order in  $x$  to that outside we have a simple initial condition for our numerics. However, if the free surface is the same order on each side of the contact points we must be more careful and provide a detailed local analysis of the motion of the two contact points. If the free surface, local to the touchdown points, has the same behaviour from the left and the right we can set  $da/db = -1$  initially.

We will be considering two initial solid substrate shapes, the simplest shape we use is that discussed above,

$$f(x) = \frac{(x^2 - 1)^2}{8}, \quad (5.2.59)$$

which provides a simple case to investigate the underlying mechanics of the presence of air. We then investigate an initial free surface shape of

$$f(x) = \begin{cases} \frac{(x^2-1)^2}{8}, & |x| < 1, \\ \frac{(x-1)^2}{2}, & |x| > 1. \end{cases} \quad (5.2.60)$$

This provides us with a more representative problem to solve, since the free surface in the far field in equation (5.2.60) tends to  $x^2/2$  as required to make the link to a droplet, unlike that in equation (5.2.59). From the above discussion on initial conditions and the two free surface shapes in equations (5.2.59)-(5.2.60)

we have initial conditions of

$$a(0) = b(0) = 1, \quad \frac{db}{da} = -1, \quad A(0) = 0, \quad C(0) = 0, \quad (5.2.61)$$

$$V_c = \frac{2}{15}, \quad p(0) = C_0 V_c^{-\gamma}, \quad (5.2.62)$$

which are used to start the solution of the system of equations (5.2.51)-(5.2.55). However, as time  $t$  increases the inner contact line velocity  $\frac{da}{dt}$  begins to reduce towards zero. As the inner contact line velocity becomes small it affects our numerics negatively, and as such once  $da/dt > -1$  we change from using  $a$  as the independent variable to time  $t$  such that the system of equations being solved changes to the system of equations (5.2.43)-(5.2.49). The numerics terminate if any of the conditions

$$\frac{da}{dt} = 0, \quad \frac{db}{dt} = 0, \quad \left| \frac{da}{dt} \right| \rightarrow \infty, \quad \left| \frac{db}{dt} \right| \rightarrow \infty, \quad (5.2.63)$$

occur due to assumptions within the Wagner model. However, within this model we do not expect to encounter large velocities in the outer contact points,  $\left| \frac{db}{dt} \right| \rightarrow \infty$ , since the shape of the impacting free surface does not become parallel to the solid substrate other than at the initial touchdown points. However, as  $a \rightarrow 0$  since the free surface shapes we use become flat  $da/dt$  can become very large. Similarly there is no mechanism to cause  $db/dt = 0$  and as such it is only  $da/dt = 0$  and  $a \rightarrow 0$  that causes our model to break down for the chosen substrate shapes which requires stopping the numerics.

### 5.3 Results

We begin analysis of the results by investigating the impact behaviour if there were no gas in the cavity. For this we set  $\varphi_c(t) = 0$  in equation (5.2.49) and remove the three equations linking the cavity volume, pressure and velocity potential,

leaving us to solve the system of equations

$$\frac{dt}{da} = \frac{c_{22}(t)c_{11}(t) - c_{12}(t)c_{21}(t)}{c_{12}(t)(c_{23}(t) - C(t)) - c_{22}(t)(c_{13}(t) + C(t))}, \quad (5.3.1)$$

$$\frac{db}{da} = \frac{c_{21}(t)(c_{13}(t) + \dot{A}(t)) - c_{11}(t)(c_{23}(t) - \dot{A}(t))}{c_{12}(t)(c_{23}(t) - \dot{A}(t)) - c_{22}(t)(c_{13}(t) + \dot{A}(t))}, \quad (5.3.2)$$

$$C(t) = -\frac{\pi b}{K\left(\frac{\sqrt{b^2 - a^2}}{b}\right)} \left( bE\left(\frac{\sqrt{b^2 - a^2}}{b}\right) \right) - \frac{\pi}{2}(b^2 + a^2), \quad (5.3.3)$$

subject to initial conditions

$$a(0) = 1, \quad b(0) = 1, \quad \frac{db(0)}{da} = -1, \quad C(0) = 0, \quad (5.3.4)$$

initially, and change to solving

$$\frac{da}{dt} = \frac{c_{12}(t)(c_{23}(t) - C(t)) - c_{22}(t)(c_{13}(t) + C(t))}{c_{22}(t)c_{11}(t) - c_{12}(t)c_{21}(t)}, \quad (5.3.5)$$

$$\frac{db}{dt} = \frac{c_{11}(t)(c_{23}(t) - C(t)) - c_{21}(t)(c_{13}(t) + C(t))}{c_{21}(t)c_{12}(t) - c_{11}(t)c_{22}(t)}, \quad (5.3.6)$$

$$C(t) = -\frac{\pi b}{K\left(\frac{\sqrt{b^2 - a^2}}{b}\right)} \left( bE\left(\frac{\sqrt{b^2 - a^2}}{b}\right) \right) - \frac{\pi}{2}(b^2 + a^2), \quad (5.3.7)$$

as  $\dot{a} < -1$ .

In Figures 5.3.1 and 5.3.2 we show the behaviour of the contact points found by solving system of equations (5.3.5)-(5.3.3) subject to the initial shapes (5.2.59) and (5.2.60), respectively. In both solutions we see that as  $a$  comes close to 0 its speed increases rapidly. This comes from considering the shape of the incoming solid substrate  $f(x) = (x^2 - 1)^2/8.0$  close to the origin. Here the substrate becomes close to parallel to the initially flat liquid free surface, which causes this increase in wetting speed. This is the same mechanism that caused extremely high contact line speeds in the earlier sections on droplet impact with an elastic substrate. The behaviour of  $a(t)$  seen in Figures 5.3.1 and 5.3.2 hints at an interesting possibility in the motion of  $a(t)$  once the gas is included. As  $a(t)$  becomes small so does the volume of the cavity, which causes the pressure of the

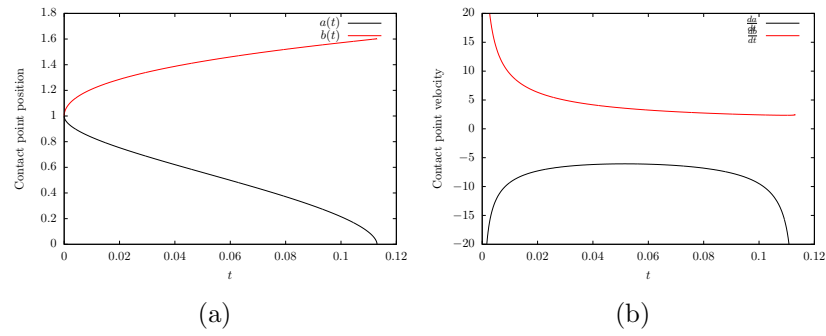


Figure 5.3.1: The contact point positions (a) and contact point velocities (b) for the substrate surface shape given in equation (5.2.59) and with no gas in the cavity.

cavity to become extremely large. This high pressure in turn acts to slow the movement of the contact point down, as the flattening of the free surface is acting to speed it up.

As expected the external contact point  $b(t)$  moves faster in Figure 5.3.2 than in Figure 5.3.1, however this is not the only difference between the results generated from the pair of solid substrate shapes. In Figure 5.3.3 we show the difference in inner contact line motion,  $a(t)$ , caused by different solid shapes for  $|x| > 1$ . As we can see the motion of  $a(t)$  is dominated by the shape of the solid inside the cavity. In reality the shape of the cavity is determined by the air cushioning process, detailed in chapter 4. This indicates that the motion of the inner contact point after impact may be governed in large part by the influence of the air before touch down. Figures 5.3.3 and 5.3.1 also indicate that when using the Wagner model for the impact of an asymmetric shaped liquid with a solid substrate splitting the free surface into multiple parts and solving them separately could be adequate as the two parts of the free surface only have a small effect on each other under some circumstances.

In Figure 5.3.4 we show the contact point position and velocity together with the cavity pressure and volume. The incoming solid shape is the same as that in Figure 5.3.1 but we have included the gas compressibility by setting  $C_0 = 1$ . We can immediately see the effect of the trapped gas on the behaviour of the inner contact point  $a(t)$ . In contrast to the no gas result in Figure 5.3.1 the

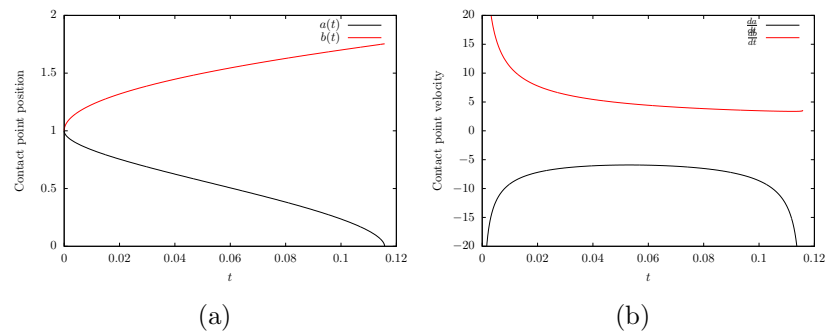


Figure 5.3.2: The contact point positions (a) and contact point velocities (b) for the substrate shape given in equation (5.2.60) and with no gas in the cavity.

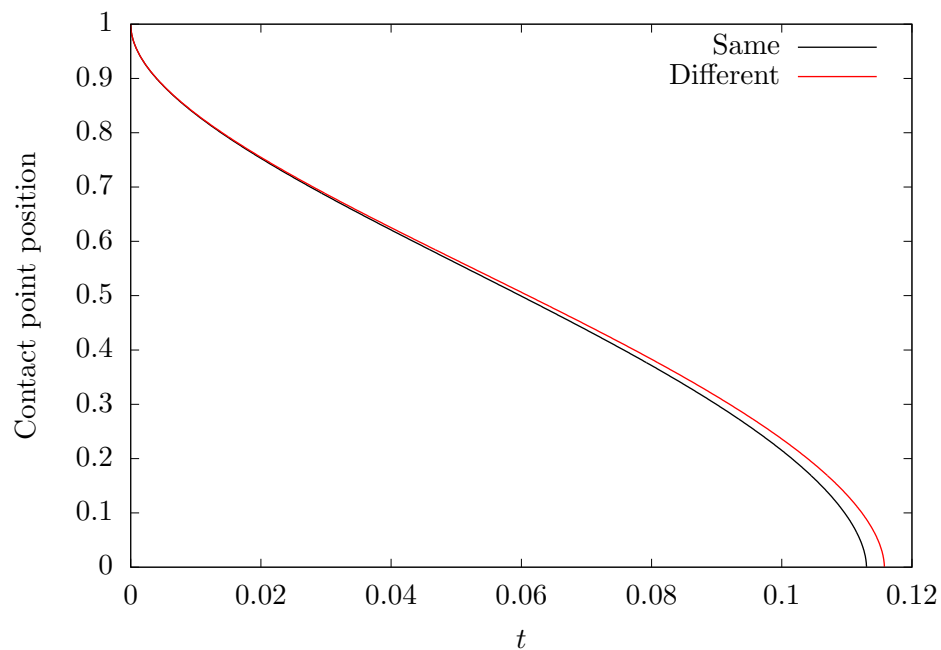


Figure 5.3.3: A comparison of the evolution of  $a(t)$  between the free surface shape being the same on either side of the contact line, (5.2.59), and different on either side of the contact line, (5.2.60)

inner contact point reaches zero velocity, at which point we have to stop our numerics due to the Wagner theory breaking down. In Figure 5.3.5 we show the contact point positions for  $C_0 = 0.1$  and  $C_0 = 2$ . As expected, with a less compressible gas (higher  $C_0$ ) we see the deceleration of the inner contact point occurring much quicker, and with the lower  $C_0$  it happens much more slowly. In Figure 5.3.6 we show the motion of the outer contact point for a range of  $C_0$ , including  $C_0 = 0$  from Figure 5.3.1. We see that as the inner contact line slows down (as we approach the end of each of the coloured lines) the outer contact

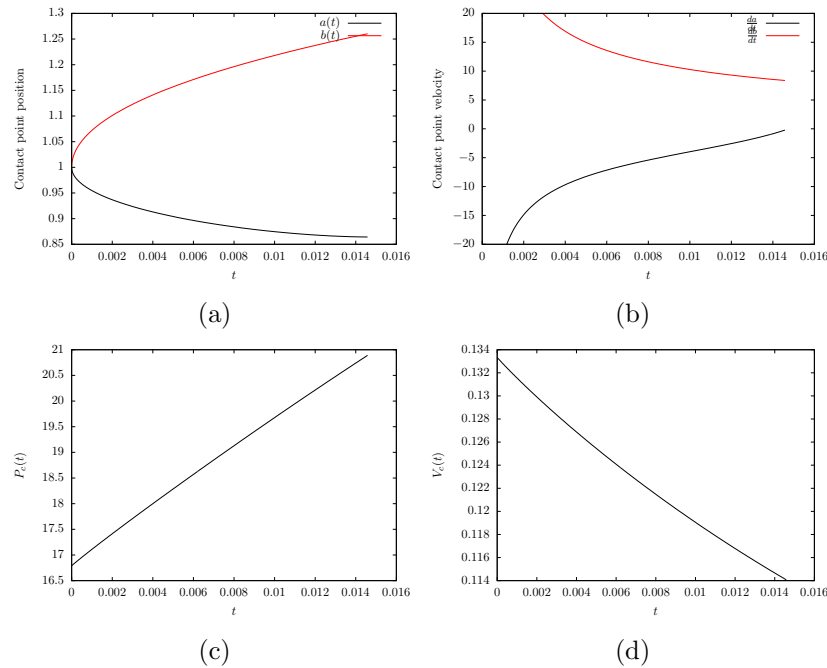
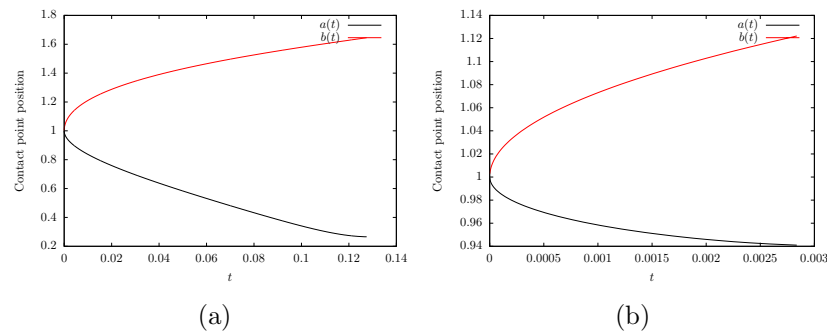
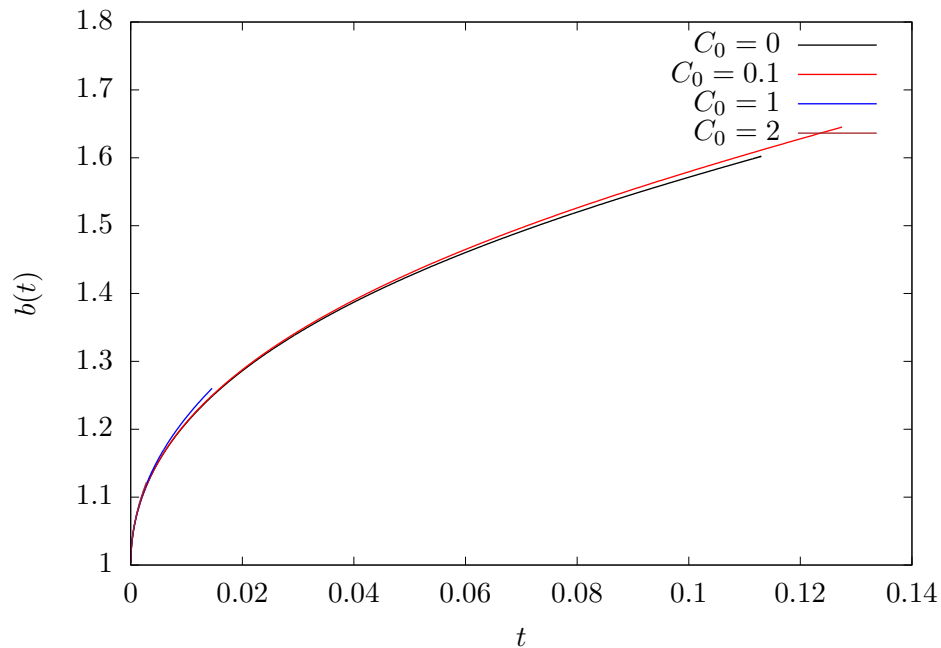


Figure 5.3.4: The contact point position (a), contact point velocity (b), pressure in the cavity (c) and volume of the cavity (d) for the solid substrate shape given in equation (5.2.59) with  $C_0 = 1$ .

point gains speed relative to the result with no gas. This happens because fluid which would flow with the contact point if there were no gas cannot do so due to the cavity pressure so to balance this extra mass out the outer contact point speed has to increase.

Although our model cannot formally continue once one of the contact points has stopped moving we can still discuss possible mechanics of the following stages. One possibility is that the acceleration of the contact point  $a(t)$  continues, with it becoming positive and the cavity starting to expand laterally. Vertically the solid substrate would continue to move down at a constant speed. This could then cause the contact point to be pinched off, trapping a small cavity of air behind the new contact point. Another possibility is that the gas has become as compressed as possible and the appropriate model is to model it as a solid structure. Finally, it is likely that beyond the limits of the Wagner model the air cavity becomes unstable in some way. Since the solid surface continues to compress the cavity the pressure in it will rise even further. Eventually the pressure will be so high

Figure 5.3.5: The contact line positions for  $C_0 = 0.1$  (a) and  $C_0 = 2$  (b)Figure 5.3.6: Comparing the motion of  $b(t)$  for a range of  $C_0$ .

that the liquid free surface becomes unstable and the gas will become a liquid-air mixture, rather than pure gas. At this point we would need to change the model of the gas cavity to include a features such a new speed of sound and compressibility for example.

In Figures 5.3.7-5.3.9 we show the contact points behaviour and cavity volume for a range of  $C_0$  using the free surface shape from equation (5.2.60) which has a different shape outside the cavity region to inside. As we can see by comparing Figures 5.3.4-5.3.5 and 5.3.7-5.3.9 the features are both quantitatively and qualitatively very similar, with the inner contact point

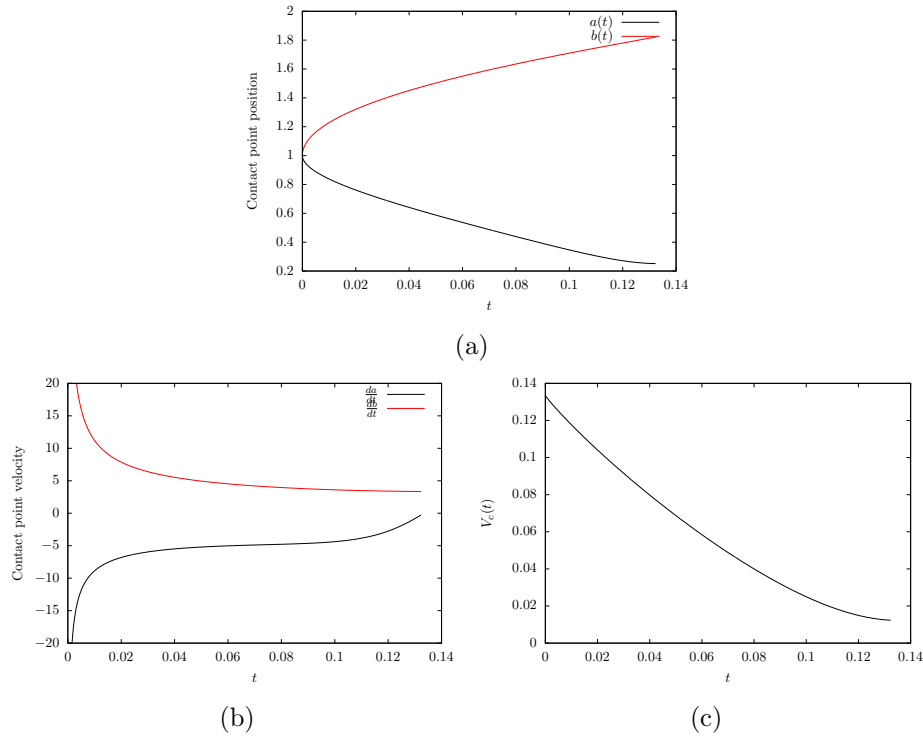


Figure 5.3.7: The contact line position (a), contact line velocity (b) and cavity volume (c) for the free surface shape given in equation (5.2.60) and  $C_0 = 0.1$ .

slowing down at a rate depending on the compressibility of the gas and eventually stopping. The largest difference for example is found by comparing the time at which the inner contact point stopped moving for  $C_0 = 0.1$ . In Figure 5.3.5a  $a(t) = 0$  at  $t = 0.0128$  versus  $a(t) = 0$  and  $t = 0.0153$  in Figure 5.3.8. We find a similar discrepancy with  $C_0 = 0.1$  and 2.0. For  $C_0 = 0.1$  the final times were 0.132 and 0.127 while for  $C_0 = 2.0$  the times were 0.00287 and 0.00281. In all cases the quadratic outer surface shape prolonged the time until the inner contact point stopped. Because the outer contact point moves faster with the quadratic than quartic solid shape at any given time the contact regions  $b(t) - a(t)$  are larger for the quadratic shape. Because of this the pressure in the cavity has more fluid to work against in order to slow the motion of the inner contact point  $a(t)$  which requires a higher pressure thus a smaller volume which takes more time to generate.

In Figure 5.3.10 we show parametric results for  $a(t_f)$ ,  $b(t_f)$ ,  $t_f$  and  $V_c(t_f)$  where  $t_f$  is the final time before  $a(t) = 0$ . The Figures show both free surfaces defined

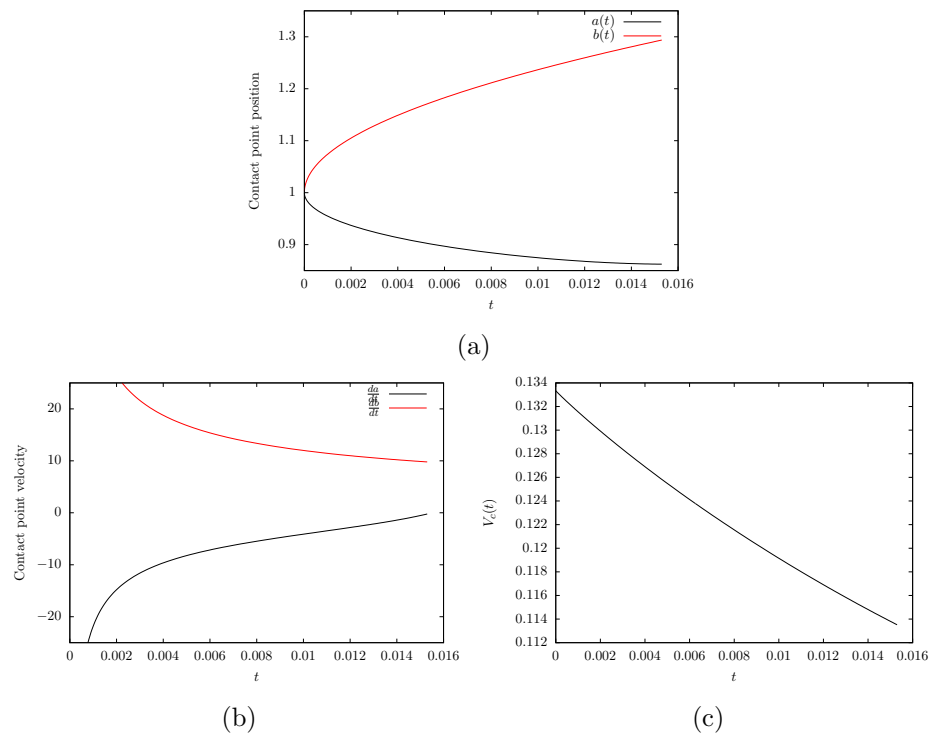


Figure 5.3.8: The contact line position (a), contact line velocity (b) and cavity volume (c) for the free surface shape given in equation (5.2.60) and  $C_0 = 1$ .

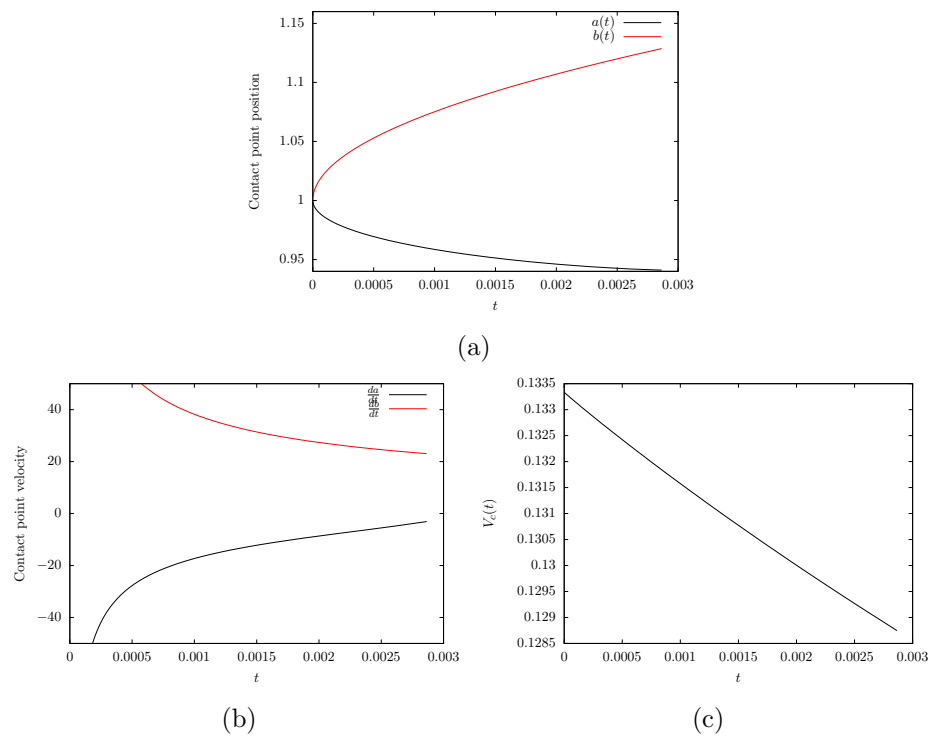


Figure 5.3.9: The contact line position (a), contact line velocity (b) and cavity volume (c) for the free surface shape given in equation (5.2.60) and  $C_0 = 0.1$ .

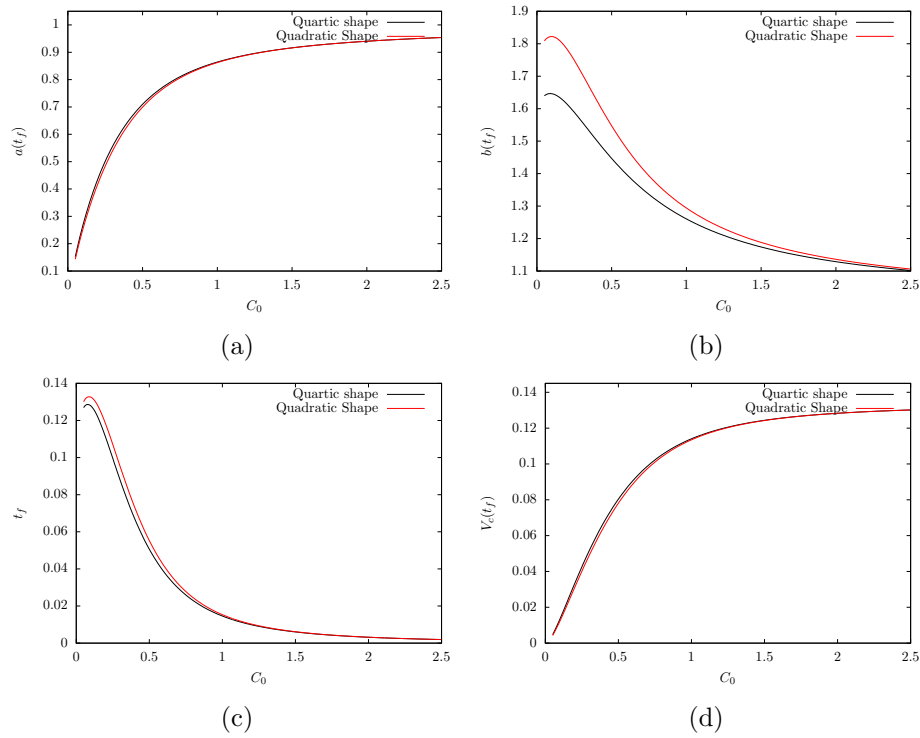


Figure 5.3.10: Parametric plots showing the inner contact line position (a), outer contact line position (b), time (c) and cavity volume (d) at the final iteration time  $t = t_f$ . for both the purely quartic incoming solid shape in equation 5.2.59 and the mixed quartic quadratic shape from equation 5.2.60

by the mixed quartic quadratic equations (5.2.59) and (5.2.60).

As we discussed previously it is expected that the cavity will become unstable at some point beyond the limits of the Wagner model. Experiments have shown that capillary waves can be generated along the cavity free surface during impact of a liquid with trapped air cavity. Here we investigate the stability of our solution by placing a small disturbance in the solid surface shape. We do this by taking the free surface shapes defined in (5.2.59) and (5.2.60) and adding a disturbance. We place this disturbance away from the initial contact point  $x = 1$  and have its amplitude be small relative to the solid surface height. We do this by adding

$$D \left( 1 + \cos \left( \frac{k\pi}{l} (x - x_0) \right) \right), \quad x_0 - l \geq x \geq x_0 + l. \quad (5.3.8)$$

Where  $D > 0$  is the amplitude,  $k$  the frequency and required to be an odd integer so that the derivative at the edges is zero,  $2l$  the length over which we apply the

disturbance and  $x_0$  is the central point the disturbance. We require that the amplitude is small  $D \ll 1$ , that the disturbance is not near the initial impact point  $x_0 + l < 1$ , and that it is not crossing the origin  $x_0 - l > 0$ . As such we investigate a solid shape defined by

$$y = \begin{cases} \frac{(x^2-1)^2}{8} - t, & 0 \leq |x| \leq x_0 - l, \\ \frac{(x^2-1)^2}{8} - t + D \left(1 + \cos\left(\frac{k\pi}{l}(x - x_0)\right)\right), & x_0 - l \leq |x| \leq x_0 + l, \\ \frac{(x^2-1)^2}{8} - t, & x_0 + l \leq |x|, \end{cases} \quad (5.3.9)$$

Note that for the solid shapes in equations (5.3.9) the initial condition on the volume changes from  $V_c = 2/15$  to  $V_c = 2/15 - 2Dl$  for odd integer  $k$ .

In Figure 5.3.11a we compare the motion of the contact points between an unperturbed solid shape and one with parameters  $D = 0.005, k = 1, l = 0.2, x_0 = 0.5$ . We can see that the motion of the outer contact point is largely unchanged by the perturbation, but the motion of the inner contact point  $a(t)$  is affected greatly. After the perturbation is encountered at  $a(t) = 0.7$  we see its influence almost immediately. The contact line slows down relative to the unperturbed motion and even stops sooner. In Figure 5.3.11b we plot the difference in the two contact line positions divided by the amplitude of the perturbation  $D = 0.005$ . Since this plot is neither small nor stable in time it indicates that the motion of the inner contact line is sensitive to a small perturbation to initial solid shape. We see this effect across a range of parameters, for example in Figure 5.3.12 and conclude that indeed the motion of the contact line is sensitive to small perturbations in the shape of the solid impactor.

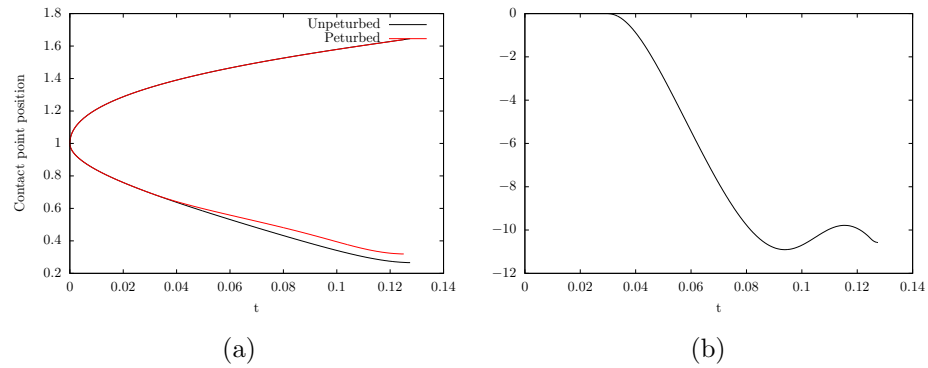


Figure 5.3.11: Figure (a) shows the contact line positions against time for an unperturbed free surface (5.2.59) and a perturbed free surface (5.3.9) with parameters  $D = 0.00$ ,  $k = 1$ ,  $l = 0.2$ ,  $x_0 = 0.7$ . Figure (b) shows the difference between perturbed and unperturbed inner contact line positions  $a(t)$  divided by the amplitude of the perturbation  $D = 0.005$  against time. The compressibility coefficient was set to  $C_0 = 0.1$

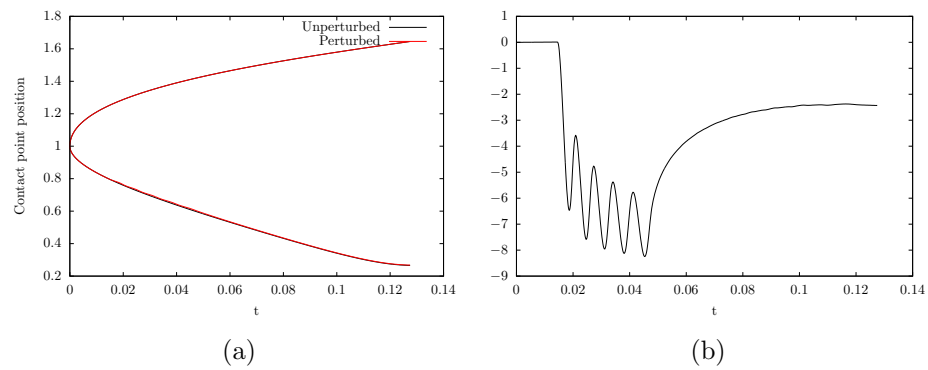


Figure 5.3.12: Figure (a) shows the contact line positions against time for an unperturbed free surface (5.2.59) and a perturbed free surface (5.3.9) with parameters  $D = 0.0008$ ,  $k = 5$ ,  $l = 0.1$ ,  $x_0 = 0.5$ . Figure (b) shows the difference between perturbed and unperturbed inner contact line positions  $a(t)$  divided by the amplitude of the perturbation  $D = 0.0008$  against time. The compressibility coefficient was set to  $C_0 = 0.1$

## Conclusions and future work

---

### 6.1 Conclusions

In chapters 2 and 3 a model of droplet impact onto an elastic plate was presented. The model generalises the Wagner theory of water impact to axisymmetric configurations and elastic surface of the body. The uniformly valid description of the resulting flow was obtained using the asymptotic approach by [Howison et al. \[1991\]](#). The flow region was divided into three sub-regions: the main flow region with its size of order of the elastic plate diameter, the small jet-root region at the periphery of the wetted part of the substrate, and the jet region where splashing can be observed. The pressure and velocity field of the main flow region are singular at the contact line, necessitating the formation of an asymptotic jet-root close to the contact line. In order to conserve mass, a liquid jet emanates from the jet-root region in a direction normal to the contact line. It was shown that the vibrating substrate does not directly interact with the jet-root region at leading order, only providing a contribution to the jet parameters through the far field condition.

The leading-order solutions in each sub-domain of the flow region were obtained and matched to each other. The flow in the main flow region was coupled with the plate vibration caused by impact. It was shown that the radius of the contact region is strongly dependent on the deflection of the elastic substrate. The jet flow is smooth and finite only if the acceleration of the contact line is negative,

as it is for a rigid substrate. Elasticity of the substrate may change the sign of the contact line acceleration if the substrate starts to oscillate during the early impact stage. This can occur only for the finite elastic substrate with a relatively small period of natural vibration. It was shown that a positive acceleration of the contact line leads to blowing-up of the jet flow with formation of the secondary torus jet in the direction normal to the surface of the substrate. The formation of this secondary jet is treated in the present model as splashing. Conditions of the splashing were derived in terms of the parameters of impact and characteristics of the substrate,  $\alpha$  and  $\beta$ . A graphical way to predict the time and location at which splashing will first be seen was discussed and presented. The evolution of the jet thickness from a small bump to a large splash was shown against Eulerian and Lagrangian variables. Finally a parametric analysis of the values of  $\alpha$  and  $\beta$  for which splashing is predicted was performed. It was found that there is a large range of  $\alpha$  and  $\beta$  for which splashing occurs for both a clamped and simply supported elastic plate, although with the simply supported elastic plate having a large region where splashing is predicted..

The Wagner model requires that during the impact the contact line velocity is positive and finite. We obtained the range of the non-dimensional elastic parameters  $\alpha$  and  $\beta$  for which the Wagner model is valid. Mechanisms behind the unbounded contact line velocity and contact line shrinking were investigated and both tied directly to behaviour of the elastic plate. These critical regimes of a droplet impact are related to the early stage when the elastic plate is partly wetted. It was shown that the elastic effects decay quickly after the elastic plate is wetted completely and the contact region continues to expand along the rigid part of the substrate.

We have shown that the presence of an elastic plate can cause splashing in absence of interaction with surrounding gas or substrate roughness. However, the roles of the liquid surface tension and viscosity in the formation or suppression of the splash are still unclear. Vibrations of the elastic plate can cause cavitation which can be responsible for damage to the substrate. The present model does

not allow us to control the distribution of the hydrodynamic pressure near the contact region and its evolution in time. This is due to the very slow convergence of the series for the pressure in terms of the normal modes of the elastic plate, see discussion of this problem by Korobkin [1998]. In these chapters we assumed axisymmetry of the flow. It is interesting to investigate how much a fully three dimensional situation would change the dynamics of spreading and splashing. The three-dimensionality of the flow and elastic response can be achieved by moving the impact point away from the centre of the plate, or by considering the impact of an ellipsoidal liquid droplet.

In chapter 4 we develop a model of a droplet approaching an elastic plate while being affected by air cushioning. The deformation of both the droplet free surface and elastic plate were coupled through the gas pressure in a complex non-linear way. The model considers a asymptotically short time before touch down in which the gas pressure becomes high enough to overcome the difference in liquid and gas densities to cause deflections in the liquid free surface and solid substrate. Appropriate non-dimensional scales were derived, indicating that in order for the elastic plate to be deflected on the same scale as the liquid free surface the plate must be very flexible. Examples of this included extremely thin plates as well as foils. By finding the horizontal velocity of the gas in terms of the free surface height and plate displacement we derived the first governing equation from the gas continuity equation. The second governing equation was found by using complex analysis on an analytic function generated from the liquid vertical velocity and pressure with the final governing equation given directly from the plate equation. This set of governing equations was solved using a system of numeric methods. We used the boundary element method to solve two of the governing equations and the method of normal modes to solve the plate equation. Due to the coupled non-linear nature of the set of governing equations at each time step a convergent solution must be iterated upon.

As the thickness of the gas layer becomes small this becomes increasingly difficult, to the point that a convergent solution cannot be found any more.

Once this happens we must stop our simulation. By increasing the resolution of our numerics we can reduce the gap thickness at which this happens, but we can never get to the point of touch down within our numerics. In order to analyse this region we investigated a small asymptotic region close to the touch down point and showed that the presence of the elastic plate does not cause any local changes to the touch down behaviour described by [Smith et al. \[2003\]](#).

We investigated two distinct situations, one where the droplet is centred on the elastic plate and one where it was not. When centred we have shown that the presence of the elastic plate universally slows the time of touch down, traps a bigger volume of gas upon touch down and has a lower pressure in the gas relative to having a rigid substrate. This is caused by the pressure acting on two deformable surfaces, rather than just the deformable free surface. Once the plate is set in motion the gap bubble closes more slowly, leading to a slower build up of pressure which causes the delay in touch down and the trapping of a larger volume of gas. Touch down typically occurs at or near the edge of the elastic plate, as here the effects of the elastic plate on reducing gas pressure and slowing the approach of the free surface to the substrate are lessened.

When the droplet is not centred on the elastic plate an element of asymmetry has been introduced which creates many interesting phenomena. We find that touch down occurs at only one point, instead of two like in the centralised impact. We demonstrated that close to this touch down point the pressure is very high, but with a generally lower pressure across the rest of the gas relative to having the plate be centralised. These effects reach a maximum for some location of the plate and then decay as the plate is moved far enough away to influence the droplet minimally. By analysing the flux we showed that this is caused by the one touch down point forcing gas out under what would have been the other touch down point if the plate were centralised, which requires a higher pressure at the touch down point and causes more flow in the gas, thus reducing its pressure.

Throughout chapter 4 we neglected the influence of gas compressibility and

thermal effects, liquid surface tension and restricted ourself to 2D. Work has been performed in the past on including these physical factors and modelling a 3d air cushion but would still interesting to see how the change from 2D-3D2 especially would change the mechanisms we see. Although the touch down asymptotic tell us that touch down does occur in a finite time it does not give us many details we can use to continue to post impact, investigating this transition from air cushioning to liquid impact problem is of great interest for the future, with potential solutions being found by including kinetic effects of the gas and other statistical physics models.

In chapter 5 we introduce a model for the impact of a liquid droplet with an attached cavity filled with gas. By using the scales and results from chapter 4 we showed that there exists a regime in which the gas cavity is at the same scale as the Wagner vertical scale. This is key as it allows us to create a model in which the gas and liquid behaviours are coupled. We introduced the Wagner model with an attached cavity which was solved using a variety of complex analysis tools, eventually leaving us with a system of ordinary differential equations to solve for the two contact point locations and various cavity properties. This set of equations was solved numerically, however initialising the numerical simulation is not trivial. As we discussed since the contact point velocities are unbounded initially we cannot use time as an independent variable. When we encountered this issue in chapters 2 and 3 we resolved it by changing independent variable to the contact line position. However since there are two pairs of independent contact points in chapter 5 this is not trivial as we must determine their relative velocities. If the shape of the impactor near the initial contact point is symmetric we can set the contact points relative velocity to -1 and begin our numerics. In other situations however it is far more complicated and is a very important area for future work.

We have shown that as the gas cavity is compressed its pressure rises to the point of stopping the motion of one pair of contact points. Due to the limitations of the Wager model we must stop our simulation at this time, however it is of great

interest what happens just after this point. It is unclear if the inner contact points become in effect pinned, begin expanding or if the cavity becomes unstable. We showed that the motion of the inner contact point is sensitive to small changes in impactor geometry. If the cavity does become unstable it is possible that the trapped gas turns into a mixture of gas and liquid which has a different compressibility and speed of sound to a pure gas cavity. From here compression could continue. In experiments by [Thoroddsen et al. \[2005\]](#) small gas bubbles were left behind the motion of the inner contact point, it is possible this happens after the inner contact point stops moving in our simulations. Although the gas cavity pressure has grown high enough to stop the motion of the contact point this does not stop the motion of the solid impactor which could pinch off small sections of the cavity close to the static contact point. In order to investigate these possibilities a more complicated model for the gas will be required which includes the flow and thermal dynamics of the gas. This is a highlight non-trivial inclusion in the model whose effects are not immediately obvious. Performing full direct numerical simulations will be an invaluable tool in investigating the role of surface tension, viscosity, more complex gas dynamics and in the transition from air cushioning to impact problem and can be used to inform our asymptotic models.

## 6.2 Future Work

There are a number of interesting and important areas for further research following the work within this thesis. Of particular interest to the author is an investigation of the splashing result shown in chapters 2 and 3. This result runs counter to the currently published experimental results by [Pepper et al. \[2008\]](#). The published experimental works all operate on a different time scale to the problems considered in chapters 2 and 3, as such having an experimental investigation of the shorter timescale we used would be interesting. It is possible that splashing will not be seen in this regime due to effects like surface

tension or viscosity in the jet-region. Here, as in all work the author is aware of, these effects are taken to be higher order corrections but finding the exact influence they have is interesting. This could be done either with asymptotic modelling or possibly more reasonably with direct numerical simulation.

Another area of future work is on the touch down process itself. The transition from pre-impact air cushioning to impact mechanics is extremely complicated and an area which could contain a large amount of interesting mathematics and physics. Particularly it is plausible that continuum models are not sufficient to model this process and instead statistical physics or molecular dynamics approaches would be necessary. Results from this type of analysis could help inform extensions to the model of droplet impact with an attached air cavity introduced in chapter 5 by providing more accurate initial conditions. Other extensions to that model are a more complicated and potentially physically relevant model of the gas, the free surface near the touchdown points taking more wedge like shape and including surface tension with particular interest in any capillary waves generated on the free surface of the trapped bubble and their impact on the stability of the model.

# Bibliography

---

- A. Alizadeh, V. Bahadur, W. Shang, Y. Zhu, D. Buckley, A. Dhinojwala, and M. Sohal. Influence of substrate elasticity on droplet impact dynamics. *Langmuir*, 29(14):4520–4524, 2013.
- B. Blocken and J. Carmeliet. A review of wind-driven rain research in building science. *Journal of Wind Engineering and Industrial Aerodynamics*, 92(13):1079–1130, 2004.
- M. M. Driscoll and S. R. Nagel. Ultrafast interference imaging of air in splashing dynamics. *Phys. Rev. Lett.*, 107:154502, Oct 2011. doi: 10.1103/PhysRevLett.107.154502.
- A. S. Ellis, F. T. Smith, and A. H. White. Droplet impact on to a rough surface. *Quarterly Journal of Mechanics and Applied Mathematics*, 64(2):107–139, 2011.
- I. S. Gradshteyn and I. M. Ryzhik. *Table of integrals, series and products*. Academic Press, seventh edition, 2007.
- P. D. Hicks and R. Purvis. Air cushioning and bubble entrapment in three-dimensional droplet impacts. *Journal of Fluid Mechanics*, 649:135–163, 2010. doi: 10.1017/S0022112009994009.
- P. D. Hicks and R. Purvis. Air cushioning in droplet impacts with liquid layers and other droplets. *Physics of Fluids*, 23(6):062104, 2011. doi: 10.1063/1.3602505.

- P. D. Hicks and R. Purvis. Gas-cushioned droplet impacts with a thin layer of porous media. *Journal of Engineering Mathematics*, 102(1):65–87, Feb 2017. doi: 10.1007/s10665-015-9821-y.
- S. D. Howison, J. R. Ockendon, and S. K. Wilson. Incompressible water-entry problems at small deadrise angle. *Journal of Fluid Mechanics*, 222:215–230, 1991.
- S. D. Howison, J. R. Ockendon, J. M. Oliver, R. Purvis, and F. T. Smith. Droplet impact on a thin fluid layer. *Journal of Fluid Mechanics*, 542:1–23, 2005.
- C. J. Howland, A. Antkowiak, J. R. Castrejón-Pita, S. D. Howison, J. M. Oliver, R. W. Style, and A. A. Castrejón-Pita. It’s harder to splash on soft solids. *Phys. Rev. Lett.*, 117:184502, Oct 2016. doi: 10.1103/PhysRevLett.117.184502.
- T. I. Khabakhpasheva and A. A. Korobkin. Elastic wedge impact onto a liquid surface: Wagner’s solution and approximate models. *Journal of Fluids and Structures*, 36:32–49, January 2013.
- J. M. Kolinski. *The role of air in droplet impact on a smooth, solid surface*. PhD thesis, Harvard University, 2015.
- A. A. Korobkin. Formulation of penetration problem as a variational inequality. *Dinamika Sploshnoi Sredy*, 58:73–79, 1982.
- A. A. Korobkin. Initial asymptotics of solution of three-dimensional problem on a blunt body penetration into ideal liquid. *Doklady Akad. Nauk SSSR*, 283, 1985.
- A. A. Korobkin. *Water impact problems in ship hydrodynamics*, chapter 7, pages 323–371. Computational Mechanics Publications, 1996.
- A. A. Korobkin. Wave impact on the centre of an Euler beam. *Journal of Applied Mechanics and Technical Physics*, 39(5), 1998. doi: 10.1007/BF02468049.
- A. A. Korobkin and T. I. Khabakhpasheva. Regular wave impact onto an elastic plate. *Journal of Engineering Mathematics*, 55:127–159, 2006.

- A. A. Korobkin and Y.-M. Scolan. Three-dimensional theory of water impact. Part 2. Linearized Wagner problem. *Journal of Fluid Mechanics*, 549:343–373, 2006. doi: 10.1017/S0022112005008049.
- A.A. Korobkin and Y. M. Scolan. Energy distribution from vertical impact of a three-dimensional solid body onto the flat free surface of an ideal fluid. *Journal of Fluids and Structures*, 17(2), 2003.
- A. W. Leissa. Vibration of plates. Technical report, Scientific and Technical Information Division, National Aeronautics and Space Administration, 1969.
- M B Lesser and J E Field. The impact of compressible liquids. *Annual Review of Fluid Mechanics*, 15(1):97–122, 1983.
- T. Maitra, C. Antonini, M. K. Tiwari, A. Mularczyk, Z. Imeri, P. Schoch, and D. Poulikakos. Supercooled water drops impacting superhydrophobic textures. *Langmuir*, 30(36):10855–10861, 2014a. doi: 10.1021/la502675a. PMID: 25157476.
- T. Maitra, M. K. Tiwari, Antonini C, P. Schoch, S. Jung, P. Eberle, and D. Poulikakos. On the nanoengineering of superhydrophobic and impalement resistant surface textures below the freezing temperature. *Nano Letters*, 14(1): 172–182, 2014b. doi: 10.1021/nl4037092.
- S. Mandre, M. Mani, and M. P. Brenner. Precursors to splashing of liquid droplets on a solid surface. *Phys. Rev. Lett.*, 102:134502, Mar 2009. doi: 10.1103/PhysRevLett.102.134502.
- S. Mangili, C. Antonini, M. Marengo, and A. Amirfazli. Understanding the drop impact phenomenon on soft PDMS substrates. *Soft Matter*, 8(39):10045–10054, 2012.
- G. D. Martin, S. D. Hoath, and I. M. Hutchings. Inkjet printing - the physics of manipulating liquid jets and drops. *Journal of Physics: Conference Series*, 105:012001, Mar 2008. doi: 10.1088/1742-6596/105/1/012001. URL <https://doi.org/10.1088/1742-6596/105/1/012001>.

- A. C. McBride. Solution of dual integral equations of Titchmarsh type using generalised functions. *Proceedings of the Royal Society of Edinburgh: Section A-Mathematics*, 83:263–281, 1979.
- M. R. Moore and J. M. Oliver. On air cushioning in axisymmetric impacts. *IMA Journal of Applied Mathematics*, 79(4):661–680, 08 2014. ISSN 0272-4960. doi: 10.1093/imamat/hxu026.
- M. R. Moore, S. D. Howison, J. R. Ockendon, and J. M. Oliver. Three-dimensional oblique water-entry problems at small deadrise angles. *Journal of Fluid Mechanics*, 711:259–280, 2012.
- M. R. Moore, J. R. Ockendon, and J. M. Oliver. Air-cushioning in impact problems. *IMA Journal of Applied Mathematics*, 78(4):818–838, 2013. doi: 10.1093/imamat/hxt026.
- Y. Narita. *Free vibration of elastic plates with various shapes and boundary conditions*. PhD thesis, Hokkaido University, 1980.
- J. M. Oliver. *Water entry and related problems*. PhD thesis, St Anne’s College, University of Oxford, 2002.
- R. E. Pepper, L. Courbin, and H. A. Stone. Splashing on elastic membranes: The importance of early-time dynamics. *Physics of Fluids*, 20(8):082103, 2008. doi: 10.1063/1.2969755. URL <https://doi.org/10.1063/1.2969755>.
- J. Philippi, P. Y. Lagree, and A. Antkowiak. Drop impact on a solid surface: short time self-similarity. *Journal of Fluid Mechanics*, 795:96–138, 2016.
- G. Poots, R. W. Gent, N. P. Dart, and J. T. Cansdale. Aircraft icing. *Philosophical Transactions of the Royal Society of London. Series A: Mathematical, Physical and Engineering Sciences*, 358(1776):2873–2911, 2000. doi: 10.1098/rsta.2000.0689.
- R. Purvis and F. T. Smith. Air-water interactions near droplet impact. *European Journal of Applied Mathematics*, 15(6):853–871, 2004. doi: 10.1017/S0956792504005674.

- R. Purvis and F.T. Smith. *Improving aircraft safety in icing conditions*, pages 145–151. Springer International Publishing, Cham, 2016. ISBN 978-3-319-25454-8. doi: 10.1007/978-3-319-25454-8\_19.
- G. Riboux and J. M. Gordillo. Experiments of drops impacting a smooth solid surface: A model of the critical impact speed for drop splashing. *Phys. Rev. Lett.*, 113:024507, Jul 2014. doi: 10.1103/PhysRevLett.113.024507.
- Y. M. Scolan. Hydroelastic behaviour of a conical shell impacting on a quiescent-free surface of an incompressible liquid. *Journal of Sound and Vibration*, 227(1-2):163–203, 2004.
- Y. M. Scolan and A. A. Korobkin. Three-dimensional theory of water impact. Part 1. Inverse Wagner problem. *Journal of Fluid Mechanics*, 440:293–326, 2001.
- Y. A. Semenov, G. X. Wu, and A. A. Korobkin. Impact of liquids with different densities. *Journal of Fluid Mechanics*, 766:5–27, 2015. doi: 10.1017/jfm.2015.8.
- F. T. Smith, L. Li, and G. X. Wu. Air cushioning with a lubrication/inviscid balance. *Journal of Fluid Mechanics*, 482:291–318, 2003. doi: 10.1017/S0022112003004063.
- J. E. Sprittles. Kinetic effects in dynamic wetting. *Phys. Rev. Lett.*, 118:114502, Mar 2017. doi: 10.1103/PhysRevLett.118.114502.
- J. E. Sprittles and Y. D. Shikhmurzaev. The dynamics of liquid drops and their interaction with solids of varying wettabilities. *Physics of Fluids*, 24(8):082001, 2012.
- S. T. Thoroddsen, T. G. Etoh, and K. Takehara. Air entrapment under an impacting drop. *Journal of Fluid Mechanics*, 478:125–134, 2003. doi: 10.1017/S0022112002003427.
- S. T. Thoroddsen, T. G. Etoh, K. Takehara, N. Ootsuka, and Y. Hatsuki. The air bubble entrapped under a drop impacting on a solid surface. *Journal of Fluid Mechanics*, 545:203–212, 2005. doi: 10.1017/S0022112005006919.

- L. A. Tkacheva. Impact of a box with an elastic bottom on a thin liquid layer. *Journal of Applied Mathematics and Mechanics*, 72(4):427–436, 2008.
- T. Tran, H. de Maleprade, C. Sun, and D. Lohse. Air entrainment during impact of droplets on liquid surfaces. *Journal of Fluid Mechanics*, 726:R3, 2013. doi: 10.1017/jfm.2013.261.
- J. H. G. Verhagen et al. The impact of a flat plate on a water surface. *Journal of Ship Research*, 11(04):211–223, 1967.
- T. von Karman. The impact on seaplane floats during landing. *National Advisory Committee for Aeronautics*, 321:309–313, October 1929.
- H. Wagner. Über stoss- und gleitvorgänge an der oberfläche von flüssigkeiten. *Zeitschrift für Angewandte Mathematik und Mechanik*, 12(4):193–215, 1932.
- S. K. Wilson. A mathematical model for the initial stages of fluid impact in the presence of a cushioning fluid layer. *Journal of Engineering Mathematics*, 25(3):265–285, Aug 1991. doi: 10.1007/BF00044334.
- G. X. Wu. Two-dimensional liquid column and liquid droplet impact on a solid wedge. *Quarterly Journal of Mechanics and Applied Mathematics*, 60:496–511, 2007.
- G. D. Xu, G. X. Wu, and W. Y. Duan. Axisymmetric liquid block impact on a solid surface. *Applied Ocean Research*, 33(4):366–374, October 2011.
- L. Xu. Liquid drop splashing on smooth, rough, and textured surfaces. *Phys. Rev. E*, 75:056316, May 2007. doi: 10.1103/PhysRevE.75.056316.
- L. Xu, W. W. Zhang, and S. R. Nagel. Drop splashing on a dry smooth surface. *Physical Review Letters*, 94(18):184505, 2005.

# A

## Integrals $U_n$

---

The integrals

$$U_n = \int_0^1 r w_n^2(r) dr, \quad (\text{A.0.1})$$

where

$$w_n(r) = J_0(k_n r) - \frac{J_0(k_n)}{I_0(k_n)} I_0(k_n r), \quad (\text{A.0.2})$$

and  $k_n$  are the real solutions of the equation (2.3.8), provide

$$U_n = \int_0^1 r \left( J_0(k_n r) - \frac{J_0(k_n)}{I_0(k_n)} I_0(k_n r) \right)^2 dr. \quad (\text{A.0.3})$$

The integrals (A.0.3) are evaluated by using the standard integrals:

$$\int_0^1 x J_0^2(ax) dx = \frac{1}{2} (J_0^2(a) + J_1^2(a)), \quad (\text{A.0.4})$$

$$\int_0^1 x I_0^2(ax) dx = \frac{1}{2} (I_0^2(a) - I_1^2(a)), \quad (\text{A.0.5})$$

$$\int_0^1 x J_0(ax) I_0(ax) dx = \frac{J_0(a) I_1(a) + J_1(a) I_0(a)}{2a}. \quad (\text{A.0.6})$$

The result is

$$U_n = \left( 1 - \frac{2}{1-\nu} - \frac{2k_n^2}{(1-\nu)^2} \right) J_0^2(k_n) + \frac{2k_n}{1-\nu} J_0(k_n) J_1(k_n), \quad (\text{A.0.7})$$

where  $U_n = O(k_n)$  as  $n \rightarrow \infty$ .

# B

## Integrals $Q_n(a)$

---

Substituting the normal modes (2.3.7) of a circular simply supported plate into (2.3.18),

$$Q_n(a) = \int_0^{\frac{\pi}{2}} \sin(\theta) \left( J_0(ak_n \sin(\theta)) - \frac{J_0(k_n)}{I_0(k_n)} I_0(ak_n \sin(\theta)) \right) d\theta, \quad (\text{B.0.1})$$

and using the standard relations:

$$\int_0^{\frac{\pi}{2}} \sin(\theta) J_0(X \sin(\theta)) d\theta = \frac{\sin(X)}{X}, \quad (\text{B.0.2})$$

$$\int_0^{\frac{\pi}{2}} \sin(\theta) I_0(X \sin(\theta)) d\theta = \frac{\sinh(X)}{X}, \quad (\text{B.0.3})$$

we find

$$Q_n(a) = \frac{\sin(ak_n)}{ak_n} - \frac{J_0(k_n)}{I_0(k_n)} \frac{\sinh(ak_n)}{ak_n}. \quad (\text{B.0.4})$$

The functions  $Q_n(a)$  are depicted in figure B.0.1, for  $n = 1, 2, 3, 4$ . The functions behave as  $\sin(ak_n)/(ak_n)$  for large  $n$  because  $J_0(k_n)/I_0(k_n) \rightarrow 0$  as  $n \rightarrow \infty$  in (B.0.4).

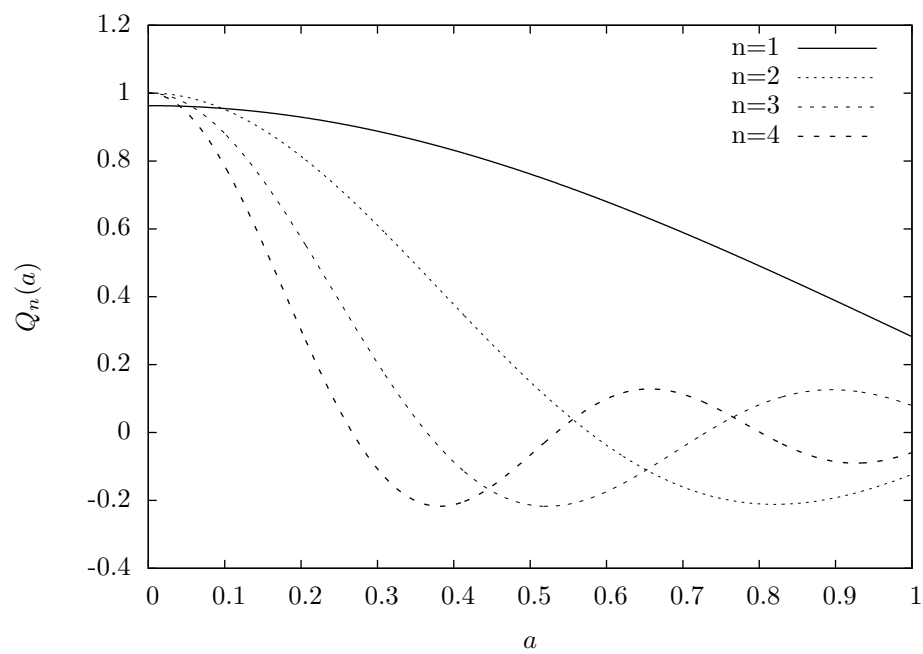


Figure B.0.1: The functions  $Q_n(a)$  for  $n = 1, 2, 3$  and  $4$  using modes calculated with  $\nu = 0.3$ .

# C

## Calculation of the vector elements

$$g_n(a)$$


---

Substituting (2.3.7) and (2.3.32) in (2.3.14),

$$g_n(a) = \frac{2\dot{h}}{\pi} \int_0^a r \sqrt{a^2 - r^2} \left( J_0(k_n r) - \frac{J_0(k_n)}{I_0(k_n)} I_0(k_n r) \right) dr, \quad (\text{C.0.1})$$

and making the substitution  $r = a \sin(\theta)$  gives

$$g_n(a) = \frac{2a^3 \dot{h}}{\pi} \int_0^{\frac{\pi}{2}} (\sin(\theta) - \sin^3(\theta)) \left( J_0(k_n r) - \frac{J_0(k_n \sin(\theta))}{I_0(k_n)} I_0(k_n \sin(\theta)) \right) d\theta. \quad (\text{C.0.2})$$

The four integrals in (C.0.2) are given by:

$$\int_0^{\frac{\pi}{2}} \sin(\theta) J_0(K \sin(\theta)) d\theta = \frac{\sin(K)}{K}, \quad (\text{C.0.3})$$

$$\int_0^{\frac{\pi}{2}} \sin(\theta) I_0(K \sin(\theta)) d\theta = \frac{\sinh(K)}{K}, \quad (\text{C.0.4})$$

$$\int_0^{\frac{\pi}{2}} \sin^3(\theta) J_0(K \sin(\theta)) d\theta = \frac{K \cos(K) - \sin(K) + K^2 \sin(K)}{K^3}, \quad (\text{C.0.5})$$

$$\int_0^{\frac{\pi}{2}} \sin^3(\theta) I_0(K \sin(\theta)) d\theta = \frac{\sinh(K) - K \cosh(K) + K^2 \sinh(K)}{K^3}. \quad (\text{C.0.6})$$

Combining (C.0.3)-(C.0.6) with (C.0.2) gives

$$g_n(a) = \frac{2\dot{h}}{\pi k_n^3} \left( \sin(ak_n) - ak_n \cos(ak_n) - \frac{J_0(k_n)}{I_0(k_n)} (ak_n \cosh(ak_n) - \sinh(ak_n)) \right). \quad (\text{C.0.7})$$

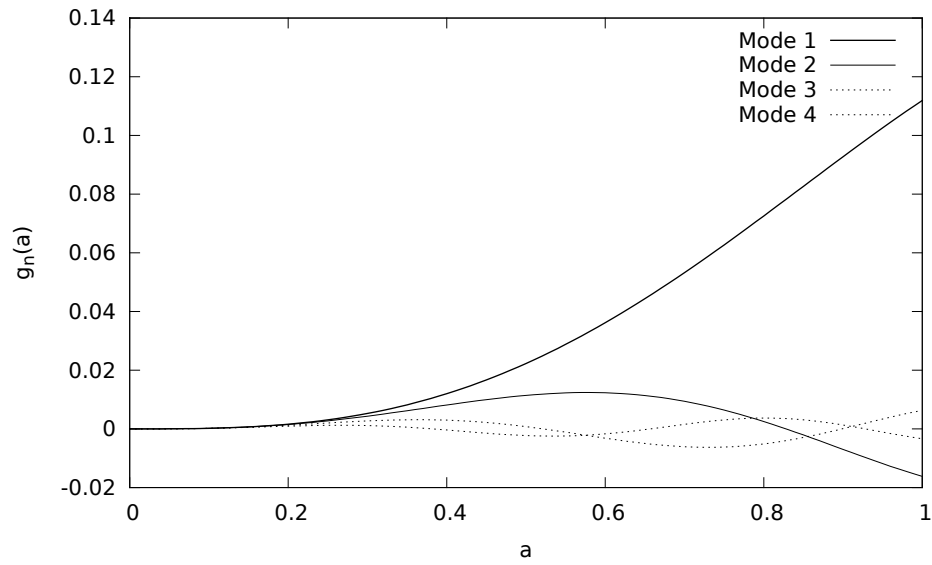


Figure C.0.1:  $g_n$  versus  $a$  for  $n = 1, 2, 3$  and  $4$  using modes calculated with  $\nu = 0.3$  for  $\dot{h} = 1$ .

The functions  $g_n(a)/\dot{h}$  are depicted in figure C.0.1 for  $n = 1, 2, 3, 4$ . The functions behave as  $-(2a/\pi k_n^2) \cos(ak_n)$  as  $n \rightarrow \infty$ .

## D

### Elements of the added-mass matrix

---

The integrals (2.3.36),

$$W_{nm}(a) = \frac{2a^3}{\pi} \int_0^1 y^2 Q_n(ay) Q_m(ay) dy, \quad (\text{D.0.1})$$

are evaluated analytically by using  $Q_n(ay)$  and  $Q_m(ay)$  from (B.0.4):

$$\begin{aligned} W_{nm}(a) = \frac{2a}{\pi k_n k_m} \int_0^1 \left( \sin(ak_n y) \sin(ak_m y) - \frac{J_0(k_m)}{I_0(k_m)} \sin(ak_n y) \sinh(ak_m y) \right. \\ \left. - \frac{J_0(k_n)}{I_0(k_n)} \sinh(ak_n y) \sin(ak_m y) + \frac{J_0(k_n) J_0(k_m)}{I_0(k_n) I_0(k_m)} \sinh(ak_n y) \sinh(ak_m y) \right) dy. \end{aligned} \quad (\text{D.0.2})$$

The result is

$$\begin{aligned} W_{nm}(a) = \frac{2}{\pi k_n k_m} \left( \frac{k_m \sin(ak_n) \cos(ak_m) - k_n \cos(ak_n) \sin(ak_m)}{k_n^2 - k_m^2} \right. \\ - \frac{J_0(k_n)}{I_0(k_n)} \frac{k_n \sin(ak_m) \cosh(ak_n) - k_m \cos(ak_m) \sinh(ak_n)}{k_m^2 + k_n^2} \\ - \frac{J_0(k_m)}{I_0(k_m)} \frac{k_m \sin(ak_n) \cosh(ak_m) - k_n \cos(ak_n) \sinh(ak_m)}{k_n^2 + k_m^2} \\ \left. + \frac{J_0(k_n) J_0(k_m)}{I_0(k_n) I_0(k_m)} \frac{k_n \cosh(ak_n) \sinh(ak_m) - k_m \sinh(ak_n) \cosh(ak_m)}{k_n^2 - k_m^2} \right), \quad n \neq m, \end{aligned} \quad (\text{D.0.3})$$

$$\begin{aligned} W_{nn}(a) = \frac{2a}{\pi k_n^2} \left( \frac{1}{2} - \frac{\sin(2ak_n)}{4ak_n} - \frac{J_0(k_n)}{I_0(k_n)} \frac{\sin(ak_n) \cosh(ak_n) - \cos(ak_n) \sinh(ak_n)}{ak_n} \right. \\ \left. + \frac{J_0^2(k_n)}{I_0^2(k_n)} \left( \frac{\sinh(2ak_n)}{4ak_n} - \frac{1}{2} \right) \right). \end{aligned} \quad (\text{D.0.4})$$

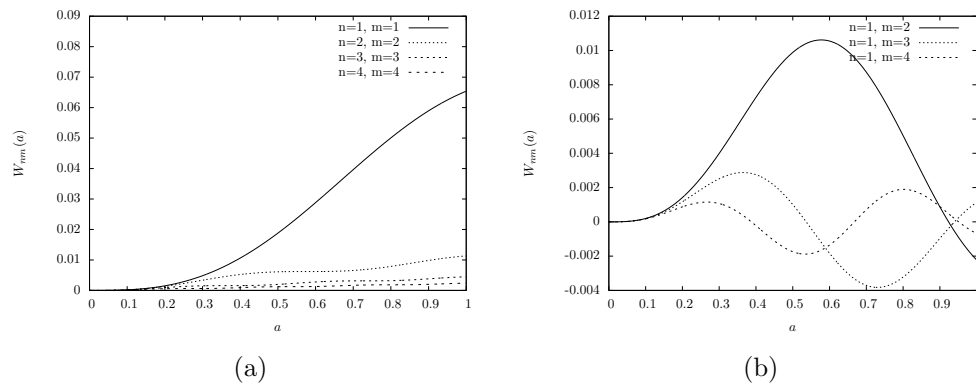


Figure D.0.1: (a) The first 4 diagonal elements of the added mass matrix,  $W_{nn}(a)$ . (b) The first 3 off diagonal elements of the first column of the added mass matrix,  $W_{nm}(a)$ .

The functions  $W_{nm}(a)$  are depicted in figure D.0.1. The diagonal elements of the added mass matrix,  $W_{nn}(a)$ , behave as  $1/k_n^2$  when  $n \rightarrow \infty$ .